



TAMPERE UNIVERSITY OF TECHNOLOGY

HEIKKI VIRTANEN
TIME-DOMAIN TRAVELLING WAVE MODELLING OF
DUAL-WAVELENGTH DFB LASERS IN REMOTE
HETERODYNE DETECTION LINKS

Master of Science thesis

Examiner: Docent Mihail Dumitrescu
Examiner and topic approved by the
Faculty Council of the Faculty of
Natural Sciences
on 8th October 2014

ABSTRACT

HEIKKI VIRTANEN: Time-Domain Travelling Wave Modelling of Dual-Wavelength DFB Lasers in Remote Heterodyne Detection Links

Tampere University of Technology

Master of Science thesis, 101 pages, 4 Appendix pages

May 2015

Master of Science (Tech.) Degree Programme in Science and Engineering

Major: Engineering Physics

Examiner: Docent Mihail Dumistrescu

Keywords: travelling wave, finite difference, remote heterodyne detection, dual-mode laser

The development of high-speed electronics has improved the availability and reduced the cost of components operating in the millimeter wave (MMW) region substantially. Therefore, in recent years the spectral range of 30–300 GHz has received a strongly increased interest in various application areas such as medical imaging, spectroscopy, radars, and guidance systems. The progress of MMW technologies has opened new opportunities in optical communication, and it has also made possible the rebirth of optical heterodyne detection systems.

Remote heterodyne detection (RHD) links are promising candidates for the optical MMW generation in the future. The most critical challenge in RHD links is the generation of two stable and phase-correlated laser lines. This work focuses on RHD links, and the generation of optical carriers using novel distributed feedback (DFB) laser diodes (LDs). These lasers provide a compact low cost solution for the optical MMW generation with a tunable frequency separation that can be exploited in numerous applications, particularly in RHD links.

The thesis gives a general presentation of optical communication links followed by a presentation of the elements and the characteristics of RHD links, outlining the difficulties and advantages of employing RHD links in optical communications. Multi-quantum-well distributed feedback laser diode principles and characteristics are reviewed and the LD requirements for operating as light sources in optical RHD links are derived. The thesis also presents a time-domain travelling wave simulation model developed for complex multi-section LDs. The model was developed since the laser characteristics needed for operating as RHD light sources imply non-typical simulation conditions like longitudinally non-uniform transverse sections, longitudinally non-uniform carrier and photon densities, variable gain and grating coupling coefficient, and a combination of active and passive sections. The developed model takes into account spontaneous emission noise, gain dispersion and variations of the longitudinal effective refractive index, material gain, carrier densities and photon density. Based on this model a simulation program has been implemented. Nu-

merous simulation studies have been performed on the novel laser structures and the thesis presents some of the most relevant numerical modelling results, including continuous wave and transient analysis. The simulation results are compared with experimental results and the differences are analyzed and discussed.

TIIVISTELMÄ

HEIKKI VIRTANEN: Kahden aallonpituuden DFB lasereiden aika-alueen etenevä aalto-mallintaminen etäisissä välitaajuusilmaisulinkeissä

Tampereen teknillinen yliopisto

Diplomityö, 101 sivua, 4 liitesivua

Toukokuu 2015

Teknis-luonnontieteellinen koulutusohjelma

Pääaine: Teknillinen fysiikka

Tarkastaja: dosentti Mihail Dumitrescu

Avainsanat: etenevä aalto, äärellinen differenssi, välitaajuusilmaisuus, kaksoismoodi-laser

Korkeanopeuksisen elektroniikan kehitys on parantanut millimetri-aallonpituudella toimivien komponenttien saatavuutta ja alentanut näiden hintaa merkittävästi. Siksi viime vuosina spektrialue 30–300 GHz on vastaanottanut voimakkaasti lisääntyntä mielenkiintoa monilla sovellutusalueilla aina lääketieteellisestä kuvantamisesta, spektroskopiasta ja tutkista, ohjausjärjestelmiin asti. Millimetriaaltoteknologioiden edistys on avannut mahdollisuuksia optisessa kommunikaatiossa tehden myös mahdolliseksi optisten välitaajuusilmaisusysteemien uudestisyntymisen.

Etäiset välitaajuusilmaisulinkit ovat lupaavia kandidaatteja optiselle millimetriaallon tuottamiselle tulevaisuudessa. Tärkein haaste välitaajuusilmaisulinkeissä on kahden stabiilin ja vaihekorreloidun laserviivan tuottaminen. Tämä työ keskittyy välitaajuusilmaisulinkkeihin ja optisten kantaja-aaltojen tuottamiseen käyttämällä uudentyyppisiä hajautetun takaisinkytkennän (DFB) laserdiodeita (LD). Nämä laserit tarjoavat edullisen ja kompaktin ratkaisun optiseen millimetriaallon tuottamiseen säädettävällä taajuuserolla, jota voidaan käyttää hyödyksi monissa sovellutuksissa ja erityisesti välitaajuusilmaisulinkeissä.

Tutkielma antaa yleisen esityksen optisista kommunikaatiolinkeistä, jota seuraa esitys välitaajuusilmaisulinkkien perusosista ja ominaisuuksista yhteenvetäen vaikeudet ja edut välitaajuusilmaisulinkkien käyttämisessä optisessa kommunikaatiossa. Työssä käydään läpi monikvanttikaivoisten jakautuneen takaisinkytkennän laserdiodeiden periaatteita ja ominaisuuksia, sekä johdetaan puolijohdelasereille asetettuja vaatimuksia valonlähteenä toimimiselle optisissa välitaajuusilmaisulinkeissä. Tutkielma myös esittää aika-alueen etenevä aalto -simulaatiomallin, joka on kehitetty monimutkaisille ja moniosioisille laserdiodeille. Malli kehitettiin koska ominaisuudet, joita lasereilta vaaditaan välitaajuusilmaisulinkkien valonlähteenä toimisessa, johtavat epätyypillisiin simulaatioehtoihin kuten pitkittäisesti epäyhdenmukaisiin poikkileikkauksiin, pitkittäisesti epäyhdenmukaisiin kantaja- ja fotonitiheyksiin, vaihtelevaan vahvistukseen ja hilan kytkentäkertoimeen sekä aktiivi- ja passiivialueiden yhdistelmiin. Kehitetty malli ottaa huomioon spontaanin emissioon aiheuttaman häiriön, vahvistuksen dispersion sekä vaihtelut pitkittäisessä efekti-

ivisessä taitekertoimessa, materiaalin vahvistuksessa, kantajatiheyksissä ja fotonitiheydessä. Simulaatio-ohjelma on toteutettu tähän malliin pohjautuen. Lukuisia simulaatio-tutkimuksia on suoritettu uudentyyppiselle laserrakenteelle ja tutkielma esittää joitakin olennaisimpia numeerisia mallinnustuloksia, sisältäen jatkuva-aaltoista ja dynaamista analyysia. Simulaatiotuloksia verrataan kokeellisiin tuloksiin ja eroavaisuuksia analysoidaan ja tarkastellaan työssä.

PREFACE

The work that is at the basis of this master of science thesis has been performed at the Optoelectronic Research Centre (ORC), Tampere University of Technology (TUT).

First of all, I would like to thank my advisor Docent Mihail Dumitrescu for his advices, visions, encouragement and continuous support through the course of this work. I wish to express my sincere appreciation to him for a conducive environment that his research group has provided to me.

I am also grateful to Dr. Antti Laakso and MSc. Topi Uusitalo for their help, fruitful discussions and inspiring collaboration. This support has been invaluable. I would also like to express my great appreciation to Dr. Pekka Savolainen for offering me the chance to work at ORC.

I must also thank all the members of ORC and all the people that were involved in this study. My thanks are extended to several colleagues at Department of Physics, Department of Mathematics and Department of Electronics with whom I have had longer or shorter discussions about the various topics of this work. Last but not least, I would like to thank my friends, fellow students, parents, and my brother for their moral support.

Tampere, 26th May 2015

Heikki Virtanen

TABLE OF CONTENTS

Introduction	1
1. Optical transmission link	3
1.1 Basic concepts	3
1.1.1 Signal modulation	4
1.1.2 Characteristics of optical receivers	4
1.2 Optical fibers	5
1.2.1 Fiber modes	6
1.3 Optical detectors	8
1.3.1 p-n photodiodes	8
1.3.2 p-i-n photodiodes	10
1.3.3 Avalanche photodiodes	11
1.3.4 Noise in photodiodes	12
1.4 Intensity modulated direct detection links	13
1.4.1 Transmission distance limitations of Intensity-modulated direct- detection (IMDD) links	14
1.5 Main requirements of optical fibres and photodetectors in optical Mil- limeter wave (MMW) generation	16
2. Optical remote heterodyne detection	17
2.1 Optical remote heterodyne detection links	18
2.2 Sensitivity degradation of RHD receivers	20
2.2.1 Intensity noise	20
2.2.2 Phase noise	23
2.2.3 Nonlinear effects	24
2.2.4 Dispersion and polarization mismatch	25
2.3 Modulation schemes	30
2.3.1 Demodulation	32
2.4 Advantages and difficulties in remote heterodyne detection	34
3. Strained multi-quantum well distributed feedback lasers	35
3.1 Semiconductor band structure	35
3.2 Basics of semiconductor lasers	37
3.2.1 Occupation probabilities	40
3.3 Quantum well lasers	40
3.3.1 Separate confinement heterostructures	43
3.3.2 Multi-quantum well structures	45
3.3.3 Strained quantum well structures	47
3.4 Transverse laser structures	49
3.5 DFB lasers	50

3.6	Chirp and temperature induced effects in semiconductor lasers	53
3.7	Requirements for dual-wavelength laser sources in remote heterodyne detection links	54
4.	Travelling wave model of DFB lasers	56
4.1	Travelling wave equations	57
4.1.1	Gain and detuning factor in Time-domain travelling wave (TDTW) equations	60
4.1.2	Finite difference method and discretization	61
4.1.3	Gratings and coupled waves	63
4.2	Carrier rate equation	64
4.2.1	Recombination terms	65
4.3	Gain modelling	66
4.4	Spontaneous emission sources	68
4.5	Spectral linewidth	69
4.6	TDTW modelling of multi-section lasers	70
5.	Simulation results and comparisons	71
5.1	Conventional laser structures	71
5.2	Superstructure grating (SSG)-Distributed feedback (DFB) laser struc- tures	74
5.3	Continuous wave (CW) analysis of SSG-DFB laser structures	75
5.4	Multimode dynamics of Laser diode (LD)s	78
5.5	Large signal analysis of distributed phase shift structures	80
5.6	Comparisons	83
	Conclusions and future research	84
	References	86
A.	Appendix	102
B.	Appendix	103
C.	Appendix	104

ABBREVIATIONS AND NOTATIONS

Abbreviations

ASE	Amplified spontaneous emission
ASK	Amplitude-shift keying
ASP	Analog signal processing
BER	Bit-error rate
BL	Bandwidth-transmission distance product
CB	Conduction band
CD	Chromatic dispersion
CFL	Courant-Friedrich-Lewy
CW	Continuous wave
DFB	Distributed feedback
DH	Double heterostructure
DOS	Density of states
DPSK	Differential phase-shift keying
DSP	Digital signal processing
EDFA	Erdium doped fibre amplifier
FIR	Finite impulse response
FM	Frequency modulation
FSK	Frequency-shift keying
FWM	Four wave mixing
GRIN	Graded index
HH	Heavy hole
I	Light intensity
IIR	Infinite impulse response

IMDD	Intensity-modulated direct-detection
ISI	Intersymbol interference
LC	Laterally corrugated
LD	Laser diode
LED	Light emitting diode
LH	Light hole
LSHB	Longitudinal spatial hole burning
MFSK	M-ary frequency-shift keying
MMW	Millimeter wave
MPN	Mode partition noise
MQW	Multiple quantum well
N_{QW}	Number of quantum wells
PBG	Photonic band gap
PIIN	Phase-induced intensity noise
PLL	Phase locked loop
PMD	Polarization mode dispersion
PMM	Power matrix method
PSK	Phase-shift keying
QW	Quantum well
QWS	Quarter-wave shifted
RHD	Remote heterodyne detection
RIN	Relative intensity noise
<i>RO</i>	Relaxation oscillation
SBS	Stimulated Brillouin scattering
SCH	Separate confinement heterostructure

SMF	Single-mode fibre
SMSR	Side-mode suppression ratio
SNR	Signal-to-noise ratio
SPM	Self-phase modulation
SQW	Single quantum well
SRS	Stimulated Raman scattering
SSB	Single sideband
SSG	Superstructure grating
STFT	Short time Fourier transform
TDTW	Time-domain travelling wave
TE	Transverse electric field
TM	Transverse magnetic field
VB	Valence band
WDM	Wavelength-division multiplexing
WG	Waveguide
XPM	Cross-phase modulation

Symbols

J_m	m-th order Bessel function of the first kind
K_m	m-th order Bessel function of the second kind
A	Guiding area
a_f	Attenuation coefficient
$\alpha_{\mathcal{H}}$	Linewidth enhancement factor
ω	Angular frequency
A_{SRH}	Shockley-Reed-Hall recombination coefficient
ϕ	Azimuthal coordinate

B	Bit rate
B_{op}	Optical bandwidth
β	Propagation constant
β_{spont}	Spontaneous emission coupling coefficient
λ_B	Bragg wavelength
B_{spont}	Bimolecular recombination coefficient
BW	Frequency bandwidth
c	Speed of light
C	Capacitance
C_{CFL}	Courant-Friedrich-Lewy condition number
C_{Aug}	Auger recombination coefficient
\mathbb{C}	Set of complex numbers
Γ	Optical confinement factor
D	Second-order dispersion coefficient
d	Thickness of the guiding region
δ_f	Delta function
δ	Detuning factor
$\Delta\tau_{disp}$	Chromatic dispersion induced propagation delay
$\tilde{\mathbf{E}}$	Fourier transform of the electric field
E_F	Fermi energy
E_{sig}	Optical signal
E_{sp}	Spontaneous emission noise
E_c	Bottom conduction band energy
m_e^*	Effective mass of electrons
m_h^*	Effective mass of holes

E_g	Band gap
ϵ	Gain compression factor
η	Injection efficiency
E_v	Top valence band energy level
f	Operation frequency
F_A	Excess noise factor
f_{RF}	Millimeter wave frequency
a	Radius of the fibre core
$F(z, t)$	Forward travelling envelope function
G	Amplifier gain
g	Material gain
g_0	Gain coefficient
G_n	Noise figure
Gbps	Gigabits per second
G_m	Modal gain
m	Grating order
GS/s	Gigasamples per second
h	Planck constant
$\tilde{\mathbf{H}}$	Fourier transform of the magnetic field
I_d	Time-averaged dark current
I_p	Time-averaged photocurrent
I_{th}	Threshold current
\mathcal{I}_i	i-th bias current set
i	Imaginary unit
$\langle \cdot, \cdot \rangle$	Inner product of complex numbers

$i_{spont,f}$	Spontaneous emission noise source of the forward travelling envelope function
$i_{spont,r}$	Spontaneous emission noise source of the reverse travelling envelope function
K	Stimulated emission coefficient
k	Wave number
k_A	Dimensionless parameter of Avalanche photodiodes
k_B	Boltzmann constant
κ	Grating coupling coefficient
L	Maximum transmission distance
L_{cav}	Cavity length
ΔL_{path}	Path length difference
\mathcal{L}	Line broadening function
$\Delta\nu$	Linewidth
α_i	Internal loss factor
α_m	Mirror loss factor
L_z	Quantum well thickness
M	Multiplication factor
m_r	Reduced mass
M_s	Number of subsections
M	Transfer matrix
\mathcal{M}	Transition matrix element
n	Band index
$n_{cladding}$	Refractive index of the fibre cladding
n_{core}	Refractive index of the fibre core
N_{th}	Threshold carrier density

N_{tr}	Transparency carrier density
N_c	Electron density in the conduction band
n_{eff}	Effective refractive index
n_{sp}	Spontaneous emission factor
P_{in}	Time-averaged optical input power
P_{opt}	Average optical power
P_{out}	Laser output power
P_{rec}	Received average optical power
P_{sig}	Optical power
$\Delta\tau_{path}$	Path imbalance induced propagation delay
Λ	Grating period
$\Delta\phi$	Phase difference of optical waves
T_{PMD}	Polarization mode dispersion coefficient
$\Psi(\mathbf{r}, t)$	Electric field amplitude
P_v	Number of hole states in the valence band
q	Elementary charge
E_{Fc}	Quasi-Fermi level for the conduction band
E_{Fv}	Quasi-Fermi level for the valence band
R	Resistance
r	Radial coordinate
R_{abs}	Absorption emission rate
\mathcal{R}	Responsivity
r_i	Complex reflection coefficient of the i-th end facet
R_{spont}	Spontaneous emission rate
R_{stim}	Stimulated emission rate

$R(z, t)$	Reverse travelling envelope function
S	Photon density
S_{sp}	Noise spectral density
$\langle i_{RIN}^2 \rangle$	Relative intensity noise current
$\langle i_{Sig.-Sp.}^2 \rangle$	Signal-spontaneous beat noise current
$\langle i_{shot}^2 \rangle$	Shot noise current
$\langle i_{Sp.-Sp.}^2 \rangle$	Spontaneous-spontaneous beat noise current
$\langle i_{thermal}^2 \rangle$	Thermal noise current
κ_{pol}	Splitting ratio
ϑ	Subband quantum number
T	Temperature
τ_{RC}	RC time constant
τ_{tr}	Carrier transit time
τ	Carrier lifetime
τ_e	Shockley-Read-Hall recombination lifetime for electrons
τ_h	Shockley-Read-Hall recombination lifetime for holes
N_{tot}	Total noise power
$u(x, y)$	Transverse field amplitude
V	Volume of the guiding region
V_{act}	Active region volume
v_g	Group velocity
\mathbf{k}	Crystal momentum
λ	Operation wavelength
z	Longitudinal coordinate

INTRODUCTION

The idea of using light to carry information is not new. People have used fires to send messages for thousands of years. However, the modern idea of optical communication can be traced back to 1880, when a Scottish-born American scientist Alexander Graham Bell invented the very first photophone. It was a device that allowed voice transmission by the aid of a light beam [1]. The idea of the photophone waited about 90 years until the discovery of lasers and the development of optical fibers made optical communication practical and efficient [2].

Today, there is a wide variety of commercial and research applications for both guided and unguided optical communication systems. Everyday a huge amount of data is sent through optical fibers and the amount of data is still rapidly increasing. Computers and mobile devices all over the world interact with each other via the Internet, which is largely based on optical communication. The rapid rise in the amount of transferred information increases the competition between different optical communication technologies and there is a continuous pressure to find more effective solutions.

Because the list of applications involving optical communication is almost endless, there are also many different requirements that are critical, such as high transmission speed, portability, compact size (small footprint), high reliability and low cost. These requirements are pushing the optical communication systems towards the physical limitations of optical fibers, receivers/detectors and light sources. Thus, sophisticated methods have been developed to overcome these limitations. For instance, one very critical step was taken at the end of 1990s, when wavelength-division multiplexing (WDM) enabled sending independent optical channels through the same optical fiber [3]. Since then WDM has boosted transmission capacity of optical communication systems enormously.

In recent years the millimeter-wave (MMW) region has gained a lot of attention in many applications such as optical imaging, spectroscopy, and radars. The use of MMWs could also provide a compact and cost-effective solution for high-speed communication networks. The basic concepts of optical communication links are reviewed in Chapter 1. Chapter 2 focuses on remote heterodyne detection (RHD) which is a promising candidate for the implementation of optical MMW links in the future. A comparison between the RHD links and other types of links shows the potential advantages as well as the difficulties of implementing RHD links in optical communications. Chapter 3 presents the basic principles of multi-quantum-well (MQW) distributed feedback (DFB) lasers and outlines the characteristics required for their use as optical RHD light sources. Chapter 4 presents a time-domain travelling wave (TDTW) simulation model developed for complex multi-section laser

diodes (LDs) that could fulfil the requirements of optical RHD light sources. Chapter 5 presents some of the most relevant simulation results obtained with the model described in Chapter 4 and compares the simulations with experimental results. The achievements and conclusions of this work as well as the possible future developments are given in the conclusions.

1. OPTICAL TRANSMISSION LINK

1.1 Basic concepts

Even though there is a variety of different types of optical communications links, the basic principle of all these systems obeys Bell's photophone [1]. The communication links contain a data source, a transmitter that imprints the data on a carrier signal and sends it through a transmission channel, and a receiver which extracts the data from the received signal.

An optical link employs a light source as a transmitter. The primary role of the light source is to convert an electrical signal into an optical one. The basic requirements for light sources in optical communication systems depend on the application but the main features are spectral width, noise, cost, output power, modulation speed, reliability, temperature sensitivity and compatibility with optical fibers. Light emitting diodes (LEDs) and laser diodes are usually the best suited devices for these requirements. Hence, almost all optical communication links employ a LED or LD as a light source.

The generated optical signal is usually launched into an optical fiber. Optical fibers provide a reliable and secure transmission path for the propagation of light. Optical fibers also provide wide bandwidth, low attenuation and low transmission cost. In addition unguided transmission techniques can be used in optical communication. In this case the beam of light emitted by the transmitter spreads in free space. Unfortunately, light beams are not as practical as microwaves for broadcast applications because the transmitter and receiver must be aligned accurately in order to avoid significant coupling losses [4]. Although unguided links have many applications, these are not considered further in this work.

Receiver circuits are usually the most complex devices in optical links. An optical receiver contains an optoelectronic converter that converts the light signal back into an electrical signal. A receiver must also extract information from the received signal. Therefore receivers contain filters, comparators, and circuitry to recover and process the signal further by electrical means.

Moreover, the optical links can include some additional components such as repeaters, multiplexers, and demultiplexers. Repeaters and amplifiers (either optical or electro-optical) are used to regenerate optical signals and prevent corruption of the signal due to detrimental effects such as dispersion and attenuation. Multi-

plexers and demultiplexers are optical devices that combine several signal streams (carried by different wavelengths) into a single optical fiber channel and separate the received combined optical signal into the initial different signal streams, respectively. These devices are used to keep apart the different optical signals transmitted by different wavelengths through the same WDM optical fiber channel, such that the signals do not interfere with each other during the transmission.

1.1.1 Signal modulation

Communication links can be classified in many ways. One way of doing it is to discriminate communication links according to the type of signal modulation. Typically, communication systems use the variation of the amplitude, phase, or frequency of a carrier wave to encode the data. When analog modulation is used, the modulated property varies continuously as a function time. In digital modulation the information is transferred using only discrete values (of amplitude, frequency, phase or some combination of these) sampled at certain time slots. The simplest example is a binary signal, which can take two distinct values at given time slots.

Although both analog and digital optical modulation have many different applications, digital systems are prevalent these days. This is because digital signals can provide several advantages over analog signals. In optical systems the signal is usually generated using LEDs or LDs that are generally non-linear devices. However, the output of analog signals must follow the analog electrical input signal in order to maintain the waveform of the analog signal. Therefore analog transmitters require high linearity and stability. These requirements are often difficult to fulfill directly with LEDs or LDs, but can be achieved by exploiting external circuits [5]. Unfortunately, external circuits increase the cost and complexity of the transmitters.

Also the optical fibers can usually handle digital signals better than analog signals due to the channel non-linearity, attenuation, and dispersion. Analog signals also suffer more from noise because small changes that can be meaningful, but small changes can be also induced by noise. Consequently analog receivers have higher requirements in terms of noise than their digital counterparts. This work is concentrated on digital signals but a comprehensive picture of analog links can be found from [5, 6], for example.

1.1.2 Characteristics of optical receivers

One of the most critical characteristic of communication links is the transmission speed. Transmission speed can be defined in many ways. Data rate or bitrate describes how many bits are transferred between the transmitter and receiver in a unit time. However, data rate is not solely sufficient to define the transmission

speed, if logical symbols can have more values than 'on' and 'off'. Hence, symbol or baud rate is used to express the number of symbol changes per unit time.

When the transmission speed of a transmitter increases, the reliability of communication links decreases. In a binary signal this means that the number of bit errors increases. Bit errors describe bits of a data stream that have changed with respect to the original bit stream during the transmission.

The bit-error rate or ratio (BER) is in turn an indicator of how often the decision circuit of the receiver will interpret a bit differently than the transmitter has intended. BER is usually expressed as a ratio of error bits per transmitted bits during the transmission interval. Because the number of bit errors depends strongly on the length of the sample, reliability of a communication link is usually expressed in terms of BER. A common criterion for communication links is to achieve $\text{BER} \leq 10^{-9}$ [4], but more stringent requirements such as $\text{BER} \leq 10^{-12}$ can also be used.

In practice all signals have certain average power and noise levels. Noise has many sources such as the transmitter or receiver circuit themselves. Despite the noise sources, all receivers require that the power level of the signal is some amount higher than the noise level in order to detect the signal. The difference between the average power of the signal and noise level can be characterized through signal-to-noise ratio (SNR).

If the SNR value is low, the signal cannot be distinguished from the noise and digital receivers cannot maintain reliable communication. Therefore receivers have a SNR value which is required to achieve a certain specific BER value [4]. The sensitivity characterizes this property of receivers. At a given modulation format, sensitivity depends on the design of the receiver as well as BER value and data rate. Typically, there are also many detrimental effects in communication links. These effects, such as waveform distortion, can reduce the receiver sensitivity [7].

Usually the communication systems are designed such that the transferred signal has a SNR level higher than the sensitivity of the receiver. This safety margin guarantees that the receiver provides reliable communication. On the other hand the extra power is wasted which increases transmission cost [7].

1.2 Optical fibers

Today optical fibers are an essential part of any guided optical communication systems. Despite the fact that the very first experiments with guided light were made in the 19th century, this invention was forgotten for many decades [8,9]. The progress in the research of optical fibers was very slow, until the discovery of lasers gave a big boost to this branch of engineering. Before the 1960s the idea of long-haul optical communication systems was impractical, because attenuation in optical fibers was high. However, this technological barrier was solved in 1966 [2]. This also

accelerated the development of optical communication systems.

Usually optical fibers used in optical communication, are fabricated from high purity fused silica glass. The optical fibers consist of a core surrounded by a cladding and protective outer jacket. The cladding is fabricated from one or many layers of materials such that it has a slightly lower refractive index than the core in which light is guided. This refractive index change can be continuous (graded-index fibers) or it can have an abrupt interface (step-index fibers).

Light intensity experiences attenuation due to absorption and scattering, when it travels through optical fibers [10]. Attenuation is an important factor in communication links because it eventually limits the transmission distance of unamplified optical signals. Losses of optical fibers depend on the wavelength of the light propagating within it. Silica glass based fibers have three spectral domains in near-infrared where communication links usually operate due to the relatively low attenuation. The first window is at 800 – 900 nm which is typically used for short-distance communication. Cheaper light sources and detectors can be utilized in the first window. The second window is at 1250 – 1350 nm where chromatic dispersion (CD) in silica fibers vanishes. The third window is at 1430 – 1600 nm. This window is typically used in long-haul communication because it has the minimum attenuation ($\sim 0.2\text{dB/km}$) and it coincides with the gain bandwidth of Erbium doped fiber amplifiers (EDFAs) [11].

Optical fibers also have other impairments apart from losses that can limit performance of communication links such as dispersion, non-linear effects and birefringence. These effects are discussed further in Section 2.2.

1.2.1 Fiber modes

In optical fibers the propagation of light can be explained using different models, the simplest being the ray optics model. However, the ray optics model is only valid for fibers which have a relatively large core diameter compared to the operation wavelength. For example, a typical single-mode fiber (SMF) may have a core radius which is only a few microns and therefore ray optics is not capable of accurately describing light propagation in single-mode optical fibers.

Classical electromagnetic theory [12] on the other hand, gives a fundamental and accurate description of light propagation in optical fibers with any dimensions. Of course, this model is computationally more intense than the ray optics model. However, ideal optical fibers have a cylindrical shape and it allows a simpler formulation. Particularly, this is the case when the weakly guiding approximation ($n_{core} - n_{cladding} \ll n_{core}$) holds and it is applied to step-index fibers. Then a pair

of Helmholtz equations [4]

$$\nabla^2 \tilde{\mathbf{E}} + k^2(\omega) \tilde{\mathbf{E}} = \mathbf{0}, \quad (1.1)$$

$$\nabla^2 \tilde{\mathbf{H}} + k^2(\omega) \tilde{\mathbf{H}} = \mathbf{0}, \quad (1.2)$$

with appropriate boundary conditions can be used to describe the propagation of light in the time-harmonic form ¹.

Equations (1.1) and (1.2) can be solved parallel in terms of two independent variables that are usually chosen to be the longitudinal components. After longitudinal components are solved it is possible to determine the transverse components from these independent variables using Maxwell's equations [7]. Assuming that the solution is separable, the trial for the electric field

$$E_z(r, \phi, z) = R(r)\Phi(\phi)Z(z) \quad (1.3)$$

leads to a system of ordinary differential equations [4]

$$\frac{d^2 Z}{dz^2} + \beta^2 Z = 0, \quad \beta \in \mathbb{C} \quad (1.4a)$$

$$\frac{d^2 \Phi}{d\phi^2} + m^2 \Phi = 0, \quad m \in \mathbb{Z} \quad (1.4b)$$

$$\frac{d^2 R}{dr^2} + \frac{1}{r} \frac{dR}{dr} + \left(h^2 - \frac{m^2}{r^2} \right) R = 0, \quad \begin{cases} h = n_{core}^2 k_0^2 - \beta^2, r \leq a \\ h = \beta^2 - n_{core}^2 k_0^2, r > a \end{cases} \quad (1.4c)$$

in the case of step-index fibers. Here the radius of the core is denoted by a . The longitudinal component has a plane wave ($Z(z) = e^{i\beta z}$) solution and the azimuthal component has a 2π -periodic ($\Phi(\phi) = e^{im\phi}$) solution due to the rotational symmetry with respect to the azimuthal angle.

The radial equation is a Bessel equation and its non-trivial solutions are linear combinations of well-known Bessel functions ($R(z) = AJ_m(hr) + BJ_m(hr)$) [13]. The unknown constants $A \in \mathbb{C}$ and $B \in \mathbb{C}$ can be determined, when appropriate boundary conditions (continuous differentiability is required) are applied. The Bessel equation has solutions only for certain values of β which remain bounded at the origin and tend to zero when r goes to infinity [13]. These solutions, which form a discrete spectrum, are so called guided modes. Equation (1.4c) may allow multiple solutions associated with the fixed m , depending on diameter of the core and material characteristics of the fiber. However, for single-mode fibers it is possible to find

¹ $k(\omega)$ is equivalent to $n(\omega)k_0$, where $k_0 = \frac{\omega}{c} = \sqrt{\epsilon_0 \mu_0}$ is the wave number, $n(\omega)$ is the refractive index of the material, ϵ_0 and μ_0 are the vacuum permittivity and permeability respectively. $\tilde{\mathbf{E}} = \tilde{\mathbf{E}}(\mathbf{r}, \omega)$ and $\tilde{\mathbf{H}} = \tilde{\mathbf{H}}(\mathbf{r}, \omega)$ denote Fourier transforms of the electric and magnetic fields.

only two eigenpairs which fulfill the equations (1.4) and the boundary conditions. The eigenpairs correspond to orthogonal polarization states and perfect rotational symmetry causes degeneracy between those states [4].

The dispersion relation $\beta(\omega)$ defines the frequency dependence of mode propagation and the inverse of its derivative gives the group velocity which is the propagation speed of the mode in the fiber.

1.3 Optical detectors

Photodetectors are crucial elements for optical communication links. The primary target of these devices is to convert an optical signal into an electrical one, after the signal is transferred optically through the transmission medium. Although semiconductor photodiodes are not the fastest available detectors, they can fulfill most of the requirements set for photodetectors such as high sensitivity, fast response, low noise, small size, low cost, and high reliability [4]. Particularly reverse-biased photodiodes based on the p-i-n junction are the most used detectors in optical communication links [4]. The basic principles of photodiodes are reviewed in order to understand the limitations that these devices set. The noise characteristics of photodiodes and the requirements that they should fulfill as RHD detectors are also discussed.

1.3.1 p-n photodiodes

The basic principle of a p-n junction based photodiode is simple. The p-n junction consist of asymmetrically distributed n-type and p-type semiconductor materials. When the p-n junction is illuminated and the incoming photons have an energy higher than the bandgap energy, the photons are absorbed with a certain non-zero probability. The photon absorption lifts an electron from the valence band into an empty state in the conduction band. Thus, photon absorption also generates an electron-hole pair. Finally, these electron-hole pairs are separated and enforced to drift into opposite directions (electrons towards n-side and holes towards p-side) primary under the influence of the internal electric field generated in the space charge region of the p-n junction by carrier diffusion. The carrier separation and transport by drift is more effective in the regions with significant electric field.

By reverse biasing the depletion region is extended and the applied electric field is added on top of the internal electric field, increasing the collective carrier flow ². When both ends of the junction are connected to an external circuit, it is possible to measure current flow through the terminals, which follows the variation of the

²In addition, carriers generated within the diffusion length from the edge of the depletion region can take a part in the carrier flow.

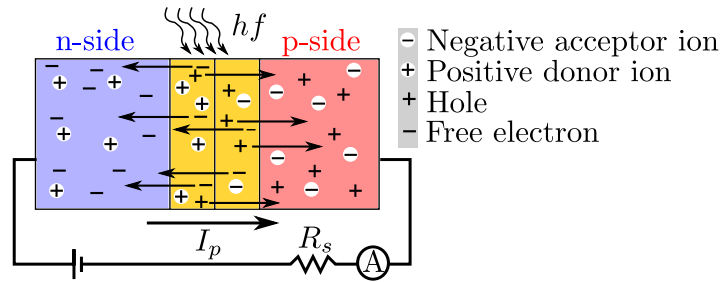


Figure 1.1: p-n junction based photodiodes consist of p-doped (with negative acceptor ions) and n-doped (with positive donor ions) regions. Carriers inside the space charge region (in yellow) are separated and swept away by drift.

optical field intensity incident on the photodiode [14]

$$I_p = \mathcal{R}P_{in} + I_d, \quad (1.5)$$

where P_{in} is the power of the incident light, \mathcal{R} is the responsivity and I_d is the dark current which arises due to the thermal excitation of carriers [15]. Dark current is present even if there is no light coming in the detector, but it can be neglected in many cases, because its magnitude is usually relatively small. Because optically generated electron-hole pairs are swept away from the depletion region by drift the photodiode becomes essentially faster if reverse bias is applied [4].

Although carriers are swept fast from the depletion region, mainly due to the internal field, the carrier transport does not happen instantaneously. The carrier transit-time (τ_{tr}) describes how fast this process occurs. However, the carrier transit-time is not the only physical restriction to the response time of p-n junction based detectors. The junction capacitance brings its own contribution to the response time of p-n junction based photodiodes. The junction capacitance together with the internal resistance and the resistive load form a RC-circuit having an equivalent time constant (τ_{RC}) [14]. Hence, the junction capacitance can also limit the response time of photodiodes. The frequency bandwidth (BW) for photodiodes is usually limited by carrier transit-time and RC time constant according to the equation [4]

$$BW = \frac{1}{2\pi(\tau_{tr} + \tau_{RC})}. \quad (1.6)$$

Diffusive carriers, which are generated close to the edge of the depletion region, can also contribute to the photocurrent. Because diffusion is a relatively slow process, diffusive carriers decrease the bandwidth of photodiodes.

While the transit time increases with the width of the depletion region reducing the bandwidth, the RC time constant decreases with the width of the depletion region (due to reduced junction capacitance) increasing the bandwidth. The opti-

mum depletion region width decreases and the corresponding maximum bandwidth increases with the area of the detector. Unfortunately the photocurrent is also reduced with smaller depletion region width and smaller photodetector area. It should also be noted that higher photocurrents are desirable for increasing the SNR since they increase the shot noise in absolute value but decrease the shot and thermal noise relatively to the signal. The combination of high bandwidth (tens of gigahertz) and high photocurrents (tens of milliamperes) can be achieved in velocity-matched photodetectors [16, 17].

1.3.2 p-i-n photodiodes

p-i-n photodiodes work basically the same way as p-n photodiodes but they have a much wider depletion region, because a layer of intrinsic semiconductor material is sandwiched between the p and n-doped regions. There are some certain advantages obtained from using a p-i-n structure - better quantum efficiency, reduced junction capacitance, reduced variation of junction capacitance with applied voltage, greater proportion of the generated current being carried by the faster drift - discussed in the following.

When photons are injected, only a certain amount of photons contribute to the output current, because only some of the incident photons are absorbed due to stochastic nature of photoelectric effect. Also some of the photons are not entering in the active area of the photodiode and some photoelectrons recombine back to photons. The output and input of photodiodes have a relationship defined as an external quantum efficiency [4]

$$\eta = \frac{\text{electron collection rate}}{\text{photon incidence rate}} = \frac{I_p/q}{P_{in}/h\nu} = \frac{h\nu\mathcal{R}}{q}, \quad (1.7)$$

when dark current is assumed to be negligible. The p-i-n structure improves quantum efficiency, because wider depletion region allows more photons to be absorbed inside the depletion region.

Increasing the width of the depletion region also reduces the junction capacitance and thereby the RC time constant, thus increasing the bandwidth. Also reducing the ratio between the diffusion length and the drift length in the p-i-n structures results in a greater proportion of the generated current being carried by the faster drift process. This contributes to increasing the bandwidth. Therefore, p-i-n photodiodes are usually used today for high-speed applications due to the improved frequency bandwidth with respect to p-n photodiodes [14]. Although p-i-n photodiodes can have improved quantum efficiency and bandwidth, there is a trade-off between these two in the design of p-i-n devices.

When the width of the depletion region increases, the transit-time limited band-

width decreases, but RC-time limited bandwidth increases [14]. On the other hand, increasing the width increases quantum efficiency. Consequently, an optimization of the depletion region is required. There have been several studies concerning this limitation and advanced structures have been developed to overcome the trade-off between quantum efficiency and frequency bandwidth of p-i-n photodiodes [18].

It should also be noted that the depletion-layer width in a p-i-n diode does not vary significantly with the bias voltage (being roughly the same as the thickness the intrinsic region). Thus, the junction capacitance is essentially independent of the bias voltage, remaining constant in operation.

Heterojunction p-i-n structures offer additional flexibility in optimizing the performance of a photodiode. In a heterojunction p-i-n photodiode, the intrinsic/undoped region has a smaller bandgap than one or both of the doped regions. While the small bandgap of the active undoped region determines the long wavelength cut-off of the photoresponse one of the wider-bandgap doped region can serve as a window for the optical signal to reach the active region without experiencing any absorption. The diffusion mechanism is eliminated (increasing the bandwidth) by avoiding the photogeneration of carriers outside the low-bandgap depletion layer. Moreover, the large bandgap of the window region sets the short-wavelength cut-off of the photoresponse, which creates a spectral window for the p-i-n photodiode quantum efficiency and responsivity.

1.3.3 Avalanche photodiodes

Due to the attenuation, long-haul communication links typically require in-line amplification, which increases costs. Hence, the ability of detectors to maintain reliable communication even with relatively low power levels is essential for many communication links. Therefore, avalanche photodiodes have sometimes been used to increase quantum efficiency and sensitivity through the multiplication of generated carries.

Avalanche photodiodes are p-i-n photodiodes which operate with relatively high reverse voltage. The high voltage strongly accelerates optically excited carriers, so that they can generate secondary carriers [19], as it also occurs in photomultipliers. The avalanche carrier-multiplication process, which may take place over a relatively short distance, effectively amplifies the photocurrent by a significant factor.

Although the avalanche photodiodes can usually provide higher responsivity than p-i-n photodiodes, they also have smaller operation bandwidth than fast p-i-n photodiodes [14]. The increased responsivity reduces the noise influences of subsequent electronic amplifiers, whereas the quantum noise becomes more important and multiplication noise is also introduced.

1.3.4 Noise in photodiodes

The photocurrent of an ideal photodiode directly corresponds to the incoming photon flux. However, in practice the photocurrent $I_p = \mathcal{R}P_{in}$ experiences small variations, even when the input power P_{in} is stable. On the other hand the photon generation in the light source is a statistical process and the emission rate always has some random fluctuations. Amplifiers, if used, also generate some additional fluctuation to the signal. Therefore the incoming photon flux fluctuates around its mean value. The fluctuations are known as photon noise. In this section the detection noise is discussed and it is assumed that the incoming photon flux does not experience significant fluctuations.

The absorption of photons in photodiodes is also a statistical process and there is a certain probability for an absorption event to occur. Thus, the number of the photon absorption events can fluctuate with respect to time, which results in shot noise. In p-n and p-i-n photodiodes the shot noise current is given by [20]

$$\langle i_{shot}^2 \rangle = 2q(I_p + I_d)BW, \quad (1.8)$$

where BW is the noise bandwidth and q is the elementary charge.

Thermal noise originates from the thermal motion of electrons in resistive devices [11]. Hence, thermal noise is generated even without any bias. The thermal noise can have many sources in a receiver, such as the series resistance of the photodiode itself or a load resistor. Receivers contain amplifiers that can also enhance thermal noise. Usually this is taken in account using the noise figure of the amplifier (G_n), it is a simple factor describing the enhancement of thermal noise due to amplification. Thermal noise current for a resistance R at temperature T can be expressed as [4]

$$\langle i_{thermal}^2 \rangle = \frac{4k_B T G_n BW}{R}, \quad (1.9)$$

Both thermal and shot noises are white (i.e. they have a flat spectral power density) [4].

Avalanche photodiodes have similar thermal noise as p-n or p-i-n photodiodes. Nevertheless, the shot noise of avalanche photodiodes is enhanced with respect to p-i-n and p-n photodiodes due to the internal amplification process. Internal gain increases the photocurrent of avalanche photodiodes M times. For this reason photocurrent can be expressed as

$$I_p = M\mathcal{R}P_{in} \quad (1.10)$$

if dark current is neglected. Each primary carrier can generate a different number

of secondary-carriers than the others due to the random excitation of secondary-carriers. Therefore, the multiplication factor is a random variable that creates noise in the gain of a photodiode. The shot noise of avalanche photodiodes is characterized by [19]

$$\langle i_{shot}^2 \rangle = 2qI_p M^2 F_A BW, \quad (1.11)$$

where F_A is the excess noise factor [19]

$$F_A = k_A M + (1 - k_A)(2 - 1/M). \quad (1.12)$$

Typically it is assumed that the dimensionless parameter k_A is small ($0 \leq k_A \ll 1$) [19].

1.4 Intensity modulated direct detection links

One of the most intuitive and primitive ways to transfer MMWs optically is to generate MMWs from a sequence of intensity pulses. Intensity variations can be generated by modulating optical sources like LDs or LEDs directly. The optical intensity variations are detected using a photodiode. After detection, the data is processed further by electrical means. The information about the phase, frequency and state of polarization are lost in the direct detection. Currently, almost all commercial op-

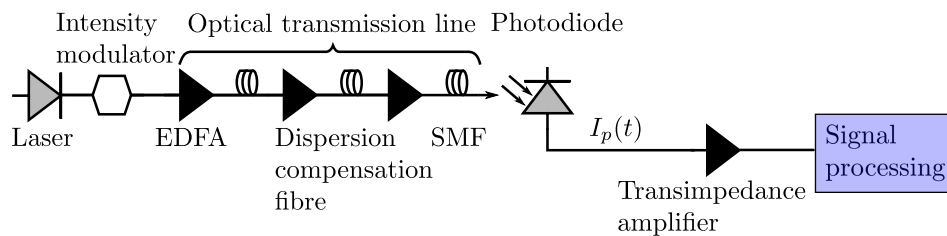


Figure 1.2: A typical single channel IMDD system.

tical communication systems use the intensity-modulation direct-detection (IMDD) scheme to transfer data. IMDD systems are compact and simple, which are the main reasons why these systems have dominated optical communication many decades. IMDD links have several drawbacks, such as low sensitivity, poor frequency selectivity [21] and low spectral efficiency [22]. However, IMDD links can mitigate some transmission impairments by utilizing EDFAs efficiently [22]. This has extended the reach of conventional IMDD systems. Nevertheless, high-speed IMDD links can suffer from serious signal degradation in long-haul transmission due to dispersion, waveform distortion and accumulated amplified spontaneous emission (ASE) noise [7].

1.4.1 Transmission distance limitations of IMDD links

Because transmission impairments accumulate along optical links, transmission systems are often characterized by a bandwidth-distance (BL) product. The distance can be defined as a maximum transmission length of a signal having a certain data rate fulfilling a predetermined BER value. The BL product of a IMDD link can be limited by different factors, but usually it is limited by the available power budget and attenuation or dispersion [11].

Typically long-haul unamplified communication links operating at low-speeds are limited by the signal strength at the receiver [7]. If the signal is too weak the receiver cannot retrieve the data. In that case the input power level must be increased or the sensitivity of the receiver has to be increased such that it is high enough to provide reliable communication. However, it is not necessarily possible to increase the input power due to non-linearity of the channel. The sensitivity of the receiver, in turn, can be increased by decreasing transmission speed [21]. On the other hand, if the length of the communication link becomes shorter, the power level of the signal at the receiver is higher, because transmission losses are also smaller. Thus, a higher data rate can be obtained. This describes the balance between the transmission speed and length. The maximum transmission distance of an unamplified power limited link can be estimated using an equation [4]

$$L = \frac{10}{a_f} \log_{10} \left(\frac{P_{out}}{P_{rec}} \right), \quad (1.13)$$

where a_f is the net loss in (dB/km), P_{out} is the laser output power and P_{rec} is the power level required to achieve a certain BER value at the receiver.

Power limitations can be reduced by enhancing the signal using in-line amplifiers. However, this increases also ASE noise in the link, which can limit the attainable BL product. Consequently, IMDD receivers are rather ASE noise limited than shot noise limited in long-haul communication links where multiple amplification stages are applied to the signal [22].

When the transmission distance increases, the BL product is not only limited by the available power budget and fiber attenuation, but also by fiber dispersion. Directly modulated IMDD links are sensitive to chromatic dispersion (CD) due to the non-zero spectral width of the optical signal. Besides the stationary spectral width of the light source, the optical signal spectrum is also broadened under intensity modulation. The intensity variations at the light source are associated with frequency variations, also known as chirp. The non-zero spectral width of the optical signal leads to intensity-pulse broadening as the pulses at different wavelengths travel at different speeds through a dispersive channel. Pulse broadening is a detri-

mental effect in IMDD links because it causes pulses to overlap. Eventually, the overlap is so large that the the receiver cannot distinguish them and the data is lost. Fortunately modern external modulators lower significantly the chirp compared to directly modulation lasers, thus reducing the dispersion sensitivity of intensity modulated signal [14].

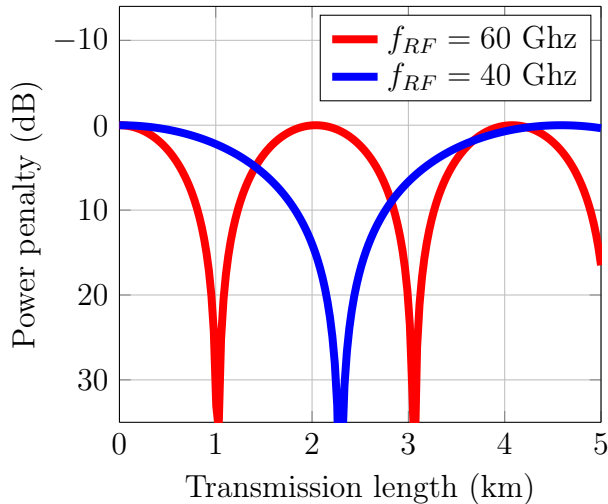


Figure 1.3: SNR penalty induced by chromatic dispersion in a IMDD link with different MMW frequencies as a function of transmission distance. Second-order dispersion coefficient $D = 17 \text{ ps}/(\text{nm} \cdot \text{km})$ and operation wavelength $1.55 \mu\text{m}$ are assumed. Attenuation is not taken into account in the calculations.

Although external modulators can reduce chromatic-dispersion-induced detrimental effects, these are not fully eliminated and CD can still affect the BL product of externally modulated high-speed long-haul IMDD links by causing significant SNR penalty [23]. In IMDD links the chromatic dispersion causes modulation sidebands to experience differential phase changes with respect to the carrier [24]. Therefore spectral components can interfere destructively at the receiver causing periodic signal fading [23]. CD induced SNR penalty can be estimated for an intensity modulated signal using [25]

$$I_p \sim \cos^2(\pi cDL(f_{RF}/f)^2), \quad (1.14)$$

where D is the second-order dispersion coefficient, f_{RF} is the MMW frequency and f is the optical carrier frequency. Figure 1.3 shows that, when dispersion compensation is not employed, the CD induced power penalty becomes significant after a few kilometers. The MMW signal completely vanishes, when the sidebands have opposite phases [23], as illustrated in Figure 1.3. At higher speeds, the transmission distance of IMDD links can also suffer from accumulated non-linear effects [4] or polarization mode dispersion (PMD) [26, 27].

1.5 Main requirements of optical fibres and photodetectors in optical MMW generation

Optical fibres and detectors are important elements in any guided optical communication system. The systems, that are particularly aimed to transfer MMWs, require several specific properties from the optical fibres and photodetectors. One of the most critical requirement in terms of photodetectors is the cut-off frequency that must reach the MMW frequency at which the system is designed to operate. Because the MMW frequency can be tens of gigahertz, this requirement can be quite severe. Usually it is also important that the frequency response of the photodetector is relatively flat close to the MMW frequency. Otherwise a small change in the MMW frequency can induce a large change in the photocurrent that can distort the signal and cause problems in the signal processing after the detection. However, there are some applications where a highly non-uniform frequency response can be desired such as the demodulation of a frequency modulated MMW signal. Moreover, high responsivity and low internal noise enable a high sensitivity for the receiver and therefore they are also wanted characteristics in photodetectors that are used in optical links to generate MMWs.

As shown in Section 1.4.1 chromatic dispersion can impose a periodic signal fading in IMDD links without a proper dispersion compensation. Optical fibers where the second-order chromatic dispersion vanishes at the operation wavelength give an alternative to overcome problems caused by CD. On the other hand this imposes higher losses (the zero-dispersion wavelength and the minimum-loss window do not coincide in ordinary single-mode fibers) or more costs (expensive dispersion-shifted fibers that have low attenuation and CD). Hence, more effective solutions such as RHD are developed to solve the limitations set by CD in optical fibres. A detailed discussion about RHD is included in the following chapter.

2. OPTICAL REMOTE HETERODYNE DETECTION

Even though IMDD systems have many benefits, they also suffer from various limitations as discussed in Section 1.4. Consequently many alternative schemes have been considered to eliminate the transmission impairments of IMDD links. In 1970 DeLange [28] made the first proposal of optical coherent heterodyne detection, where a MMW signal was generated optically by heterodyne mixing a laser spectral line with a local oscillator (LO) laser at the receiver, such that the spectral lines were separated by a desired MMW frequency.

The configuration provides many advantages over IMDD links, but it still has a major issue related to the large phase noise of semiconductor lasers. Although it is possible to stabilize the operation frequency of LDs [29, 30], the resulting MMW linewidth becomes Lorentzian shaped with a linewidth equal to the sum of the individual laser lines. This linewidth may not be narrow enough to achieve the predetermined BER value under modulation¹ and the transmission speed becomes strictly limited by the linewidth [31].

Fortunately the spectral purity of the MMW signal can be improved by heterodyning two phase-correlated spectral lines together [32]. However stable phase-correlation is hard to maintain in coherent heterodyne detection due to the random phase fluctuations of LDs, and therefore an optical phase locked loop is often required to synchronize the phases of the incoherent lasers. This requirement has been the main issue in coherent heterodyne detection.

Despite several other studies in 1980s and 1990s [29, 30] heterodyne detection systems were mainly used in research laboratories due to their complexity. Recently these systems have gained more attention because they provide several advantages over IMDD links that are particularly visible when transmission speeds and spectral congestion are increasing. The main virtues of heterodyne detection are:

- Higher sensitivity, easily obtained selectivity [21], and possibility to use sophisticated modulation formats as the phase, frequency, polarization, and amplitude can be recovered in the detection [22].
- The difference frequency linewidth can be much smaller than the optical

¹Unless very low phase noise lasers are used in the configuration [23].

linewidth of the signal and LO signal, provided the two are mutually coherent. An electronic filter can define an effective optical frequency bandpass that is narrower than any realizable wavelength filter operating on the light itself. This enables background light rejection and the detection of weak signals.

- For a strong LO, a possible noise reduction to the shot noise limit [33].
- The frequency difference is generally far away from the spectral ranges of many noise sources. Thus, the spectral region near the frequency difference is usually relatively quiet and electronic filtering can efficiently remove the remaining noise sources.
- The MMW signal is easily down-converted to frequencies where it is possible to exploit ultra-low noise electrical amplifiers to boost the signal.
- Possible gain in the detection process itself: when a controlled local oscillator (LO) is employed, the amplitude of the detected difference frequency can become larger than the amplitude of the original signal since the difference frequency signal is proportional to the product of the amplitudes of the LO and the signal. Thus very weak signals are captured by mixing the incoming signal with a strong local oscillator without any supplementary optical or electrical amplifiers. The detection gain can enhance the sensitivity of a heterodyne receiver 10-15 dB compared to a IMDD receiver [21].
- As the full complex amplitude is maintained in the, detection using phase or polarization-diversity receivers [22] becomes possible. This enables electronic equalization to efficiently and accurately post-compensate several detrimental effects [34, 35].

2.1 Optical remote heterodyne detection links

Optical remote heterodyne detection (RHD) avoids complicated phase or frequency locking at the receiver end because the reference laser line is provided remotely, which reduces the complexity of the system significantly compared to the conventional coherent heterodyne detection [36]. In RHD links two spectral lines, which are usually phase-correlated with a frequency difference equal to the desired MMW frequency, are transmitted through an optical fibre. The MMW signal is generated by heterodyning both spectral lines at the receiver using a photodetector. Because the spectral lines are generated optically, this method is capable of generating extremely high MMW frequencies. In practice the MMW frequency is limited by the bandwidth of the photodetector or circuitry that are used to detect and process the signal.

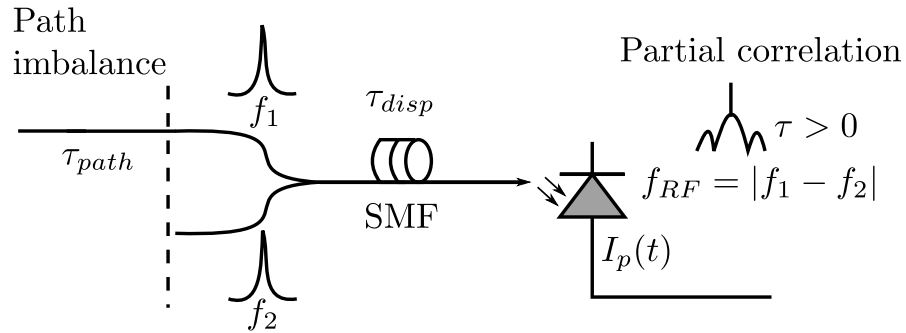


Figure 2.1: The configuration of optical RHD links. In reality the laser lines are only partially correlated due to the imbalanced propagation paths of the laser lines and dispersion effects [37].

On the other hand RHD also requires a stable dual-wavelength laser source which can provide the phase-correlated laser lines. Therefore many different approaches have been proposed for dual-wavelength optical transmitters:

- Dual-wavelength lasers operating in two longitudinal modes have been investigated [38].
- LDs with two transverse modes operating in a single longitudinal mode have been reported [39].
- High quality MMWs have been generated using external modulators by suppressing one of the modulation sidebands [40] or the optical carrier [41]. In these techniques only a single-mode laser is required to operate at continuous wave (CW) mode, and external modulators are employed to modulate the intensity of the laser output. Although these transmitters are stable and both transmitted spectral lines are from the same laser source, transmitter structures are complex and external modulators increase insertion losses.
- Injection locking has also been used to generate MMW signals. In this case the modulation sidebands of an intensity modulated master laser are fed into one or two slave lasers. Moreover the free-running frequencies of the slaves are designed to match with the sideband frequencies. When the injected optical power is suitable, the slaves become locked to the sidebands of the master laser. If the outputs of the slaves (or a slave and the master laser) are coupled to a photodetector, the configuration generates a narrow linewidth MMW signal [42, 43]. In practice the locking bandwidths are narrow because the configuration suffers from stability problems. Consequently feedback loops are usually used to increase the stability of injection locked lasers [44].

High spectral purity is achieved if the laser modes share the same cavity and gain medium because both modes experience the same dominating noise mechanisms, and the common noise is rejected at the photodetector when the instantaneous phases of the laser lines are subtracted [45]. Due to the common mode rejection effect, phase noise is reduced significantly and a high quality MMW signal can be generated [46].

2.2 Sensitivity degradation of RHD receivers

Ideally the phase-correlation of the spectral lines is maintained during the transmission in RHD links, resulting in highly phase stable MMWs [24]. However, in practice, optical links contain several impairments such as intensity noise, phase noise, polarization fluctuations, dispersion, and various non-linear effects that deteriorate the signal quality, disrupt the phase-correlation effect, and reduce the BL product of RHD links. Due to nonidealities, the receiver sensitivity decreases and the signal power should be increased in order to maintain the required BER value. The increase of optical power is known as power penalty. This section focuses on several sources of power penalties that can deteriorate the receiver sensitivity in RHD links.

2.2.1 Intensity noise

Stimulated emission becomes the dominant photon generation process when semiconductor laser is operating above the threshold current. Nevertheless, spontaneous emission is still present. The randomness of spontaneous emission events causes that lasers always experience some kind of fluctuation in the output power, even in CW mode. Even though spontaneous emission corresponds to a small amount of generated photons, these photons have a significant effect on intensity noise. In spontaneous emission the recombination of an electron-hole pair generates a photon. For this reason each spontaneous emission event decreases carrier density, introducing also a change in the optical gain and refractive index. These perturbations within the laser cavity lead to intensity and frequency (phase) fluctuations via relaxation oscillations [31,47]. The power fluctuations of a laser are usually expressed in terms of relative intensity noise (RIN) and its contribution to the noise current of a photodetector can be approximated by [48]

$$\langle i_{RIN}^2 \rangle = (\mathcal{R}P_{in})^2 10^{(\text{RIN}(\text{dB})/10)} BW, \quad (2.1)$$

where RIN(dB) is the measured average value of RIN over the noise bandwidth in decibels. RIN is efficiently suppressed by using balanced photodetectors to receive the signal [49]. Balanced detectors also reduce the direct detection components from the detected signal. These properties make balanced detectors a more preferable

solution for detecting the beat signal than ordinary single-port detectors. The MMW signal generated by a balanced photodetector can be expressed as [7]

$$I_p = 2\mathcal{R}\sqrt{P_{in,1}P_{in,2}}\cos(2\pi f_{RF}t + \Delta\phi), \quad (2.2)$$

where $P_{in,1}$ and $P_{in,2}$ are the optical powers of the detected laser lines, and $\Delta\phi$ is the phase difference. At this point it is worth noticing that the photocurrent is related to the product of $P_{in,1}$ and $P_{in,2}$. Hence the photocurrent of the beat signal can fluctuate even though the sum of $P_{in,1}$ and $P_{in,2}$ remains constant. This fluctuation is caused by mode partition noise (MPN) and it is discussed more closely in Chapter 5.

There are also many other noise sources in RHD links besides RIN, MPN, thermal, and shot noise such as phase-induced intensity noise (PIIN). In reality the transmitted spectral lines have a finite spectral width. When the phase noise of the laser lines interacts with CD, intensity noise is imposed to the MMW signal at the photodetector degrading the SNR [50]. The impact of PIIN on the SNR does not reduce the performance of receivers significantly in medium-haul systems even though the linewidth is relatively broad [50]. Nevertheless PIIN can become the dominant noise source in long-haul RHD systems as depicted in Figure 2.2. Contribution of PIIN to RIN is approximated by [51]

$$\text{PIIN}(f_{RF}) = 4\pi\Delta\nu\left(f_{RF}D\frac{\lambda^2L}{c}\right)^2, \quad (2.3)$$

where $\Delta\nu$ is the laser linewidth, L is the length of the optical fibre, λ is the optical wavelength, c is the speed of light, and D is the second-order dispersion parameter.

Reflections also increase intensity noise in optical links. Reflections emerge due to refractive index interfaces, located at the connectors and splices of optical fibres. They can build up external interferometric cavities causing multiple copies of the signal to propagate in a fibre. If phase-shifted copies are associated with chromatic dispersion, phase variations are converted to intensity noise that is enhanced by optical amplifiers [48]. Competing cavities can also cause instabilities within the internal laser cavity and increase the laser RIN [52]. Back-reflections are reduced by using connectors with for example angled end-facets. Optical isolators are also used to reduce back-reflections.

In practice, each optical amplifier degrades the SNR value somewhat due to spontaneous emission induced noise. Optical amplifiers not only generate spontaneous emission noise, but also enhance spontaneous emission from the previous amplification stages. Hence, amplifiers are also sources of amplified spontaneous emission (ASE) noise. Both spontaneous emission and ASE noise introduce additional mixing

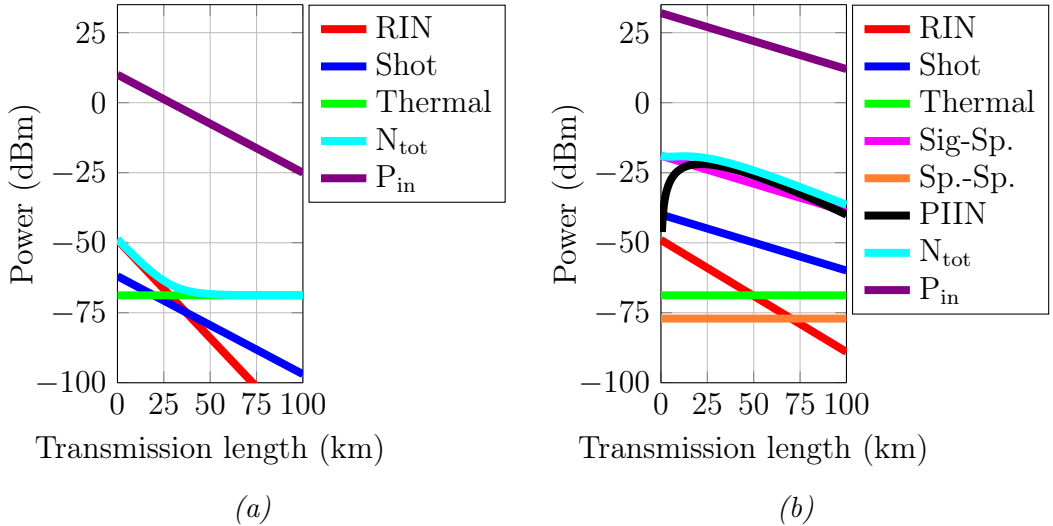


Figure 2.2: The noise levels of various noise sources, total noise (N_{tot}), and the received optical power (P_{in}) are estimated for two different kind of RHD links. (a) shows noise powers for a RHD link operating at $1.31 \mu\text{m}$ where the second order chromatic dispersion vanishes. (b) describes different noise sources for a RHD link operating at $1.55 \mu\text{m}$. The power of the signal is boosted with an optical pre-amplifier. The modelling parameters are specified in Appendix A.

products at the photodetector that affect the noise level of the generated photocurrent.

Typically only two additional mixing products bring significant contribution to the total noise as compared to the unamplified link. The first one is the mixing product between the ASE noise and the amplified signal known as signal-spontaneous beat noise. This noise is detected only in the electrical domain and it can be estimated using [48]

$$\langle i_{Sig.-Sp.}^2 \rangle = 4\mathcal{R}^2 G P_{in} S_{sp} BW, \quad (2.4)$$

where S_{sp} is the noise spectral density given by [48]

$$S_{sp}(f) = (G - 1)G_n h f / 2, \quad (2.5)$$

and P_{in} is the received unamplified optical power. In Equation (2.5) the amplifier gain is denoted by G . G_n is the noise figure, and h is the Planck constant. The second observable mixing product is generated when ASE noise beats against itself at the receiver. Spontaneous-spontaneous beat noise is expressed as [48]

$$\langle i_{Sp.-Sp.}^2 \rangle = 2\mathcal{R}^2 S_{sp}^2 (2B_{op} - BW) BW, \quad (2.6)$$

where B_{op} is the optical noise bandwidth. Signal-spontaneous beat noise is usually

more important in terms of link performance than spontaneous-spontaneous beat noise if the optical noise bandwidth is relatively narrow [53].

2.2.2 Phase noise

One of the most critical requirements for heterodyne detection is the spectral purity of the received signals, but phase noise has a much smaller effect on IMDD systems [31]. The reason for the importance of phase noise in heterodyne detection is obvious from Equation (2.2) as a differential phase change is related to the generated photocurrent. In order to keep the phase noise induced SNR penalty low, the phase difference must be relatively stable.

The short-term stability of the phase difference is often characterized through the linewidth of the generated MMW signal. If the laser lines are phase-correlated the common noise of the laser lines is rejected at the photodetector and the generated MMW signal can have an extremely narrow linewidth even with relatively broad optical linewidths [54]. However, dispersion induced phase noise broadens the spectral line of the MMW signal and narrow optical linewidths are also required for remotely provided laser lines to maintain low phase noise in the MMW signal [54].

Fundamentally the finite spectral width of continuously operating LDs is limited by two factors. The first one is the random events of spontaneous emission. Spontaneous emission is a completely incoherent mechanism that generates photons in the cavity of lasers. The generated photons have an arbitrary phase that causes the spectral broadening of laser lines. Spontaneous emission also indirectly contributes to the linewidth of a laser through intensity fluctuations as explained in Section 2.2.1.

The second factor that inherently affects the linewidth of LDs is caused by external perturbations, such as thermal noise or fluctuations in the injected carrier density. Temperature and carrier density fluctuations change the characteristics of the laser cavity and eventually introduce phase noise by inducing variations in the material gain and refractive index.

Besides the fundamental limitations set for the linewidth of LDs by the external perturbations and spontaneous emission, LDs have also many other sources of phase noise such as mode instability [55] and the existence of sidemodes [56] which can significantly increase the linewidth. Phase noise induced SNR penalty depends on the modulation formats and demodulation schemes, and it is usually described as a function of linewidth-data rate ratio $\Delta\nu/B$ [57]. Section 2.3.1 includes more detailed discussion about the values of $\Delta\nu/B$ ratio for different modulation formats and demodulation schemes.

2.2.3 Nonlinear effects

Typically guided optical communication systems exploit single-mode fibres in long-haul data transmission because multi-mode fibres suffer from modal noise and inter-modal dispersion [48]. However single-mode fibres have a small core diameter which induces a high intensity of light in the core, although the total propagating power is rather low. Hence single-mode fibres do not behave as completely linear channels at higher optical power levels. In long-haul links non-linear effects can accumulate over the transmission length and cause signal degradation through several different effects such as stimulated Raman scattering (SRS), stimulated Brillouin scattering (SBS), four wave mixing (FWM), and self-phase modulation (SPM) [4].

SRS is an inelastic scattering process where a photon loses its energy to an optical phonon and a lower-energy photon [58]. In pure silica SRS shifts the frequencies of the scattered photons with respect to the incident photons usually about 10–14 THz [59]. In single-mode fibres SRS requires relatively high power levels ($\sim 1\text{--}2\text{ W}$) before the scattered power starts to increase almost exponentially [58]. Due to the relatively high threshold power, SRS does not usually limit the performance of single channel links but it can induce crosstalk in WDM systems [4].

SBS in turn is an inelastic scattering process where a photon loses its energy to an acoustic phonon and a photon [58]. Acoustic phonons have much smaller energy than optical phonons, that take part in SRS, and therefore SBS induced frequency shifts are much smaller (order of a few GHz [4]). The threshold power is also much lower for SBS (of the order of a few milliwatts) and the small threshold power of SBS can limit the propagating power in single channel optical links [60]. After the threshold is exceeded a large amount of optical power reflects back towards the transmitter, causing optical power to saturate [61]. The threshold power depends on the linewidth of the optical signals [61], and modulation format as well as modulation speed [60]. Because the threshold power is inversely proportional to the number of amplifiers in the link, SBS can be a serious problem for long-haul links which employ many amplifiers [61].

FWM generates new spectral lines when at least two initial spectral lines interact with each other through the non-linear response of a material [59]. FWM is a phase sensitive process and the conversion efficiency depends on the phase-correlation of the interacting spectral lines [59]. Hence, the two phase-locked optical lines employed in RHD are particularly sensitive to FWM. Also polarization [62] and the spacing of the spectral lines [61] affect the mixing efficiency. FWM is a detrimental effect in communication links because the mixing products of FWM act like background noise and degrade the SNR. FWM can also imbalance the propagating laser lines, limit the maximum power per channel, and increase bandwidth requirements in RHD and

WDM links [4, 57, 63].

SPM is a consequence of the intensity dependence of the refractive index, which causes fluctuations in the phase and instantaneous frequency of spectral lines [4]. Phase and frequency fluctuations lead to the spectral broadening of spectral lines which in conjunction with chromatic dispersion causes signal distortion. In WDM systems the intensity of adjacent channels can fluctuate at the same time enhancing non-linear phase noise further [4]. Non-linear phase noise can be minimized using modulation formats where the intensity variations are small.

2.2.4 Dispersion and polarization mismatch

In fibre-optic channels dispersion effects can distort the signal and reduce the receiver sensitivity. In medium and long-haul communication links dispersion impairments emerge not only from chromatic dispersion (CD), but also from polarization-mode dispersion (PMD). At higher transmission speeds temporal spreading caused by different dispersion effects can limit the attainable BL product of communication links [26, 64]. The impact of dispersion effects depends on the fibre itself, applied modulation format, and the spectral width of the optical signal. Dispersion effects are usually reduced by compensating CD and PMD in optical or electrical domain. Dispersion induced effects and compensation methods are discussed briefly in this section.

Historically intermodal dispersion was the dispersion type that formed the first problem for fibre-optic communication when multi-mode fibres were introduced. Intermodal dispersion follows from the different group velocities of fibre modes. Due to intermodal dispersion, after a long propagation distance the receiver detects multiple copies of the signal arriving at slightly different times. To avoid intersymbol interference, the group delay between fibre modes caused by intermodal dispersion must be small enough, in order to provide a significant temporal overlap between fibre modes compared to the time period reserved for a bit. Unfortunately, intermodal dispersion is usually such a strong phenomenon that only small BL products can be obtained using multi-mode fibres. When the core radius is reduced, fewer and fewer modes can propagate within the fibre core. For single-mode fibres the core radius is so small that only the fundamental mode can propagate inside the core long distances. Although high-order modes can be excited in single-mode fibres, they experience high attenuation which allows them to propagate only very short distances. Because single-mode fibres eliminate intermodal dispersion and modal noise, long and medium-haul guided communication systems use single-mode fibres [65].

CD is a type of dispersion that occurs because the group velocity of the optical signal is a function of wavelength. CD spreads out the spectral components of the propagating light in optical fibres as they tend to travel at different velocities

through an optical fibre. Generally CD has two sources:

- Material dispersion: Different spectral components see different refractive index.
- Waveguide dispersion: Even if the refractive index would not depend on the wavelength, still the transverse modal profile is wavelength dependent, resulting in different effective refractive index values for different wavelengths.

Because both laser lines travel through an optical fibre in RHD links, CD induces a differential propagation delay ($\Delta\tau_{disp}$) between the laser lines [23]. Moreover, in some cases the laser lines do not necessarily travel exactly the same optical path in RHD links, and there might be a small offset delay due to a path imbalance $\Delta\tau_{path}$ that contributes to the total differential propagation delay given by [23]

$$\Delta\tau = |\Delta\tau_{disp} + \Delta\tau_{path}|. \quad (2.7)$$

The propagation path delay can be estimated by [23]

$$\Delta\tau_{path} = \pm \frac{\Delta L_{path} n_{core}}{c}, \quad (2.8)$$

where ΔL_{path} is the path length difference. The sign of the path imbalance introduced delay depends on the CD induced delay. If the path imbalance delays the same laser line than CD then $\Delta\tau_{path}$ is positive, otherwise it is negative. CD induced delay is expressed as [23]

$$\Delta\tau_{disp} = DL f_{RF} \frac{\lambda^2}{c}. \quad (2.9)$$

In Equation (2.9) D presents the second order chromatic dispersion parameter, L is the propagation length, f_{RF} is the frequency difference between the two spectral lines, and λ is the operation wavelength. As shown in Figure 2.3 a small path imbalance delay can reduce the differential delay when the transmission length is small. However, when the transmission length increases, the path imbalance delay cannot compensate the large propagation delay of the laser lines. If the propagation delay is not compensated otherwise, the laser lines sent at the same time arrive at different moments. If the arrival time difference is too large it may cause intersymbol interference, increase the probability of false decision, and eventually destroy the signal.

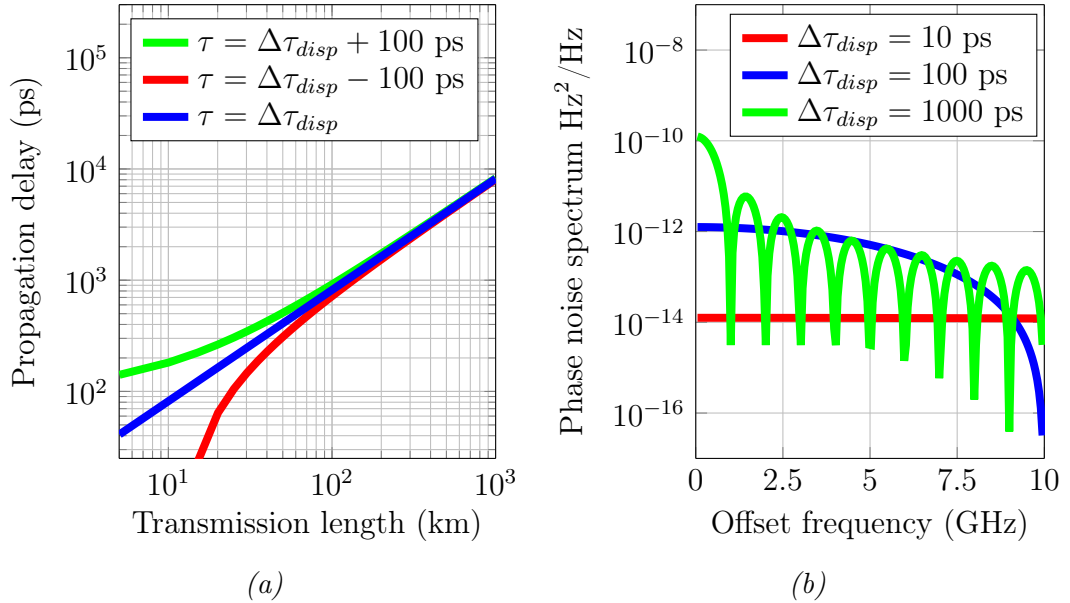


Figure 2.3: (a) CD induced propagation delay as a function of transmission distance calculated for different path imbalance delays. (b) phase noise spectral density estimated for different propagation delays. The laser linewidth is 10 MHz, $f_{RF}=60$ GHz, $\lambda=1.55$ μm , $D=17$ ps/nm·km, and the path imbalance delay is assumed to be negligible.

The propagation delay is conventionally counterbalanced in optical domain by filtering or using dispersion compensation fibres, for example. Unfortunately optical dispersion compensation is often costly, non-adaptive, and requires that dispersion management is distributed throughout fibre-optic links due to the non-linearity of optical channels [4].

Furthermore CD induces two observable detrimental effect in RHD links. The first effect is that CD also induces a power penalty directly, while the second one is that a non-zero differential delay results in phase noise that can limit the BL product of a link [23]. Assuming that the transmitted laser lines have a Lorentzian shape, phase noise fluctuation spectrum is approximated by [66]

$$S_{\phi}(f) = 2 \frac{\Delta\nu}{\pi f^2} \left(1 - \cos(2\pi f \Delta\tau) \right) \quad (2.10)$$

If the generated laser lines are perfectly phase-correlated, the differential delay results in a partial phase-correlation when the lines travel through a dispersive channel. This phase noise broadens the linewidth of the MMW signal and can induce a SNR penalty at the receiver whose magnitude depends on the modulation format and demodulation scheme.

However it has been shown that RHD links experience almost negligible power penalty caused by CD when compared to IMDD links that are used to generate

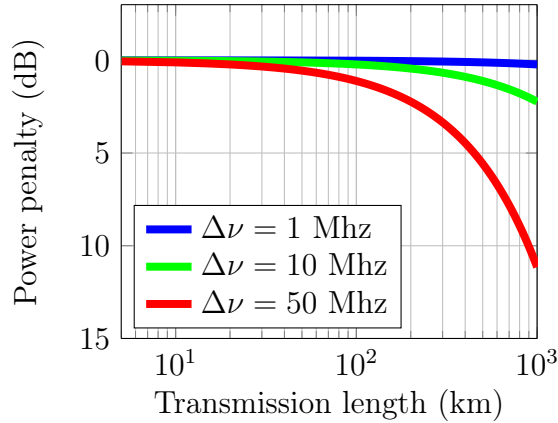


Figure 2.4: Dispersion penalty of a RHD link estimated for different laser linewidths. Chromatic dispersion causes a relatively small power penalty in RHD links although the laser linewidths are relatively broad. The calculations have been performed for $D=17$ ps/nm·km, $\lambda=1.55$ μ m, and $f_{RF}=60$ GHz.

MMWs [67]. In principle the optical spectrum in RHD links is comparable with the optical spectrum of single-sideband (SSB) intensity modulation. In double-sideband intensity modulation the signal power periodically fades as shown in Figure 1.3 because of CD [24]. In SSB modulation CD causes only relative phase changes between the spectral lines. Therefore the CD induced power penalty almost completely vanishes in RHD links even though the laser lines are broad. The propagation delay induced SNR penalty is estimated in RHD links using a simple formula [67]

$$SNR_{pen} = 10 \log \left(\frac{1}{\exp(-2\pi\Delta\nu\Delta\tau_{disp})} \right). \quad (2.11)$$

In practice all optical fibres have imperfections. These defects, as well as temperature, humidity or mechanical stress, can break the cylindrical symmetry of fibres such that optical fibres act as a birefringence material [68]. Hence the fundamental mode having two degenerated orthogonal polarization states, can split into two different modes propagating with slightly different group velocities [69]. Therefore the orthogonal polarization states experience a phase difference and propagation delay with respect to each other when both of them propagate through an optical fibre. The phase difference may fluctuate randomly in time, causing variations in the polarization states of the optical signals. This effect is referred to as polarization mode dispersion (PMD).

In RHD both carriers have ideally an identical state of polarization that leads to a photocurrent described in equation (2.2). As explained above, PMD can cause polarization mismatch, although the two carriers have the same polarization before being launched into an optical fibre. Polarization mismatch can also occur due to

imperfect optical components (isolators, couplers, etc.) or different initial polarizations. The other sources of polarization mismatch can mitigate or deteriorate the total SNR penalty caused by PMD [70, 71].

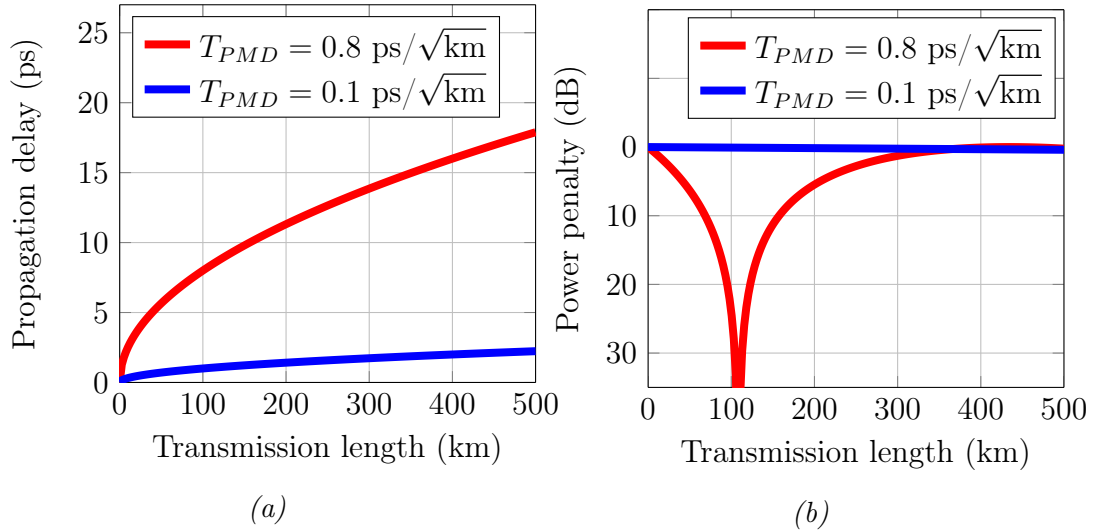


Figure 2.5: PMD induced propagation delay (a) and power penalty (b) are estimated for two different kind of T_{PMD} coefficients in a RHD link. $T_{PMD}=0.8 \text{ ps}/\sqrt{\text{km}}$ is a typical value for fibres used in old networks, while modern communication links have usually much smaller PMD coefficient such as $0.1 \text{ ps}/\sqrt{\text{km}}$ or smaller. $f_{RF}=60 \text{ GHz}$ and the splitting ratio $\kappa_{pol}=0.5$ are assumed in the calculations. This illustrates the worst case scenario and corresponds to 45 degree angle between a linear polarization state and the principal polarization axes.

PMD is a time-dependent random process, while a detailed analysis of practical systems requires a statistical approach [67, 72], it is possible to approximate PMD induced delay time between the carriers using a measured average value. The transmission distance of communication links is usually in the region where the propagation delay is proportional to the square root of transmission distance [69]. Thus, the PMD induced propagation delay is estimated by [69]

$$\tau_{PMD} = \frac{T_{PMD}}{\sqrt{L}}, \quad (2.12)$$

where T_{PMD} is the average proportionality coefficient. PMD induced power penalty, in turn, is expressed as [67]

$$SNR_{pen} = -10 \log \left(\frac{1 + f(\kappa_{pol}) + \cos^2(\pi f_{RF} \Delta \tau_{PMD} L)(1 - f(\kappa_{pol}))}{2} \right), \quad (2.13)$$

where κ_{pol} is the power splitting ratio of light launched into a fibre with respect to the principal axes and $f(\kappa_{pol}) = \cos(4 \arccos(\sqrt{\kappa_{pol}}))$. As shown in Figure 2.5, PMD can be a serious problem for old fibre links that have a relatively high PMD

coefficient. Fortunately, only a small signal degradation is expected in modern fibres where PMD coefficient is reduced. The propagation delay also depends on T_{PMD} but it is usually much smaller than the propagation delay of CD.

2.3 Modulation schemes

The modulation is a process where a low-frequency baseband signal is mixed with a carrier signal. From the communication theory point of view signal modulation is a key factor that determines the transmission properties of a signal. Recent needs for advanced modulation formats are motivated by the signal tolerance to transmission impairments (CD, PMD, non-linear effects, etc.), susceptibility to accumulated noise, transmission capacity, better reliability, improved power, and spectral efficiency.

Various factors have an impact on the choice of modulation scheme. Unfortunately there is no perfect solution for all these requirements and the modulation format is always a compromise that is the closest to the requirements of a particular application. The choice of modulation format depends on many parameters such as transmission speed, fibre type, transmission length, and frequency spacing.

The basic forms of digital modulation schemes are amplitude-shift keying, (ASK), frequency-shift keying (FSK), and phase-shift keying (PSK). These are considered in this section. More advanced formats, like the quadrature amplitude modulation, which is a hybrid of PSK and ASK, are not considered in this work, but an excellent description of high-order modulation formats can be found from [69].

The ASK is a digital modulation format associated with amplitude variations of the modulated signal. It uses a finite number of discrete amplitude values to represent digital data. Fixed amplitude values of ASK modulation are transmitted such that one of the discrete amplitudes is transmitted during a bit duration, while the phase and frequency of the signal remain constants during the modulation.

The ASK modulation format can be applied to RHD and IMDD links, but heterodyne detection implies a couple of differences compared to direct detection receivers. The amplitude variations cause unintentional phase changes in LDs and this leads to the degradation of the signal due to the phase sensitivity of heterodyne receivers. Consequently, the ASK modulation in RHD links is usually generated using external modulators, because external modulators can keep the phase of the transmitted signal relatively stable [4]. External modulators are also used to reduce spurious frequency modulation of the signal that can reduce the performance of coherent receivers [4]. However, the external modulators increase the size, cost, and losses of transmitters [69].

FSK is another of the basic digital modulation schemes in which digital data is encoded by varying the frequency of the carrier between discrete frequency levels. In the simplest form of FSK there are only two frequency levels. One frequency

represents '0' and the second frequency '1'. The number of the discrete frequency levels can be increased in order to improve the power efficiency but increasing the number of frequencies requires a wider transmission bandwidth [73].

FSK is less susceptible to intensity noise than ASK because non-linear processing can be used to reduce spurious intensity variations from the signal. It is also more tolerant to non-linear effects because the signal has ideally a constant amplitude. FSK signal can be generated without external modulators, exploiting the chirp of directly modulated LDs. On the other hand FSK modulation has also drawbacks such as low spectral efficiency compared to amplitude or phase modulation formats, and more complicated demodulation circuits than ASK.

The requirements for directly modulated laser sources in communication links employing the FSK modulation format typically include low spurious amplitude modulation and high frequency modulation (FM) efficiency up to the maximum modulation speed [74]. FM efficiency describes how much the operation frequency changes with respect to bias current variations, and it may depend strongly on the current variation frequency [57]. The frequency dependence is problematic because any non-uniformity in the FM efficiency can lead to a bit-pattern dependent behaviour [74].

PSK is a spectrally efficient digital modulation format. Typically PSK receivers can provide superior sensitivity compared to ASK and FSK ones [4]. On the other hand PSK modulation requires phase sensitive detection, making the demodulation circuits more complicated than in ASK or FSK formats.

PSK signal is generated by changing the phase of the signal and keeping both amplitude and frequency constant. The information is embedded to the phase of the carrier in a digital form. Binary PSK signal contains two fixed phases such that there is a phase shift of π between the logical symbols. Because the phase of the carrier contains the information, large phase fluctuations corrupt the transferred information. Thus, PSK requires that the phase of the carrier is stable and well-controlled. Phase stability sets also stringent requirements for the linewidth of the MMW compared to FSK or ASK modulation formats [75]. The requirements can be mitigated by introducing methods such as differential phase-shift keying (DPSK). DPSK requires phase stability only for a two-bit period because it compares the phases of adjacent bits to each other. Absolute phases are no longer needed as in PSK, which reduces linewidth requirements significantly [75]. For PSK and DPSK modulation formats external modulators are usually used to create the modulated signal optically [69].

2.3.1 Demodulation

Heterodyne receivers require a further stage where the frequency of the MMW signal is brought down to baseband and the information is extracted from the signal. This stage is also known as demodulation. There are various ways to create a mapping from the intermediate frequency to the baseband for different modulation methods. Most of these are well-known from radio and microwave communication systems. In this section several demodulation techniques for ASK, FSK and DPSK formats are explored.

As discussed earlier, phase information is preserved in heterodyne detection. This also reflects on demodulation methods that can be exploited to recover the data. Synchronous and asynchronous receivers are common examples that have been used to indicate differences between two different approaches to demodulate digital modulation formats using analog circuits. Synchronous receivers use an absolute phase reference to demodulate signals whereas asynchronous receivers do not have any absolute phase reference. Which demodulator is the best suited for a particular modulation scheme depends on what kind of signal is expected to be received. Particularly, noise characteristics and the modulation index (i.e. how much the modulated variable changes with respect to transmission speed) are important to know when designing a receiver for a particular application.

A straightforward implementation of an asynchronous ASK receiver can be done using a simple envelope detector. In the first place out-of-band noise is easily removed from the incoming signal by applying a bandpass filter directly before the envelope detector. After the envelope detection, the high frequency ripple is removed by a low-pass filter and finally the binary flow is determined based on a threshold circuit. The synchronous ASK receiver mixes a local oscillator signal with the incoming signal. Whenever the local oscillator has the same frequency as the carrier, a direct current component appears at the output. Unfortunately the level of direct current component depends on the phase between the local oscillator and the incoming signal and therefore a phase locked loop is needed to stabilize the phase difference. Low-pass filtering is employed to remove high-frequency noise before the output is fed into a threshold circuit for detection.

Asynchronous and synchronous FSK receivers can be implemented in a similar way than their ASK counterparts because a binary FSK signal can be ideally treated as two ASK signals operating at two different frequencies. If the tone spacing is much larger than the transmission speed, it is possible to extract one of the tones using an asynchronous or synchronous ASK receiver by centering the bandpass filter or local oscillator on one of the tones [76]. The performance of the receiver can be slightly improved by separating both tones using two ASK receivers in parallel such that

the bandpass filters or local oscillators capture the tones separately. Eventually the outputs of the ASK receivers are subtracted before they reach the decision circuit [77]. It is worth noticing that, unlike in ASK receivers, FSK receivers can be equipped with a limiter positioned just before the actual frequency discriminator. For this reason FSK receivers can result in a significant improvement in the SNR compared to ASK receivers [78]. The improved SNR however requires a higher bandwidth. The non-linearity caused by the limiter imposes a threshold effect in FSK receivers which leads to a rapid performance reduction if the SNR value falls below a certain threshold value [78].

Asynchronous receivers are more tolerant with respect to the phase noise of LDs which makes these receivers particularly attractive for wide deviation FSK and ASK formats. In order to keep the SNR penalty below 1 dB, the linewidth requirements are tight ($\Delta \nu < 5 \times 10^{-3}B$) [69] for synchronous receivers compared to asynchronous receivers ($\Delta \nu < 0.1 B$) [57]. Nevertheless synchronous receivers have theoretically a better sensitivity than asynchronous receivers if the linewidth is narrow enough [31, 79].

It is self-explanatory why it is not possible to implement asynchronous PSK receivers. However, it is possible to detect DPSK signals asynchronously using a delay line interferometer. By separating the bandpass filtered signal into two arms, delaying the second arm exactly one bit and mixing the signals, the phase difference between two successive bits can be determined [80]. The same method has also been used to demodulate FSK signals having a small tone spacing compared to the transmission speed [11]. FSK demodulation requires a delay in which the tone spacing experiences a π phase shift [81]. The receiver requires a relatively narrow linewidth for the incoming MMW signal ($\Delta \nu < 2.5 \times 10^{-3}B$ and $\Delta \nu < 3.0 \times 10^{-3}B$ for FSK and DPSK respectively [81]).

The demodulation schemes described above can be implemented using simple analog circuits and the theory behind these methods is well-established. Unfortunately the signal undergoes many linear and non-linear transmission impairments during the propagation through an optical fibre. Conventionally the linear effects on multiplexed channels are compensated at the same time by passing the overall optical signal through dispersion compensation filters, for example. However recent advances in analog signal processing (ASP) and digital signal processing (DSP) allow a different approach. Because the full complex amplitude can be recovered in heterodyne detection, the transmission impairments of an individual signal can be accurately compensated using an electronic circuit after the detection, which simplifies the structure of the transmission links. Although this approach has an additional impairment in the form of detector non-linearity, it has many attractive properties because the stability and performance of communication systems can be

greatly enhanced by applying adaptive and time-varying signal processing [22]. Post-compensation using electronic circuits is considered to be a flexible, cost-effective, and feasible solution for 100 Gb/s communication systems in the future [22]. Electronic post-compensation can also reduce non-linear distortions [82].

Futhermore DSP has a significant advantage over ASP. Digital receivers need an analog-digital converter that translates the signal into digital form, introducing simultaneously a low-level quantization noise. After the analog-digital conversion, the receiver induces only a negligible noise level to the signal in the signal processor itself. ASP instead, induces additional noise to the signal during the signal processing. This is a problem when circuits become more and more complex because noise can have a great impact on the receiver performance. On the other hand DSP requires analog-digital converters which are either unavailable, or costly and power-hungry at ultra high frequencies [83].

2.4 Advantages and difficulties in remote heterodyne detection

RHD has several advantages over IMDD links and conventional coherent heterodyne detection in optical MMW generation. The main benefits are:

- Negligible SNR penalty due to chromatic dispersion
- Signals having very high MMW frequencies can be generated
- No need for a local oscillator laser that is locked to the transmitted optical signal using complex electronic circuits
- It is possible to use advanced modulation formats and sophisticated signal processing tools to compensate transmission impairments because amplitude, frequency, and phase are recovered in the detection.

On the other hand the main limitation in RHD links comes from the light source that is used to generate two stable phase-correlated laser lines. Even though some solutions exist (injection locked lasers, external modulation techniques, etc.) they are usually expensive and have a high complexity. A dual-wavelength laser diode, that generates both spectral lines in the same cavity, could provide a low cost compact light source for RHD links with a high power efficiency, low coupling losses, and a tunable frequency difference. These properties make dual-wavelength lasers very desired for numerous applications that exploit RHD.

3. STRAINED MULTI-QUANTUM WELL DISTRIBUTED FEEDBACK LASERS

As discussed in Chapter 1, modern fiber-optic communication links usually employ a LED or LD to transmit optical signals. LEDs can provide simple and low cost light sources for short distance and low-speed communication links, but they are not suitable for high-speed long-haul communication due to their wide frequency spectrum, low modulation speed, and low efficiency.

LDs have high efficiency, fast response time, and narrow spectral width. LDs also emit coherent light that is easier to focus and couple into a single-mode fiber efficiently. Distributed feedback (DFB) lasers are a type of LDs that have an integrated diffraction grating placed along the active region of the guiding structure, which provides single longitudinal mode selectivity. DFB lasers are compact, robust, and can operate with low intensity and phase noise levels. These properties make DFB lasers very desirable light sources for high-speed long-haul communication. This chapter is devoted to quantum well based DFB lasers and LDs in general. The chapter reviews the basic operation of semiconductor lasers, single-, and multi-quantum well laser structures, establishing the theoretical framework for the laser model described later in Chapter 4.

3.1 Semiconductor band structure

A complex set of equations is needed to describe the behavior of semiconductor devices from the electronic, optical and thermal perspective, which are all involved in the semiconductor light sources. Although there are many different modeling targets and model accuracy levels, the electronic equations generally include the Poisson equation, the current continuity equations, the Schrödinger equation, the electrochemical equilibrium potential equation (Fermi level equation) and the carrier transport equations (e.g. Boltzman equation, drift-diffusion equation). The optical perspective of the semiconductor behavior is governed by the Maxwell equations or some approximation of them while the thermal perspective is modeled by the distribution of thermal sources/sinks and by the heat transfer equation. Besides the electronic, optical and thermal equations there are also the coupling equations between these three main behavioral domains (the carrier generation-recombination equations, the heat generation and absorption, and the material parameter equa-

tions, which give the material parameters variations with different variables such as temperature or electric field).

Solving the complete set of semiconductor equations is an enormous and computationally intractable task, particularly since the semiconductor crystals are composed of a vast number of tightly packed atoms that interact with each other. The accurate treatment of crystals leads to a complicated many-body problem that is computationally almost intractable. Therefore, many simplified models have been proposed to provide satisfactory accuracy with reasonable computational cost.

Without a great loss of accuracy, it is usually sufficient to consider only the behaviour of valence electrons (electrons of the highest occupied atomic orbitals), and assume that the other electrons are localized around the nuclei forming ions. Because the ions are much heavier than the electrons, the valence electrons respond to ionic vibrations almost instantaneously, and, therefore, the motion of electrons can be decoupled from the motion of ions [84]. This approximation simplifies the many-body problem to a many-electron problem which is still too complicated to solve in practice. The Hartree-Fock approximation leads to a practically solvable single electron problem by assuming further that each valence electron experiences only the fixed average potential of other electrons and the periodic potential of the ion lattice [84]. For the single electron problem there are several numerical methods such as the orthogonalized plane wave method [85,86], pseudopotential method [87], and $\mathbf{k} \cdot \mathbf{p}$ method [88] that can be used to seek numerical approximations for the exact solutions.

Due to the dense packing of atoms in crystals the wave functions of the individual valence electrons overlap. In the meantime the Pauli exclusion principle does not allow electrons to have exactly the same quantum state. Hence, the solutions of the single electron problem result in energy bands. Each of these bands defines a set of quasi-continuous energy levels, rather than discrete energy levels of individual atoms [89]. The energy states that the electrons can occupy lie within the energy bands $E_n(\mathbf{k})$, where n is the band index and \mathbf{k} is the wave vector associated with the wave packet of an electron. Although, the single electron Schrödinger equation has an infinite number of solutions at given \mathbf{k} , it is usually sufficient to consider only the bands that lie just above and below the Fermi energy known as the conduction band (CB) and valence band (VB)¹.

In solids there are forbidden energy ranges in which there are no solutions for

¹For many important semiconductors the VB splits into three branches close to the band maximum. The branches are referred to as split-off, heavy and light hole bands, where the latter ones are possibly degenerated. These branches can be conveniently approximated by a parabolic local approximation of the momentum-energy dependence close to the band maximum [90]. It is also possible to use the same parabolic approximation for the CB. In the parabolic approximation the electrons and holes are assumed to behave like free particles with a certain effective mass defined by the curvature of the energy-momentum dependence curve.

the single electron problem at a given value of the wave vector. A special feature of semiconductors is that the Fermi energy lies within a forbidden region, which appears between the CB minimum and the VB maximum. This energy range is called as the bandgap. Semiconductors have two different types of bandgaps, direct and indirect. In direct bandgap semiconductors the VB maximum and the CB minimum occur approximately at the same value of the wave vector, whereas in indirect bandgap semiconductors the wave vector of the CB minimum and VB maximum differ².

Because the bandgap is small in semiconductors, a valence electron can jump from the VB to the CB by absorbing thermal energy, thus leaving behind a vacant space in the valence band, which is referred to as a hole. Since electron states are closely spaced in the energy bands, an electron from another state in the valence band can easily occupy the vacant space, leaving behind another empty state, and leading to a movement of the empty space (hole) in the valence band.

Therefore a hole behaves like a positive-charge moving freely in the VB, similarly with the movement of excited electrons in the CB. The electrons in the CB and holes in the VB can take part in a collective carrier flow when an external voltage is applied to a semiconductor. When the temperature rises enough to have sufficient free electrons and holes the semiconductors become conductive. However, the thermal excitation is not sufficient to provide the conductivity required for most applications and the semiconductors are often doped by extra impurity atoms in order to tailor the conductivity and other material properties [92]. Dopant atoms with more valence electrons than the host semiconductor lattice atoms are employed to create an n-type semiconductor by introducing additional electron states below the CB edge, such that the supplementary valence electrons are easily excited to the CB by thermal energy. Dopant atoms with fewer valence electrons are introduced in the host semiconductor lattice to create a p-type semiconductor by adding electron state vacancies (i.e. filled hole states) close enough to the VB edge to be thermally excited. The dopant-increased carrier concentrations improve the conductivity of the semiconductor material.

3.2 Basics of semiconductor lasers

The laser is a device that amplifies and emits a coherent light beam by stimulated emission. There are different types of laser structures but the essential structural

²The probability of interband transitions depends strongly on the crystal momenta ($\mathbf{p} = \hbar\mathbf{k}$) of the initial and final states [90] because the conservation law of crystal momentum enforces a strict selection rule for interband transitions [91]. If the wave vectors of the initial and final state do not match, the selection rule requires that one or multiple phonons participate to the transition to ensure momentum conservation. The probability of a phonon-assisted carrier generation or recombination process is much smaller than the probability of carrier generation or recombination processes in direct-gap semiconductors, where phonon assistance is not necessary [69].

elements are: a gain medium to provide gain to the propagating optical field and structural elements to provide optical mode confinement and optical feedback in an optical cavity. The fundamental optical processes underlying the laser operation are absorption, spontaneous emission and stimulated emission:

- Interband absorption takes place if a photon has sufficient energy to lift an electron from the VB to the CB. When an electron is promoted to the CB, the absorption simultaneously generates a hole in the VB. Intra-band absorption takes place when a carrier (electron or hole) is further excited from an already-excited state to another, unoccupied higher energy state in the same band (but possibly a different subband).
- Spontaneous emission takes place because systems tend to reach equilibrium in the lowest energy states. In semiconductors the excited states have a certain average lifetime that defines how long an electron can occupy a certain excited state in the CB, until it spontaneously falls back into an empty state in the VB. Because this process also obeys the conservation laws of energy and crystal momentum [90], the energy difference between the lower and higher energy state is released to a photon in the process, while the momentum difference is compensated by a phonon (if it is the case).
- Due to time-reversal symmetry there is also a reverse process for the absorption: the stimulated emission [14]. In stimulated emission a photon can stimulate an excited electron in the CB to fall back into the VB such that another photon is also generated. The stimulated photon has ideally exactly the same frequency, direction, polarization, and phase as the stimulating photon.

There is also the non-radiative recombination (including Auger recombination, surface recombination and recombination at defects/traps), when the energy released from the recombination of a CB electron with a VB hole is transferred as heat to other carriers or to the lattice.

Gain

The stimulated emission is the dominating photon generation process in LDs. It is a photon multiplication process that amplifies the intensity of light in an avalanche-like manner. In order to get a net optical amplification, the stimulated emission rate must exceed the absorption rate. In thermal equilibrium the most likely optical process is the interband absorption and no lasing can occur due to stimulated emission.

The first efficient semiconductor lasers operating in continuous wave at room temperature were double heterojunction (DH) LDs, which are essentially p-i-n diodes

with a relatively thin (0.1-0.4 μm) layer of nominally undoped narrower bandgap semiconductor sandwiched between p and n-doped cladding layers with wider bandgap and lower refractive index. It is important to mention that from the three different types of bandgap alignment in heterojunctions (type I - straddling gap, type II - staggered gap, and type III - broken gap), which depend on the distribution of the bandgap difference between the CB and VB, the double heterojunction structures are regularly based on the type I straddling gap alignment. This is because this type of alignment ensures the confinement of both types of carriers in the low bandgap region. Therefore, only the type I straddling gap alignment will be considered in the following.

When a forward bias is applied to the p-i-n structure (i.e. electrical pumping), it enforces carriers to drift towards the undoped narrower bandgap active region from the opposite directions. Due to the higher bandgap of the cladding layers, the injected carriers are trapped within the active region. Carrier trapping in the active region can also be obtained when an externally-injected optical field is absorbed and generates the carriers (i.e. optical pumping). If the electrical or optical pumping power is sufficient, large concentrations of CB electrons and VB holes build up within the active region. This situation, known as population inversion, is the opposite of the thermal equilibrium when most of the electrons occupy the VB and the CB is almost empty. Once population inversion is obtained, the probability of a stimulated emission event to occur exceeds the probability of an interband absorption, and the photons propagating in the active region experience a net amplification.

Due to the multiple loss mechanisms in LD, the pumping power must be increased until the gain equals the total loss, before the lasing starts. The point where this happens is known as the laser threshold. Above the threshold, the carrier density does not increase significantly (and, accordingly, the gain remains close to the threshold value) because the supplementary pumping power is transformed by stimulated emission into laser output power.

Laser cavity: optical guiding and feedback

Since the stimulated emission requires not only population inversion but also a relatively high stimulating optical field cavity, almost all LDs employ an optical guiding mechanism and an optical feedback mechanism to provide high optical field intensity in the active region. The optical feedback increases the distance that photons travel in the cavity, it enhances the photon density that is needed to trigger the photon multiplication process of stimulated emission and it provides a selection mechanism by recirculating only some of the photons.

3.2.1 Occupation probabilities

When a semiconductor crystal is in the thermodynamic equilibrium it does not exchange matter and energy with its environment and the carrier concentrations remain constants in time. Under thermodynamic equilibrium the occupation probability of an electron is governed by the Fermi function

$$F(E, E_F) = \frac{1}{e^{(E-E_F)/(k_B T)} + 1}, \quad (3.1)$$

where E_F is Fermi energy. However, most of the semiconductor devices, including LDs and photodiodes, usually operate under non-equilibrium condition. The thermodynamic equilibrium can be disturbed, for example, if a device is illuminated or if an external voltage is applied to it. The perturbation changes the carrier distributions in the CB and VB away from the thermodynamic equilibrium distributions and, if the perturbation remains constant long enough, the system establishes a new equilibrium state. In this new non-thermodynamic equilibrium state it can be considered that electrons and holes have their own quasi-equilibrium states [93], and the occupation probabilities of carriers in the CB and VB can be determined separately through two Fermi functions and quasi-Fermi levels. The occupation probability for an electron state in the CB at a given energy E under non-equilibrium condition is expressed using the Fermi function with Fermi level $E_F = E_{F_c}$ (i.e. $F_c(E) = F(E, E_{F_c})$). The probability that an energy level E in the VB is filled by a hole is given by $1 - F_v(E)$, where $F_v(E) = F(E, E_{F_v})$ [93].

3.3 Quantum well lasers

The typical thickness of the low bandgap active region in DHs is of the order of 0.1-0.4 μm . However, the development of fabrication technologies has allowed the growth of thinner active regions ($\sim 5\text{-}20$ nm). The reduction in the active region thickness has been observed to result in drastic changes in the electronic and optical properties of the structure [94–96]. These changes are attributed to quantum mechanical effects that take place when the thickness of the active region becomes smaller or comparable to the carrier de Broglie wavelength [97]. As a result of the reduction in the active region thickness, the carrier motion in the layer growth direction, perpendicular on the layer thickness, becomes restricted, leading to a quantization of kinetic energy [97]. Because the quantization can be described by the well-known quantum mechanical one-dimensional potential well, these lasers are referred to as quantum well (QW) lasers. The other two dimensions of the low-bandgap region are much larger in QW lasers and in these dimensions the carriers behave like in the bulk semiconductor.

The reduced thickness of QWs split the continuous energy bands of the bulk QW semiconductor material into discrete energy subbands. Using the parabolic band approximation and assuming that the well is infinitely deep, the interband transition energy in a QW structure of thickness L_z can be expressed for a direct-gap semiconductor as [97]

$$E_{\vartheta,\varsigma}(\mathbf{k}) = E_g + \frac{\hbar^2(\pi\vartheta/L_z)^2}{2m_e^*} + \frac{\hbar^2(\pi\varsigma/L_z)^2}{2m_h^*} + \frac{\hbar^2|\mathbf{k}|^2}{2m_r}, \quad \begin{matrix} \vartheta = 1,2,3,\dots, \\ \varsigma = 1,2,3,\dots, \end{matrix} \quad (3.2)$$

with the in-plane wavevector $\mathbf{k} = (k_x, k_y)$ and the reduced mass $m_r = m_e^*m_h^*/(m_e^* + m_h^*)$, where m_e^* and m_h^* are the effective masses of the electron and hole participating in the transition, respectively.

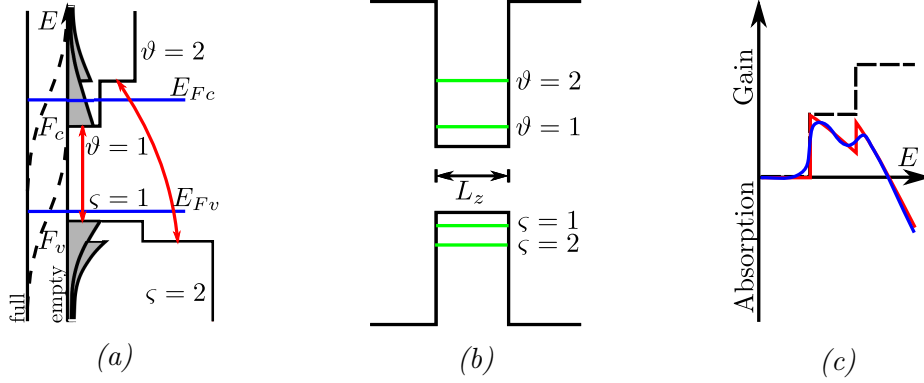


Figure 3.1: (a) reveals the step-like density of states in QW structures and indicates allowed interband transitions. It also depicts the occupation factors and filled states in the CB and VB. (b) shows the band structure of a typical type I QW and the first two subbands. (c) is a sketch of a type I QW gain spectrum. The blue curve presents the gain spectrum with gain broadening (by convolving the material gain with a Lorentzian lineshape function) and the red one gives the gain spectrum without broadening.

The energy of the split-off band is relatively and far away from the heavy (HH) and light hole (LH) bands and, therefore, it does not significantly influence the optical transitions. Hence the optical transitions are usually considered taking into account only heavy and light hole bands. Although the band structure of a QW contains many subbands, only certain type of interband transitions are allowed while others are forbidden. The forbidden transitions follow from the fact that optical transitions in QW structures must satisfy several selection rules:

- The energy must be conserved in the transitions.
- The in-plane wave vector fulfills the conservation law of momentum $\Delta\mathbf{k} = 0$ [98].

- The subband quantum number conserves in the transitions between the subbands of the CB and VB, (i.e. $\vartheta = \varsigma$) [97].
- The relative strengths of interband optical transitions involving TE and TM modes depend on the final VB state and some transitions do not occur (i.e. TE transitions between CB - HH, CB - LH, and CB - SO have relative strengths of 1/2, 1/6 and 1/3, respectively while TM optical transitions do not occur between CB and HH states and have 2/3 and 1/3 relative strengths for CB - LH and CB - SO, respectively).

The material gain depends mainly on three factors; the occupancy probabilities³, the density of states (i.e. the number of available states per unit energy per unit volume), and transition probabilities⁴. It turns out that the band structure of QWs leads to a step-like density of states [98]. Due to the abrupt increase in the density of states, one would predict that also the gain has an abrupt increase after each subband edge, because the transition probability under \mathbf{k} -selection rule is approximately constant with respect to photon energy [99]. This is not what has been observed and the gain spectrum of a QW laser is much smoother than expected. Two primary causes for the smoothness have been proposed. According to the first one, the tails follow from the violation of the strict \mathbf{k} -selection rule, causing an energy dependence of the transition matrix element [100]. The second explanation rises from the broadening of transition energies due to the various intraband scattering processes between carriers and phonons (which are induced by crystal inhomogeneity and many-body effects) [97, 101].

The density of states in the VB actually consists of two sets of overlapping steps. One series correspond to the subbands of the HH band and the second set is related to more sparsely spaced LH subbands. Although, the transition probability is larger for CB-LH transitions in TM polarization than the transition probabilities for CB-LH or CB-HH transitions in TE polarization [99], typically the material gain is higher for TE polarization due to the higher hole density in the HH subbands. In TE polarization CB-HH transitions have higher transition probability than CB-LH transitions [99].

³Because a necessary condition for an emission event in a semiconductor requires that the initial state E_2 in the CB is filled and the final state E_1 in the VB is empty, the occupation factor for an emission event F_e is given by $F_c(E_2)(1 - F_v(E_1))$. On the other hand the occupation factor for an interband absorption event F_a is governed by $F_v(E_1)(1 - F_c(E_2))$, since an absorption event can only occur when there is an empty state in the CB to where a valence-band electron can jump. The condition for positive net gain and population inversion in a semiconductor is given by $0 < F_e - F_a = F_c(E_2) - F_v(E_1) \implies E_{F_c} - E_{F_v} > E_2 - E_1 = hf$.

⁴The transition probabilities are not explained in this work, but it is worth mentioning that they depend on the transition matrix element that makes interband transitions polarization dependent in QW lasers [99]. It is also proportional to the overlap integral of the electron and hole envelope functions [97].

QW lasers can provide several advantages over conventional DHs. For example, QW structures are less susceptible to temperature variations and they experience smaller chirp than DH structures [98]. QWs also have a small active volume, which decreases the transparency current density. In QW lasers the energy levels have a strong dependence on the width of the well L_z . By adjusting the well width, the emission and absorption wavelengths can be tuned without changing the composition of the active region material. The main advantage of QWs, however, comes from the possibility to apply strain in the active region. Strained QW structures are considered later in Section 3.3.3. The step-like density of states is also known to improve the slope of material gain with respect to the change in the carrier density at low carrier densities [97, 102]. However, there is also a price to pay from the step-like density of states, as the gain saturates at high injection levels. Due to the gain saturation, the maximum gain of a fully-inverted subband does not necessarily produce enough gain to compensate losses until the second subband starts to fill up. Another drawback of QWs can sometimes be considered their small optical confinement, due to the narrow thickness of the active region. However, there are many situations when a small optical confinement factor favors the desired characteristics of the laser.

3.3.1 Separate confinement heterostructures

Since both the photon flux and material gain vary across laser structures, it is convenient to define the modal gain G_m to describe the net average increase rate caused by stimulated emission per unit length for the photon flux inside the laser cavity. The modal gain is determined by a weighted average of material gain over the cavity volume [102]

$$G_m = \frac{\int g(\mathbf{r})|\mathbf{E}(\mathbf{r})|^2 dV}{\int |\mathbf{E}(\mathbf{r})|^2 dV}, \quad (3.3)$$

where $g=g(\mathbf{r})$ is the net material gain per unit length that characterizes the local net stimulate emission rate.

Since a QW is very thin and only a small portion of the optical power is aligned with the active region, single QW structures comprising just the QW and cladding layers are not used in practice. A structure referred to as separate confinement heterostructure (SCH) is generally employed to increase the overlap between the photon flux and the QW-based active region (i.e. to increase the transverse optical field confinement in the QW). In the SCH structure the QW is surrounded by intermediate bandgap waveguide (WG) layers, which in turn are embedded between wide bandgap p- and n-doped cladding layers. Since usually higher bandgap is

associated with reduced refractive index, the WG layers have a refractive index lower than the QW and higher than the cladding. Hence, because the WG layers are significantly thicker than the QW, the SCH structure optical waveguiding is provided by the WG layers (and their refractive index contrast to the cladding layers), relatively independent of the thickness and refractive index of the QW. In the SCH structures the QW-to-cladding potential barrier is divided in two steps: the QW-to-WG and the WG-to-cladding potential barriers.

The bandgap and the corresponding refractive index distribution are essential in the design of SCH structures. A large bandgap and corresponding large refractive index difference between the cladding and WG layers leads to a good optical confinement but poor carrier confinement if the QW-to-WG bandgap difference is reduced. This increases the carrier leakage out of the QW and eventually increases the threshold current. On the other hand, if the WG-to-cladding bandgap and corresponding refractive index difference is small, it typically results in a good QW carrier confinement, but poor optical confinement (due to the reduced WG-to-cladding refractive index contrast), which reduces the modal gain [103].

Compositional grading of the WG layer material (commonly known as graded index, GRIN) is sometimes employed such that the WG layer bandgap decreases continuously towards the QW. The grading has the advantage that it introduces a potential gradient, which which pushes carriers towards the QW. This reduces the number of occupied states in the WGs which, in turn, causes a reduction in the threshold current [104] and increases the quantum efficiency. The built-in electric field may also affect the modulation bandwidth of QW lasers by making the the carrier transport faster.

The claddings layers are usually highly doped, which improves the flow of the injected carriers, but, in order to reduce internal losses due to free-carrier absorption in the areas with high optical field intensity, the WG layers are, generally undoped. There are two elements which have a major contribution to the carrier transport in SCH structures [105]

- the carrier transport time through the WG layers
- the carrier capture time by the QW

In graded index (GRIN) structures, bandgap variation assists carriers to move across the WG layers, inducing a noticeable reduction of the carrier transport time compared to the ungraded structure with the same WG thickness [106]. Nevertheless, this improvement may be counter-balanced by the fact that the GRIN structures usually achieve their maximum optical confinement for larger thickness than constant composition WG layers [105, 107]. Although GRIN structures can reduce the band

filling of WGs as well as the carrier capture time [106], GRIN-WGs are not preferable in all circumstances, especially when high FM efficiency is desired [108].

The width of the WG layers requires optimization both for the step-index constant-composition and for the GRIN types of SCH structures. Thick WG layers lead to a long carrier transport time, whereas narrow WGs reduce the optical confinement and may increase the parasitic capacitance of the structure [105].

3.3.2 Multi-quantum well structures

When LDs are directly modulated, the maximum attainable digital modulation speed is determined by many factors, the most important being the photon and carrier lifetimes. The photon lifetime defines the average time a photon spends in the laser cavity before it is absorbed or emitted through the laser facets. The photon lifetime is usually of the order of a few picoseconds in edge emitting lasers, and this sets the theoretical upper limit for the modulation speed of a LD. The carrier lifetime, in turn, gives what is the average time a carrier spends in excited state, before it falls into the ground state. Below the threshold, the carrier lifetime is defined by the rates of non-radiative recombination and spontaneous emission. Hence, the lifetime is relatively long ($\sim 1\text{-}4$ ns). Above the threshold, the carrier lifetime is substantially smaller due to the much higher stimulated emission rate.

When the LD pumping is increased, the modal gain climbs up, the carrier lifetime declines and the maximum attainable modulation speed rises. Unfortunately, the modulation speed cannot be increased indefinitely being limited by the carrier-photon laser self-resonance frequency, which is given by the carrier and photon density relaxation oscillations. It has been observed that a large photon density, short carrier lifetime, short photon lifetime, and high differential gain (i.e. the slope of the modal gain with respect to carrier density) increase the carrier-photon resonance frequency and enable faster direct modulation [109].

QW lasers have a modal gain which rises rapidly after the carrier density exceeds the transparency value, due to the step-like density of states. However, when the modal gain increases, it experiences a saturation because the volume of the thin QW is small and there is a relatively small number of states to be inverted at each subband.

To overcome this difficulty, multi-quantum well (MQW) structures, containing several generally identical quantum wells, are used, particularly in high-speed directly modulated LDs. The multiple wells are separated by barrier layers that usually have a smaller bandgap than the WGs, but a larger bandgap than the wells. This structure improves the optical confinement by increasing the overlapping of the optical field intensity distribution over the total volume of the active region. Hence, for a given modal gain, the carrier density associated with one well becomes

smaller [110], and a higher carrier density is required to saturate the modal gain [111]. This implies that MQW structures can generally provide a higher differential gain than SQW structures when the modal gain is high. Moreover, there is an extra differential gain enhancement less carriers are wasted to fill states within the WGs [112]. The higher differential gain of MQW lasers has been shown to improve their modulation bandwidth [105]. The decision using SQW or MQW structures depends on many factors, including the laser losses and the desired laser characteristics. The MQW structures are particularly required when laser losses are high, since the SQW structures might not provide enough gain. MQW lasers have usually superior modulation performance, largely due to the higher differential gain, sometimes narrower emission linewidth increased, slope efficiency and reduced threshold dependence on temperature (largely due to reduced carrier leakage to the claddings)⁵. On the other hand each well in the MQW lasers requires the same transparency carrier density as the well in SQW lasers. Hence, at low loss levels SQW lasers usually perform better than MQW lasers when the rest of the structure remains identical. Hence, at low loss levels the SQW lasers usually perform better than MQW ones.

So far it has been assumed that the carrier density is uniformly distributed over the wells in MQW lasers. Although uniform carrier distribution is desired, in reality this is hard to achieve when carriers are distributed over many QWs. To avoid the problems caused by non-uniform carrier distribution, the MQW lasers require accurate investigation of the carrier transport and capture, including carrier re-capture and transport between the wells.

Besides QW carriers capture, there is an opposite process in which carriers can escape from the QWs. This is a detrimental phenomenon for SQW structures, but vital for MQW structures. Without it the MQW lasers would have highly non-uniform carrier distributions from one well to another. Therefore in MQW structures it is important to design the active region in such a way that the carrier capture of the whole MQW structure is optimized while the carriers are uniformly distributed among wells [114].

At the normal operating temperatures of LDs, the carriers can escape from QWs by the aid of thermal energy. In MQW structures the electrons can be transferred from one QW to the next by tunnelling through the barriers. The dominant transport mechanism is the faster one [105]. The thermionic emission time is independent of barrier width, but it strongly depends on the potential barrier height. On the

⁵The smaller state filling leads to a smaller chirp and reduction in linewidth enhancement factor ($\alpha_{\mathcal{H}}$) as the number of QWs increases [113]. The reduced carrier threshold density (N_{th}) and increased active region volume, combined with the smaller linewidth enhancement factor contribute to emission linewidth ($\Delta\nu$) reduction. On the other hand increased internal losses and higher spontaneous emission factor lead to emission linewidth increase with the number of QWs. Hence, the optimization of the number of QWs in order to minimize the laser emission linewidth is not straightforward [113].

other hand the tunnelling time is a function of both height and width of the barriers [105]. Low potential barriers leads to shallow wells with higher thermionic escape and tunneling, which result in uniform carrier distribution among the wells but higher carrier leaking out of the MQWs, which increase band filling of WGs [112] and losses [115], decreasing the modal gain. On the other hand, high potential barriers reduce both the thermionic emission and tunneling, leading to non-uniform carrier distribution among the wells. Thick barriers eliminate the tunneling and the remaining thermionic emission both couples the QWs and induces carrier escape to the WG, which are contradictory effects, for which it is difficult to achieve a good compromise.

Thin barriers increase the carrier tunnelling, improving the uniformity of carrier distribution among the wells without affecting adversely the carrier escape from the MQWs. However, very thin barriers may lead to the coupling of QWs [116]. When inter-well coupling occurs, it splits the subbands of the well into minibands increasing the density of states and making the population inversion more difficult. Because strong inter-well coupling smears the step-like density of states, it is usually an unwanted phenomenon. Relatively high potential barriers are preferred in order to limit the carrier escape from the QWs while the QW coupling and relatively uniform carrier distribution among the wells is improved by employing thin enough barriers for providing enough tunneling without creating minibands.

3.3.3 Strained quantum well structures

The laser performance can be improved when strained QWs are used. Strain is achieved by growing one or multiple thin layers of semiconductor material on top of a substrate such that the substrate material and the layer material have slightly different lattice constants. The bonds between the thin layer ions and the substrate ions prevent the thin layer ions from being spaced with their characteristic/native lattice constant. As the thin layer thickness increases, the stress rises until the critical thickness is reached and the strain relaxes through misfit dislocations [117]. Below the critical thickness, when the native lattice constant of the thin grown layer is smaller than the substrate lattice constant, the thin layer ions are forced to sit farther apart in the layer plane and the strain is referred to as bi-axial tensile strain. Conversely, when the native lattice constant of the thin grown layer is larger than the substrate lattice constant, the thin layer ions are forced to sit closer in the layer plane and the resulted in-plane strain is called tensile strain. The in-plane lattice constant variation under biaxial strain is accompanied by an opposite variation of the lattice constant along the direction perpendicular on the layer plane, according to the Poisson ratio. Also, due to the various structures and distributions of the crystal cell atoms the resulted strain has both hydrostatic and shear components (the

hydrostatic deformation being associated with the variation of the average spacing between ions, and the shear deformation being associated with the variation of the crystal cell angles).

The strain modifies the band structure of QW structures in different ways depending on the crystal cell and band structure type. The changes affect particularly the valence band structure since the hole binding energies and movement are more affected by the crystal cell ion distribution. The hydrostatic strain changes the separation between the energy bands, while the shear strain breaks the degeneracy of light and heavy hole bands and modifies the effective mass of holes [118]. Under compressive biaxial strain the bandgap is increased, the HH energy level is shifted above the LH energy level and the HH effective mass is reduced, while under tensile bi-axial strain the bandgap is reduced, the LH energy level is brought above the HH level and the LH effective mass is increased.

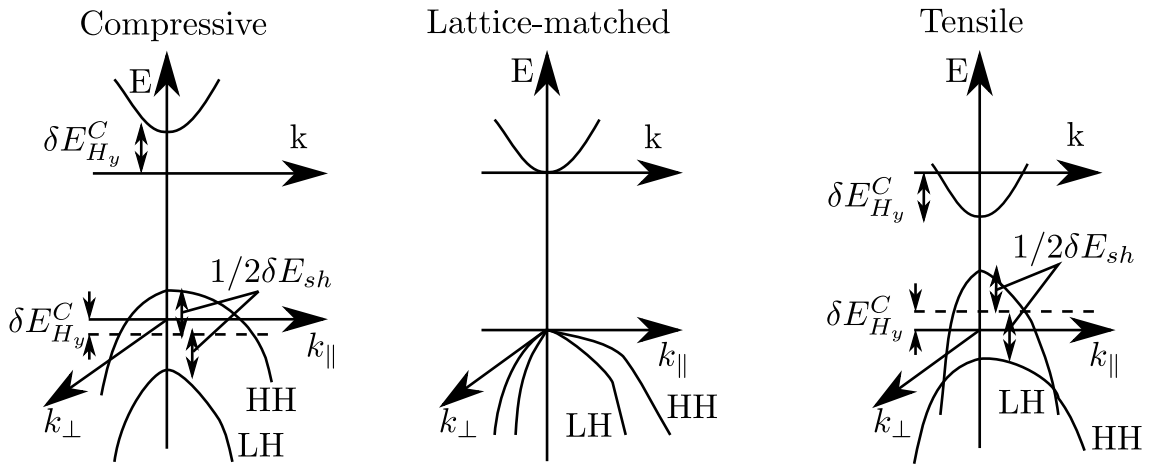


Figure 3.2: Band structure distortion due to lattice strain. Adapted from refs. [119, 120].

Strained QW structures have shown significant reduction in the threshold current density mainly due to lifting the HH-LH band degeneracy, which reduces the density of states and enables population inversion at lower injection levels [111, 121, 122]. Moreover, reduced carrier density is contributing to the reduced temperature sensitivity, which is derived from reduced carrier leakage, Auger recombination suppression of the valence band absorption [123]. Strain also affects the polarization selectivity of QW lasers. The compressively strained QWs emit only in TE polarization, while tensile strained QWs emit more in TM and less in TE polarization [117]. Other advantages of strained QW lasers are decreased spectral linewidth [124], smaller spontaneous emission rate (owing to the smaller transparency carrier density), better quantum efficiency [125], and enhanced modulation speed (due to the increased differential gain).

3.4 Transverse laser structures

In the edge-emitting lasers the light propagates along the p-i-n-junction plane. When Fabry-Perot resonator cavities are used the laser cavity is usually delimited longitudinally by cleaved facets, which act as partly reflective mirrors. Both the carrier transverse population inversion and the transverse optical field confinement do not only provide the conditions for stimulated emission but can also ensure single transverse mode operation. The potential barriers between layers (particularly the QW-to-barrier/WG in QW lasers) provide the vertical carrier confinement that helps in achieving the population inversion, while the vertical optical confinement is ensured by the SCH structure. Limiting the thickness of the active region as well as the thickness of the WG layers and WG-to-cladding optical contrast ensures single vertical mode operation.

Two types of methods are commonly used to ensure lateral carrier and optical field confinement and prevent the excitation of higher order lateral modes in edge-emitting lasers: index and gain guiding. In gain-guided lasers the lateral confinement is obtained by spatially varying the gain in the lateral direction. This is usually performed by restricting the current flow laterally to a narrow stripe (5-10 μm) along the longitudinal direction of the laser cavity. Although the current density spreads laterally when it flows towards the active region, the highest current density is concentrated just beneath the contact. Laterally elsewhere the current density is so low that the population inversion is not achieved and the active layer is absorbing. Hence, the laterally varying gain in the active region confines the stimulated emission laterally, inducing the lateral gain guiding of the optical field.

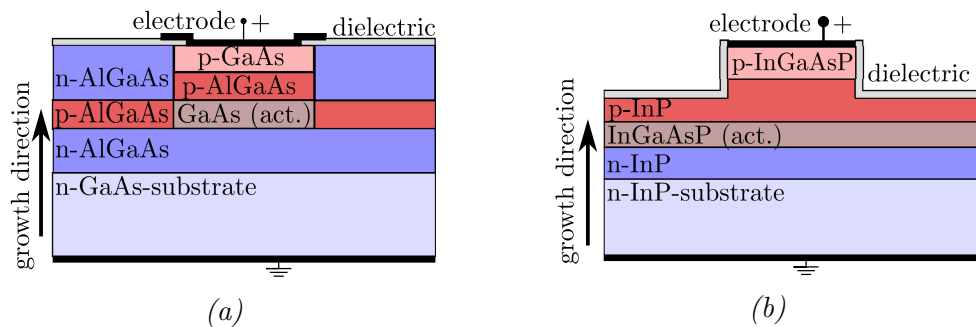


Figure 3.3: Examples of (a) buried heterostructure laser and (b) ridge waveguide laser transverse structures.

Index-guided lasers introduce a lateral variation in the refractive index, generally on top of some form of lateral gain guiding. There are several ways to fabricate index-guided lasers, but they are mainly based either on varying the thickness of the semiconductor layers above the active region (like in ridge waveguide lasers) or on inducing a lateral discontinuity in the semiconductor material (by etching and

re-growth, like in buried heterostructure lasers).

The typical ridge waveguide structure employs a ridge is etched on top of the active region, which may be subsequently embedded in a dielectric material. The bias current is injected (with limited lateral diffusion) through the ridge into the active region, overlapping to a large extent with the optical field, which is confined laterally by the lateral contrast of the vertical effective refractive index. The structure is both index and gain guided laterally but since the lateral index contrast is relatively small (i.e. weakly index guided) the structure also relies on the relatively high gain guiding provided by the limited lateral extension of the current flow through the active region.

The strongly index-guided buried heterostructure lasers can be fabricated by etching a narrow stripe of the active region and subsequently embedding it into a lower refractive index non-conductive semiconductor material. The lateral extension of the current flow and the lateral confinement of the optical are given by the lateral extension of the un-etched active region stripe. While this structure is both gain and index guided, the index guiding is usually so strong that it dominates the lateral guiding of light. Index-guided lasers have superior mode stability, lower threshold, higher beam quality, and better linearity compared to gain-guided lasers. Usually strongly index-guided lasers have even better characteristics than weakly index-guided lasers, but their fabrication is more complicated and expensive [126].

3.5 DFB lasers

DFB lasers are edge-emitting lasers having a periodical variation of the (effective) refractive index on the longitudinal direction (along the direction of light propagation). The longitudinal periodicity provides constructive interference of the reflections from refractive index variation only for wavelengths obeying the Bragg condition

$$2n_{eff}\Lambda = m\lambda_B, \quad (3.4)$$

where Λ is the variation period, λ_B is the Bragg wavelength⁶, n_{eff} is the effective refractive index, and m is the grating order.

This creates a feedback mechanism that selects only the longitudinal mode with the closest wavelength to the Bragg wavelength. The periodic structure is also commonly denominated as a 'grating', while the 'distributed feedback' name is derived from the fact that the feedback is distributed along the grating in the laser cavity.

The longitudinal variation of the (effective) refractive index is usually provided

⁶For a uniform grating there exists a particular wavelength, known as the Bragg wavelength (λ_B), at which the partial reflections are out-of-phase and the propagating light waves completely cancel each other, causing destructive interference.

by etching a corrugation close enough to the active region (in order to provide good overlapping with and coupling to the optical field), and subsequently embedding it by regrowth with a semiconductor material of different refractive index (thus creating a longitudinal buried grating structure). The buried grating fabrication requires that the epitaxial growth process is stopped at some point and the epiwafer is taken out from the growth chamber. Then the corrugation is etched onto the surface of the wafer. After cleaning, the epiwafer is set back into the growth chamber where the rest of the epilayer structure is grown over the corrugation (with the material grown immediately on top of the corrugation having a different refractive index than the corrugated material). A second processing stage follows to define the surface features (e.g. ridge waveguide, contact opening and metallization) of the device [127]. This is a complex expensive, time consuming process, involving at least two epitaxial growth stages and two processing stages, and it may suffer from contamination between the different growth and processing stages.

The DFB lasers can be alternatively fabricated using surface gratings [128, 129]. In this case the geometry of a weakly index-guided ridge waveguide laser (processed after the complete epitaxial growth of the epiwafer has been accomplished) includes a periodic corrugation on one or the both sides. This method reduces the fabrication complexity, costs but has the disadvantage that optical feedback (i.e the grating coupling coefficient) is limited due to the limited overlap between the optical field distribution and the grating area. However, with a proper design the laterally corrugated (LC) ridge waveguide gratings can provide sufficient optical feedback [5, 129].

It should be mentioned that the end facets also have an important role in the design and operation of DFB lasers. When the optical feedback of the grating is weak, the magnitudes and phases of the end facet reactivities govern the behaviour of DFB lasers. If the optical feedback is stronger than the magnitudes of the end facet reactions the grating dominates and the end facets have a negligible effect on the operation of a DFB laser.

Regardless of the fabrication method, the DFB grating structure can be described as a one dimensional photonic crystal that prevents the propagation of light with wavelengths within a stopband around the Bragg wavelength. Since modes cannot propagate within the stopband a 'pure' DFB structure (i.e. without any other feedback mechanism apart from the grating) supports two degenerate modes placed at the first antinodes on the sides of the stopband. The most common ways to lift the dual-mode degeneracy of DFB lasers and achieve stable single longitudinal mode emission are the use of un-balanced reflection from the laser facets, the use of periodic gain/loss variation (aligned with the refractive index variation) and the use of phase-shift(s). The un-balanced facet reflections are usually achieved by high-reflection (HR) and anti-reflection (AR) coating of the facets. One problem

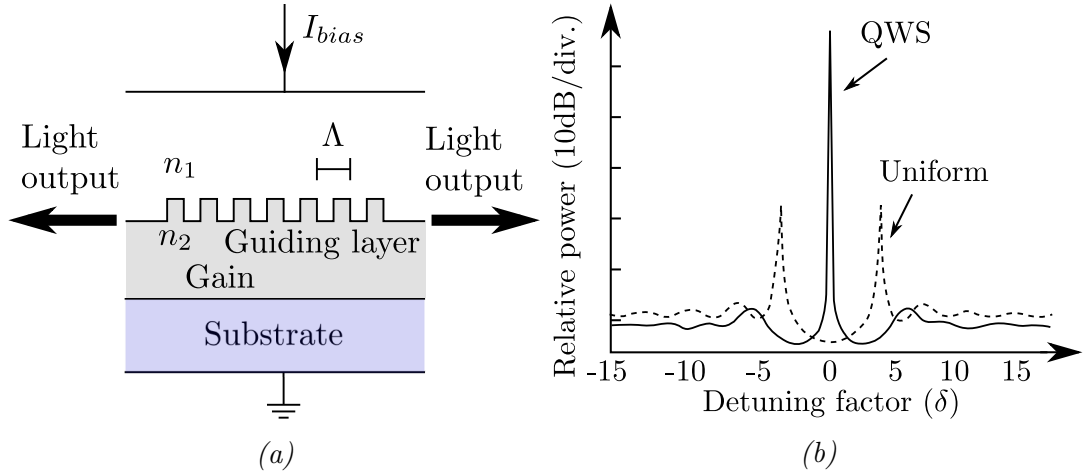


Figure 3.4: (a) shows the grating structure of a DFB laser. (b) shows the optical spectrums of an uniform DFB laser and a QWS-DFB laser.

of this approach stems from the fact that the cleaved laser facets cannot be accurately positioned with respect to the gratings. This makes the mode selection based on un-balanced facet reflections very tricky and un-reproducible. Moreover, the un-controllable phase of the facet reflections with respect to the grating reflections creates fabrication yield problems as most of the laser characteristics (e.g. emission wavelength, output power, linewidth, modulation bandwidth, side-mode-suppression-ratio) depend on it.

The periodic gain variation can be achieved through injection current modulation (when the grating affects the longitudinal current distribution) or through loss variation induced by the grating structure. Although it ensures good single-longitudinal mode stability, a significant and index-grating-phase-matched gain/loss variation is tricky to achieve and might affect the laser characteristics.

A quarter wavelength long defect (phase-shift) placed within the grating introduces a reflectivity dip in the stopband. This dip in the reflectivity enables single longitudinal mode emission for the quarter-wave shifted (QWS) DFB laser [130], which is a desirable property for many applications, particularly in optical communication systems. In QWS-DFB lasers an integer multiple of a quarter of the Bragg wavelength is usually chosen as a phase-shift section for the grating because it guarantees the widest band gap and attenuates the other longitudinal modes near to the Bragg wavelength [130]. Chirped (i.e. with slightly varying period) [131] and apodized (i.e. with varying coupling strength) [132] gratings are used to modify the band structure of the 1D photonic crystal Bragg reflector. Sometimes so called superstructures are applied as well. In superstructures multiple gratings are placed next to each other, such that the individual gratings are separated by a small unperturbed sections [133].

3.6 Chirp and temperature induced effects in semiconductor lasers

Since the carrier density influences both the optical intensity and the emission frequency/wavelength, LDs can be used to generate optical intensity and frequency modulated signals by directly modulating the current flow into the active region. In the digital modulation LDs are typically pre-biased above the threshold current and the digital data is encoded to the optical output by superimposing bias current variations on the pre-bias. As the bias current varies, the carrier density and modal gain switch the output power between different intensity levels.

However, any variation in the carrier density also leads to a refractive index change because the gain and refractive index are related [134], and therefore the emission frequency shifts. Hence, the intensity and frequency modulation are not fully separable and there always is frequency modulation when intensity modulation is present and vice versa. The relationship between the gain and refractive index can be described empirically [135] using the linewidth enhancement factor, $\alpha_{\mathcal{H}}$ ⁷, given by [47]

$$\alpha_{\mathcal{H}} = -\frac{4\pi}{\lambda} \frac{dn_{eff}/dN_c}{dG_m/dN_c}, \quad (3.5)$$

where n_{eff} is the effective refractive index (i.e. the characteristic refractive index of the laser structure), N_c is the electron density in the conduction band, and G_m is the modal gain. Because the differential gain and refractive index are wavelength dependent, it also reflects into the $\alpha_{\mathcal{H}}$ -factor. It has been observed that the $\alpha_{\mathcal{H}}$ -factor usually becomes smaller as the emission wavelength (given by the Bragg resonance) is blue-shifted with respect to the gain peak in DFB lasers (because this increases the differential gain at the denominator of eq. 3.5). On the other, hand the $\alpha_{\mathcal{H}}$ -factor increases when the emission wavelength is red-shifted from the gain peak [115, 136, 137].

There are several mechanisms that generate heat in LDs. Most of these are somehow also related to carrier density, such as non-radiative recombination, resistive heating, intraband scattering, optical absorption, and surface recombinations [119]. Particularly, carriers inside the active region can generate heat (largely through hot carrier relaxation), which is conducted away from the structure and dissipated into the surrounding environment. Temperature affects (usually negatively) many characteristics of LDs, among them the threshold current [138], quantum efficiency [139],

⁷Unfortunately, it is hard to measure the $\alpha_{\mathcal{H}}$ -factor directly and therefore experimental results are always dependent on the measured structure. For example, the temperature tuning effect is also related to thermal expansion of the grating pitch in DFB lasers.

and noise [140]. Consequently, the operation temperature of LDs is often stabilized.

The temperature variations induce changes in the refractive index and in the material gain mainly because temperature modifies the band structure (particularly by reducing the bandgap) in semiconductors [141]. The refractive index and the material gain perturbations shift the emission wavelength. In some cases this is a detrimental effect, but in some a desired property. Temperature also brings its contribution to the $\alpha_{\mathcal{H}}$ -factor. When temperature rises, the derivatives of the gain and refractive index with respect to carrier density decrease, but the slope of the gain usually declines faster than the slope of the refractive index. For this reason increasing temperature decreases the $\alpha_{\mathcal{H}}$ -factor [142].

Generally rising temperature increases the refractive index and the grating pitch in DFB lasers. On the other hand growing carrier density lowers the refractive index due the band filling, bandgap shrinkage, and free carrier absorption [115]. Hence, temperature and carrier density variations introduce opposite shifts for the emission wavelength. Because temperature variations take place in a slower time scale than carrier variations [57], the FM efficiency, discussed in Section 2.3, is strictly dependent on the variation speed of the injected carriers. At lower variation speeds, the temperature induced wavelength tuning dominates, until temperature variations can no longer follow carrier density variations. At higher variations speeds, the carrier induced refractive index change is solely responsible for the wavelength tuning as the temperature tuning effect vanishes. For QWS-DFB laser the competition between these two counteracting phenomena causes a sharp dip in the FM efficiency close to 10 MHz range modulation frequencies [57]. If a QWS-DFB laser is frequency modulated close to the dip, this may lead to a bit-pattern dependent behaviour, and distort the signal [74].

3.7 Requirements for dual-wavelength laser sources in remote heterodyne detection links

There are several properties that are essential for a dual-wavelength laser source in RHD links. In general the semiconductor lasers have a large phase noise that results in a broad spectral width for the MMW signal when two separately generated (incoherent) laser lines are used to generate the MMW. Hence, RHD links usually exploit laser sources that can generate two phase-correlated laser lines. In dual-wavelength lasers both spectral lines are generated within the same laser cavity and therefore they experience the same dominant noise sources. When both of these spectral lines arrive to the photodetector, the common phase and frequency noises are subtracted and the resulting MMW can have a smaller linewidth than the linewidths of the laser lines in optical domain. The frequency drift of the MMW is also significantly

reduced due to the same effect.

Moreover, a good MMW generation efficiency and a high SNR require that the power levels of the spectral lines are relatively close to each other. However, this requirement is not sufficient to ensure a high quality beat signal after the detection because side modes can act as a background noise to the signal and degrade the SNR, inducing supplementary mixing products that cause problems in the signal processing. Hence, the side modes of the laser spectrum must be suppressed. Although the mode balance is good and the side modes are suppressed, the laser lines must also have sufficient power to overcome transmission losses (coupling losses, fiber attenuation, etc.) but several non-linear effects, discussed in Section 2.2.3, set an upper limit to the powers of the spectral lines that are launched into an optical fiber. Also the structures that utilize a monolithically integrated semiconductor optical amplifier can boost the powers of the laser lines if they are not adequate. Moreover, there are various other characteristics that are wanted in dual-wavelength lasers, including narrow spectral widths (which increases the tolerance with respect to chromatic dispersion) and a common polarization for both spectral lines.

The most troublesome requirement for dual-wavelength lasers in RHD links is the stability of the dual-wavelength emission, which is difficult to attain due to the gain competition of the laser modes. A strong gain competition can cause fluctuations in the relative amplitudes and frequencies of the spectral lines and these variations are directly transferred to the MMW in the detection, deteriorating the quality of the resulted electrical signal. By reducing the spatial overlap of the optical fields of the two modes, the competition for gain of the two laser modes may be alleviated. Because multi-section laser structures can reduce the overlap of the optical field distributions of the two laser lines these structures are favourable solutions in the design of dual-wavelength lasers. It is also possible to efficiently tune the frequency difference of the two modes by injecting a longitudinally non-uniformly distributed bias current into a multi-section laser structure when the modal distributions have a reduced overlap because the modes experience the carrier and temperature induced refractive index changes differently.

4. TRAVELLING WAVE MODEL OF DFB LASERS

The modelling of semiconductor lasers is a complicated task due to many complex interactions taking part in the operation of these devices. The detailed description of LDs would require a full quantum mechanical treatment and the solution of a coupled opto-electro-thermal problem (already outlined in Chapter 3). Since the fabrication process of LDs is never perfect, the similarity between the characteristics of the modelled and fabricated device cannot be taken for granted even for detailed laser models. Essentially the full description can be far too complex to work with. Therefore many simplified models have been proposed to give a basic understanding of the operation of LDs and their dynamic behaviour [143–145].

In this work we concentrate on a one dimensional time-domain travelling wave (TDTW) model based on models described in [127, 146–149]. TDTW models provide many advantages over commonly used standing wave approach which is valid only if the photon lifetime is short compared to the characteristic time of the laser dynamics [150]. Meanwhile TDTW models handle laser dynamics in a very small characteristic time scale [150]. The standing wave approach and other modelling methods forced to seek the resonance frequencies of the laser cavity in the complex plane may suffer from convergence problems. This is particularly problematic if the modelled laser is also unstable, because the instability of the laser can cause further convergence problems, and there isn't necessarily a way to detect the source of the failure [119].

TDTW method, instead, does not handle individual longitudinal modes explicitly, but the resonance frequencies can be found out by applying the discrete Fourier transform to the time-dependent envelope functions of the forward and backward travelling waves [146]. TDTW models are particularly applicable for multi-mode lasers because they do not need to solve resonances self-consistently at each time step as frequency-domain methods. Since TDTW models include stochastic spontaneous emission sources, they also take into account realistically the effects of spontaneous emission and quantum noise on the laser characteristics.

TDTW also has several drawbacks. Particularly the spectral dependency of the material gain or refractive index are hard to implement efficiently in time-domain because the longitudinal modes are not explicitly known during

the simulation¹. Usually TDTW algorithms are only conditionally stable. The stability conditions strictly restrict the spatial and temporal step sizes. Any violation of the stability requirements can lead to spurious solutions and numerical instabilities [127]. Although TDTW algorithms can be used to estimate the linewidth of a laser, this is practical only for relatively broad linewidths because the simulation time is proportionally to the square of the frequency resolution. Thus, very long simulation times are required in order to average out the noise of a narrow linewidth laser [119].

4.1 Travelling wave equations

The classical electromagnetic theory gives a relatively comprehensive picture of DFB lasers from the optical point of view. According to that theory, the solution of an initial and boundary value problem is required to give the full optical description of DFB lasers. Unfortunately large scale Cauchy problems are cumbersome to solve. Since the optical response of LDs is much faster than the electronic or thermal time scales, it is typically sufficient to consider Maxwell's equations in their time-harmonic form. Moreover, it is assumed that the refractive index variations are small in the regions where optical intensity is confined, and therefore the exact solution can be conveniently approximated with relatively good accuracy by a series expansion of TE and TM modes. Because the semiconductor layers, where the light is guided, are very thin in the vertical direction but relatively broad in the lateral direction, it is assumed further that TE and TM modes have only one dominant polarization component similar to well-known slab waveguides [127]. Due to these approximations, the problem can be separated into two coupled but much simpler scalar problems that govern the transverse and longitudinal structures separately. Despite the various approximations, the separation of the longitudinal and transverse solutions is a lengthy procedure and it is not considered in this work but a detailed discussion can be found from for example in [127].

The two dimensional transverse problem provides the transverse field distribution $u(x, y)$ and propagation constant β_m pairs with the given angular frequency ω_m of the m -th longitudinal mode. The solutions correspond to the TE and TM modes of a fully passive guiding structure having an infinite translation symmetry in the longitudinal direction without any gain, loss, or reflections (e.g. grating structure). Although this problem has an infinite number of solutions, there is only a finite number of modes that vanish at infinity and have a real valued propagation constant in a lossless structure. These requirements are essential for the modes guided in a

¹Of course it is possible to apply a DFT-algorithm to the envelope functions after each time step but this is computationally expensive, since the inverse Fourier transform must be performed to return to time-domain.

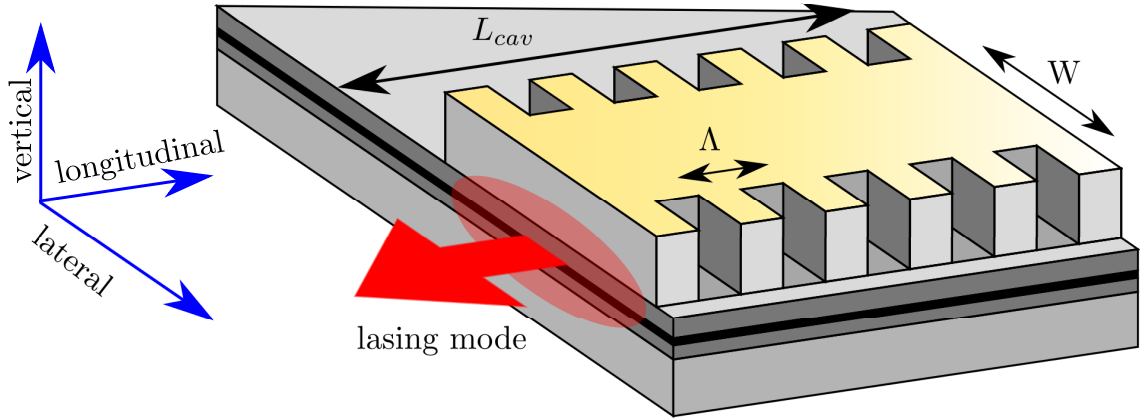


Figure 4.1: Schematics of a DFB laser with laterally-coupled ridge waveguide grating.

passive optical structure. Hence the transverse problem is given by

$$\nabla^2 u(x, y) + k^2 u(x, y) = \beta_m^2 u(x, y), \quad (4.1)$$

with Sommerfeld radiation condition [151]. Moreover it is assumed that the solutions have a continuous first derivative.

The problem is similar to one discussed earlier in Section 1.2.1. Unlike for optical fibres, there are no analytical solutions for the transverse problem that fulfills the boundary conditions in edge-emitting lasers due to the more complicated geometry. Thus, numerical methods are required to approximate the exact TE and TM modes in the transverse cross-section [152, 153].

The design of the transverse structure of DFB lasers is aiming that only the fundamental solutions of TM and TE modes exist (i.e. single transverse mode operation). Because the optical feedback and confinement of TM modes are smaller than TE modes [98], it can be assumed that the fundamental TE mode starts to lase first, and the fundamental TM is suppressed, particularly in compressively strained QW structures.

The second sub-problem examines operation along the longitudinal structure, which is governed by a pair of travelling wave equations (i.e. classical advection equations). The derivation of the travelling wave equations used in this work is based on the assumption that the electric field amplitude can be written as

$$\Psi(\mathbf{r}, t) = u(x, y) \sum_m (F(z, t)e^{\omega_m t + \beta_m z} + R(z, t)e^{\omega_m t - \beta_m z}) \quad (4.2)$$

where $u(x, y)$ is the transverse field distribution of the fundamental TE mode. $F(z, t)$ and $R(z, t)$ are spatially and temporally slowly varying envelope functions.

Taking into account the periodic variation of material or geometry in the longitudinal direction and assuming that the time variations of the refractive index are

slow compared to the optical frequencies, two travelling wave equations are obtained for the counter-propagating envelope functions [127]

$$\frac{1}{v_g} \frac{\partial F}{\partial t} + \frac{\partial F}{\partial z} - (\Gamma g - \alpha - j\delta)F = j\kappa R + i_{spon,f}, \quad (4.3a)$$

$$\frac{1}{v_g} \frac{\partial R}{\partial t} + \frac{\partial R}{\partial z} - (\Gamma g - \alpha - j\delta)R = j\kappa F + i_{spon,r}, \quad (4.3b)$$

where v_g refers to group velocity, g is the material gain per unit distance, Γ is the confinement factor, and α_i is the loss factor. δ is the detuning factor and κ is the coupling coefficient. These parameters are defined more rigorously later in the following sections.

In the TDTW model the counter-propagating envelope functions are solved directly in time-domain and they carry information about the amplitude and phase of the spectral components which is essential in order to characterize the behavior of classical waves in gratings and interfaces. Since photons are not classical particles, the envelope functions and photon density must be somehow tied to each other. As both the photon flux and the square of the classical electric field are proportional to the light intensity, the envelope functions are normalized according to a semi-classical interpretation [154]

$$S = |F|^2 + |R|^2. \quad (4.4)$$

The photon density is related to the optical power of a laser through [154]

$$P = hf v_g S A, \quad (4.5)$$

where A is the area of the guiding region and f is the reference frequency. Here it has been assumed that the photon density is uniformly distributed over the guiding area and vanishes everywhere else.

In general, a partial differential equation without any initial or boundary conditions has an infinite number of solutions or it has no solution. Therefore, auxiliary initial and boundary conditions are imposed. Because it is assumed that there are no photons inside the laser before the simulation starts, the zero solutions are set as initial conditions. It is also required that the solutions of equations (4.3) must meet following boundary conditions

$$F(0, t) = r_2 R(0, t), \quad R(L_{cav}, t) = r_1 F(L_{cav}, t) \quad (4.6)$$

where r_1 and r_2 are the complex reflection coefficient of the end facets and L_{cav} is the cavity length.

4.1.1 Gain and detuning factor in TDTW equations

The TDTW equations described in Section 4.1 are classical advection equations. The general solutions of homogeneous advection equations

$$\frac{1}{v_g} \frac{\partial R}{\partial t} - \frac{\partial R}{\partial z} = 0, \quad (4.7a)$$

$$\frac{1}{v_g} \frac{\partial F}{\partial t} + \frac{\partial F}{\partial z} = 0, \quad (4.7b)$$

are well-known since they simply translate each point in the initial solution to the new position $z \pm v_g \Delta t$. Hence, they describe the movement of waves travelling in the $-z$ and $+z$ directions with velocity v_g . Therefore these equations are also known as one-way wave equations. When the net modal gain, loss factor and phase are added to the right hand side

$$\frac{1}{v_g} \frac{\partial F}{\partial t} + \frac{\partial F}{\partial z} = (\Gamma g - \alpha - j\delta)F, \quad (4.8a)$$

$$\frac{1}{v_g} \frac{\partial R}{\partial t} - \frac{\partial R}{\partial z} = (\Gamma g - \alpha - j\delta)R, \quad (4.8b)$$

it can be shown that substituting trials [127]

$$F = e^{(\Gamma g - \alpha - j\delta)v_g t} \tilde{F}, \quad R = e^{(\Gamma g - \alpha - j\delta)v_g t} \tilde{R} \quad (4.9)$$

into equations (4.8), only the solutions of the advection equations (4.7) in terms of variables \tilde{F} and \tilde{R} are needed. Namely, the solutions of equations (4.8) are simply recovered from these solutions using equations (4.9).

The α_i -factor takes into account general losses such as absorption, radiation and scattering losses within the laser cavity. The detuning factor that appears in Equations (4.8) is defined according to

$$\delta = \beta - \beta_r = \frac{2\pi n_{eff}}{\lambda} - \beta_r, \quad (4.10)$$

where n_{eff} is the characteristic refractive index of the guiding structure also known as effective refractive index. The detuning factor has two main tasks. First of all it is numerically convenient to normalize the propagation constants with respect to a certain reference value. The second task is related to the carrier and temperature induced refractive index changes that can be efficiently implemented using the detuning factor, because it creates an additional phase shift to the envelope functions when n_{eff} changes. The choice of the reference propagation constant is arbitrary. In DFB lasers the detuning factor is often defined as the deviation from the propagation

constant meeting the Bragg condition

$$2\beta_r\Lambda = 2m\pi, \quad (4.11)$$

where Λ is the grating period, and m is an integer known as the grating order. This choice is taken because the grating period is usually constant and in DFB lasers the propagation constants are interesting close to the Bragg condition. If there is no grating present, then a good choice for the reference propagation constant is defined by the wavelength of the peak gain.

4.1.2 Finite difference method and discretization

Assuming that the group velocity is constant throughout the device², the TDTW equations are discretized by dividing the laser into small segments ($s > 0$) with equal lengths in the longitudinal direction. It can be thought that there is node between two adjacent sections where a transfer matrix and a supplementary noise source are located. The transfer matrix and noise source take into account the fundamental processes of DFB lasers (gain, losses, noise, coupling, etc.). At each time step the values of an envelope function are updated in all the nodes using the old solutions from the previous time steps as an input. After the solutions are updated in the node points, then the next time step is taken and the envelope function are once again updated in the node points. Each node point also has a reservoir of carriers that interacts with the photon density through a carrier rate equation.

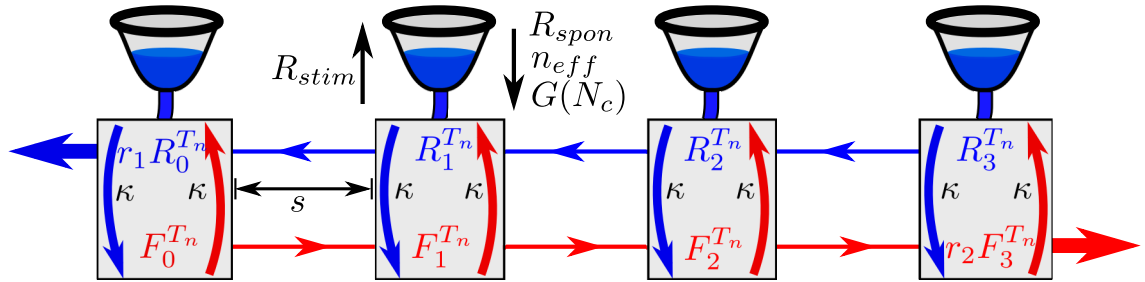


Figure 4.2: Schematics of the numerical implementation of TDTW method. In the figure the forward travelling envelope function ($F_Z^{T_n}$) is propagating to the right, and the reverse envelope function ($R_Z^{T_n}$) travels to the left.

The solutions of the travelling wave equations are searched using the second-order central difference scheme in time and space. Since the method is an explicit time-marching algorithm, the spatial and temporal step sizes ($\Delta t > 0$) are not independent of each other [155]. The numerical stability of the algorithm requires that

²The choice of constant group velocity simplifies the model, but it is not compulsory and the group velocity can vary with respect to the position. However, if the group velocity also depends on time, a more complicated algorithm is required.

so called Courant-Friedrich-Lewy (CFL) condition [156]

$$0 < \frac{v_g \Delta t}{s} = C_{CFL} \leq 1 \quad (4.12)$$

is fulfilled. Otherwise the information is forced to propagate numerically faster than the group velocity which leads to instabilities and the numerical algorithm may yield unreliable, spurious results. The inequation (4.12) is only a necessary condition, but it is not sufficient to ensure the stability. However, it has been shown that the numerical errors at a time step do not grow in time for this particular algorithm [127]. Consequently it is said that the method is numerically stable. This also guarantees that the algorithm generates a solution that remains bounded if Equation (4.12) holds.

In this work central difference approximations are used. The central difference approximation of a spatial derivative is written as

$$\left. \frac{\partial F}{\partial z} \right|_{z=Zs, t=(T-\frac{1}{2})\Delta t} \approx \frac{F_{Z+\frac{1}{2}}^{T-\frac{1}{2}} - F_{Z-\frac{1}{2}}^{T-\frac{1}{2}}}{s}, \quad (4.13)$$

where T and Z are temporal and spatial node points. Time derivatives are approximated using

$$\left. \frac{\partial F}{\partial t} \right|_{z=(Z+\frac{1}{2})s, t=T\Delta t} \approx \frac{F_{Z+\frac{1}{2}}^{T+\frac{1}{2}} - F_{Z+\frac{1}{2}}^{T-\frac{1}{2}}}{\Delta t}. \quad (4.14)$$

Although the values of a continuous function may be approximated using the function value at the previous time step, a more convenient solution in terms of the numerical formulation is to use an averaged value such that

$$F(z, (T - \frac{1}{2})\Delta t) = F_Z^{T-\frac{1}{2}} \approx \frac{1}{2} (F_{Z+\frac{1}{2}}^{T-\frac{1}{2}} + F_{Z-\frac{1}{2}}^{T-\frac{1}{2}}), \quad (4.15)$$

This method is called Lax averaging [157], and it is used when the numerical approximations of the travelling wave equations are constructed later.

Since the finite difference approximations of the time and spatial derivatives arise from cutting off the Taylor series of the corresponding derivatives, there is an error that reflects the fact that only a finite number of terms are used in the approximation. This truncation error decreases as the step size decreases. In the central difference scheme used in this work, the truncation error is proportional to the square of the step size, and therefore it is a second-order method.

There is also another source for numerical errors originating from the finite precision computations. Unlike truncation errors, round-off errors rise as the step size

decreases. Both truncation and round-off errors can spread out the solution such that large gradients are smoothed as time evolves [158]. They also introduce a different numerical dispersion relation for the waves that numerically propagate in the simulation compared to the physical waves [158]. Since the distortions caused by numerical dispersion are smallest when the C_{CFL} -number equals to unity [127, 158], the time and spatial step sizes are chosen according to the condition $\Delta t = s/v_g$.

4.1.3 Gratings and coupled waves

Guided modes of an ordinary dielectric waveguide with infinite translation symmetry are orthogonal and therefore they do not exchange energy with each other. However, a longitudinally periodic perturbation breaks this orthogonality such as contra-propagating waves can interact with each other [159]. The periodic perturbation affects photons in a similar way than the periodicity of a semiconductor crystal affects the motion of electrons. Hence, if the conservation laws of the momentum and energy are fulfilled the optical waves with opposite wave vectors can couple into each other and exchange energy.

Effective index method and coupled-mode theory has been applied to give a relatively good approximation for weakly coupled structures [159–161]. Since these approaches provide a good accuracy with a small computation cost they are used to couple contra-propagating envelope functions into each other in the developed TDTW model. According to the coupled-mode theory a simple complex factor known as coupling coefficient κ is used to describe how much an envelope function is coupled into the another counter-propagating envelope function [162]. When the propagation constant lies in the photonic band gap, the coupling coefficient introduces an imaginary component to the propagation constant, attenuating the corresponding longitudinal mode. For higher order gratings correction terms are used to take into account radiative modes [162]. These terms are neglected in this work.

By adding the coupling term to the right hand side of Equation (4.7), a pair of coupled advection equations are obtained [127]

$$\frac{1}{v_g} \frac{\partial \tilde{F}}{\partial t} + \frac{\partial \tilde{F}}{\partial z} = j\kappa \tilde{R}. \quad (4.16a)$$

$$\frac{1}{v_g} \frac{\partial \tilde{R}}{\partial t} - \frac{\partial \tilde{R}}{\partial z} = j\kappa \tilde{F}. \quad (4.16b)$$

Equations (4.16) should be solved with boundary conditions

$$\tilde{F}(0, t) = r_2 \tilde{R}(0, t), \quad \tilde{R}(L_{cav}, t) = r_1 \tilde{F}(L_{cav}, t), \quad (4.17)$$

and using initial values $\tilde{F}(z, t) = 0$ and $\tilde{R}(z, t) = 0$. Numerically the equations (4.16a) and (4.16b) are approximated by applying the central difference scheme and Lax averaging as discussed in Section 4.1.2. These approximations yield a pair of discrete equations

$$\tilde{F}_{Z+\frac{1}{2}}^{T+\frac{1}{2}} - \tilde{F}_{Z-\frac{1}{2}}^{T-\frac{1}{2}} = j\frac{1}{2}\kappa s \left(\tilde{R}_{Z-\frac{1}{2}}^{T+\frac{1}{2}} + \tilde{R}_{Z+\frac{1}{2}}^{T-\frac{1}{2}} \right), \quad (4.18a)$$

$$\tilde{R}_{Z-\frac{1}{2}}^{T+\frac{1}{2}} - \tilde{R}_{Z+\frac{1}{2}}^{T-\frac{1}{2}} = j\frac{1}{2}\kappa s \left(\tilde{F}_{Z+\frac{1}{2}}^{T+\frac{1}{2}} + \tilde{F}_{Z-\frac{1}{2}}^{T-\frac{1}{2}} \right). \quad (4.18b)$$

Solving Equations (4.18) in terms of unknown variables $\tilde{F}_{Z+\frac{1}{2}}^{T+\frac{1}{2}}$, $\tilde{R}_{Z-\frac{1}{2}}^{T+\frac{1}{2}}$ and substituting (4.9), the transfer matrix (M)

$$\begin{bmatrix} F_{Z+\frac{1}{2}}^{T+\frac{1}{2}} \\ R_{Z-\frac{1}{2}}^{T+\frac{1}{2}} \end{bmatrix} = e^{(g-\alpha-j\delta)s} \underbrace{\frac{1}{1 + \frac{1}{4}\kappa^2 s^2} \begin{bmatrix} 1 - \frac{1}{4}\kappa^2 s^2 & j\kappa s \\ j\kappa s & 1 - \frac{1}{4}\kappa^2 s^2 \end{bmatrix}}_{=M} \begin{bmatrix} F_{Z-\frac{1}{2}}^{T-\frac{1}{2}} \\ R_{Z+\frac{1}{2}}^{T-\frac{1}{2}} \end{bmatrix}, \quad (4.19)$$

for the envelope functions F and R in Equations (4.3) is obtained. Although the indices of the time steps and spatial mesh points in Equations (4.19) are not integers, there is no need to restore envelope functions at half-integer time steps and node points because it is possible to apply an half-integer shift to the variables.

4.2 Carrier rate equation

Travelling wave equations (4.3) and boundary conditions (4.6) are not solely sufficient to describe the behavior of DFB lasers that can exhibit highly non-uniform photon and carrier densities along the length of the device. In order to complete the picture of the energy exchange between carriers and photons in DFB lasers, the optical model must be coupled with the electrical transport process. However, classical macroscopic carrier transport models such as drift-diffusion model are complicated to implement and computationally expensive. Hence it is assumed that each longitudinally sliced segment has a carrier reservoir that interacts with photon density. Within the sections carrier-photon interactions are modelled combining travelling wave equations with a carrier rate equation. The carrier rate equation given by [127]

$$\frac{d(\Gamma V N_c)}{dt} = \frac{I\eta}{q} - 2\Gamma V v_g g(N_c, S, \lambda, T) S - \Gamma V (A_{SRH} N_c + B_{spont} N_c^2 + C_{Aug} N_c^3), \quad (4.20)$$

considers the rate of change of the total carrier number within the active volume occupied by the segment. In Equation (4.20) V is the volume of the guiding region

expressed as $V=As$. η is the injection efficiency which describes the lateral current spreading, leakage over the hetero-barriers, and electron-hole pair recombinations in the WG and barrier layers. A_{SRH} , B_{spont} and C_{Aug} are experimentally determined recombination coefficients. It has been assumed that the optical power is uniformly distributed over V and outside this volume it completely vanishes. Because the active region is much smaller than the region where photons are confined, the term ΓV takes into account that only a fraction of the carrier density overlaps with the photon density.

The first term on the right hand side in Equation (4.20) describes the total number of injected electron-hole pairs. The second term is related to the net rate at which stimulated emission reduces the electrons in the conduction band. The last remaining terms incorporate the reduction of the carrier number due to spontaneous emission and non-radiative recombination. In Equation (4.20) it is assumed that the carrier transit and capture times are negligible. The effects of thermal carrier escape and longitudinal carrier diffusion are also omitted.

4.2.1 Recombination terms

In semiconductors a spontaneous emission event takes place when an electron and a hole recombine. Therefore the spontaneous emission rate depends on the number of occupied electron states N_c in the conduction band and on the number of vacancy states in the valence band P_v . Thus the number of spontaneous emission events is expected to be proportional to the product of the electron and hole number, i.e. $N_c P_v$ [148]. Usually the LD active regions are nominally undoped and therefore the charge neutrality condition $N_c \approx P_v$ holds. Consequently the spontaneous emission rate is approximated by a semi-empirical formula [163]

$$R_{spont} = B_{spont} N_c^2, \quad (4.21)$$

where B_{spont} is the proportionality factor known as bimolecular recombination coefficient. It has been shown that the injection current, bandgap energy, and temperature have a strong impact on B_{spont} [164–167]. B_{spont} is also much smaller for indirect than direct bandgap semiconductors [69].

Excited electrons can also interact with other atoms or particles such that no energy is released in the form of electromagnetic radiation. In such a case the released energy typically excites phonons in the semiconductor crystal. Because non-radiative recombinations do not generate any photons they must be minimized for LDs.

Semiconductor crystals are never perfect, and there are always imperfections and impurities which may affect the characteristics of the structure. Imperfections (i.e.

defects) introduce energy states (i.e. traps) in the forbidden bandgap. These states can also facilitate two step trap-assisted recombination processes which may be associated with absorption of multiple phonons [88]. A carrier is able to use these intermediate states as stepping stones. It can first fall into an intermediate state and in the second step it moves into the valence or conduction band. Because energy and momentum must be preserved during the processes, these transitions emit or absorb photons or phonons.

The Shockley-Read-Hall model characterizes the recombination caused by impurities and other defects in a semiconductor [168]. At high injection levels the recombination rate is approximated as [102]

$$R_{SHR} = \frac{N_c}{\tau_e + \tau_h} = A_{SRH} N_c, \quad (4.22)$$

where τ_e and τ_h are recombination lifetimes of electrons and holes respectively. Because the recombination rate is directly proportional to carrier density, Shockley-Read-Hall recombinations have a limited effect on the total recombination rate at high injection levels.

In Auger recombination processes the released energy of an electron-hole recombination is transferred to a third carrier which can be an electron or hole. Auger recombination processes are non-radiative processes because the energy of the third particle is eventually released to the lattice. In two electron and one hole collisions the rate of Auger recombinations is proportional to the number of available states in the valence band P_v and the square of occupied states in the conduction band N_c . On the other hand processes involving two holes and one electron are proportional to $N_c P_v^2$. Therefore Auger recombination rate depends strongly on the carrier concentrations and it becomes important when both carrier densities are high [102]. Auger recombination rate is expressed as

$$R_{Auger} = C_{Aug} N_c^3, \quad (4.23)$$

where the proportionality factor C_{Aug} is typically determined empirically. C_{Aug} depends also strongly on the band gap, and C_{Aug} decays rapidly when band gap increases. It can be shown that increasing temperature also increases the recombination coefficient [169].

4.3 Gain modelling

Since the material gain $g(N_c, P_v, S, \lambda, T)$ affects many characteristics of LDs, its accurate modelling is required to improve the understanding of the behaviour of LDs. Although thermal effects can be taken into account in the material gain, it

is complicated when the characteristic time scale of a laser is smaller than $\sim \mu s$ [150, 170]. Because the electronic time scale is much smaller $\sim ns$ than the thermal time scale, the temperature distribution must be updated much slower than the carrier density in transient simulations. Since the main interest of this work is focused on direct modulation, the temperature induced variations in the material gain has been neglected in order to avoid complicated coupling between carrier and thermal equations.

In QW structures the material gain varies sub-linearly with respect to the carrier density [111], and therefore the logarithmic fit of material gain is widely applicable for QW lasers [102]. However, the linear fit provides a reasonable good accuracy for LDs with MQW active regions if the total losses are relatively small [111]. Because the lasers, modelled in Chapter 5, must employ a grating having a quite good coupling strength in order to suppress undesired longitudinal resonances, the assumption of the low total losses is expect to be valid. Hence, the carrier density dependence of the material gain is expressed as

$$g(N_c) = g_0(N_c - N_{tr}), \quad (4.24)$$

where N_{tr} is the transparency carrier density and g_0 is an experimentally determined fitting parameter. Gain saturation introduced by carrier heating and spectral hole burning are included by introducing a non-linear gain coefficient ϵ such that [127]

$$g(N_c, S) = \frac{g(N_c)}{1 + \epsilon S}. \quad (4.25)$$

As discussed before the material gain also depends on the wavelength of photons. Unlike in frequency-domain methods, the wavelength dependence is not straightforward to implement in time-domain methods in which the oscillating longitudinal modes are not explicitly known. A convenient solution is to employ temporal filtering during the simulation [127]. Temporal filtering decreases computational cost because it can be implemented efficiently evaluating simple convolutions directly in time-domain and no conversions between time, and frequency domain is needed during the simulation.

If losses are kept relatively low, the threshold gain is usually also quite low and only the electronic states from the first subband of a strained MQW structure are required to achieve lasing action. In this case a good approximation of the gain curve close to the gain peak is obtained when a parabola or Lorentzian function are fitted to the experimental data. These type of filters are simple to implement and therefore digital Lorentzian filters are used to model gain dispersion in this work. For broadband gain modelling modern spatio-temporal digital filters must be used

instead [171].

As digital filters handle discrete-time signals they are an obvious choice for gain filtering. Linear digital filters are divided roughly into two categories; finite impulse response (FIR) filters and infinite impulse response (IIR) filters according to their filter coefficients. The general formula for digital filters is given by [172]

$$y_n = \sum_{k=0}^M c_k x_{n-k} + \sum_{j=0}^{N-1} d_j y_{n-j-1}. \quad (4.26)$$

For FIR filters the d_j coefficient vanish, contrary to IIR filters where d_j coefficients may have non-zero values. IIR filters are usually more compact and they can approximate the prescribed frequency response accurately with a smaller number of coefficients than FIR filters [172]. Hence IIR filters have smaller storage requirements and it is possible to evaluate the convolution faster but it is worth noting that FIR filters are always stable, whereas IIR filters may be unstable which must be taken into account when IIR filters are designed. In this work the material gain is filtered using an IIR filter. The filter coefficients are given in [127]. The gain filter falls into zero at the Nyquist frequencies $\pm 1/2\delta t$ and thus aliasing errors are avoided.

4.4 Spontaneous emission sources

As DFB lasers in reality, the numerical TDTW model is also excited by spontaneous emission. This feature is implemented using complex spontaneous sources which have randomly distributed real and imaginary parts. At each spatial and time step spontaneous emission sources are substituted into Equations (4.3). Spontaneous emission sources are generated using a normally distributed pseudo-random number generator with zero mean such that the sources fulfill the following correlation relations [154]

$$\langle i_{spon,f,r}(z, t), i_{spon,f,r}(z', t') \rangle = \beta_{spon} (B_{spon} N_c^2) \delta(z - z') \delta(t - t') / v_g, \quad (4.27a)$$

$$\langle i_{spon,f,r}(z, t), i_{spon,f,r}(z, t) \rangle = 0, \quad (4.27b)$$

where β_{spon} is the coupling coefficient of spontaneous emission into the lasing modes, δ_f is the Delta function, and $\langle \cdot, \cdot \rangle$ is the usual inner product of complex numbers. Since the spontaneous emission sources meet Equations 4.27 in the node points at each time step, they are spatially and temporally uncorrelated.

4.5 Spectral linewidth

In communication systems it is preferable that optical sources emit over a narrow spectral width. Fundamentally the spectral width is limited by the coupling of spontaneous emission to the stimulated emission which induces fluctuations to the intensity and phase of the laser output [47]. These fluctuations are not independent of each other and their mutual coupling brings its contribution to the laser linewidth [47].

Hence the linewidth depends on the spontaneous emission rate, but it also depends on several internal and external factors such as the fluctuations in the carrier density, the recombination rates, the optical gain, and the operation temperature. Phase fluctuations of a DFB laser are ideally considered to be a stochastic Gaussian random process. Thus the linewidth is found to be Lorentzian with a spectral linewidth [173]

$$\Delta\nu = \frac{R_{sp}}{4\pi I}(1 + \alpha_{\mathcal{H}}^2) = \frac{\tau v_g^2 n_{sp}}{4\pi(N_c - N_{th})V_{act}}(\alpha_i + \alpha_m)^2(1 + \alpha_{\mathcal{H}}^2), \quad (4.28)$$

where R_{sp} is the spontaneous emission rate, $\alpha_{\mathcal{H}}$ is the linewidth enhancement factor, I is the light intensity, n_{sp} is spontaneous emission coupling factor, v_g is the group velocity, η_i is the injection efficiency, α_i is the internal loss factor, α_m is the mirror loss factor, N_c is the carrier density, and N_{th} is the threshold carrier density.

Equation (4.28) indicates that the linewidth should decrease as the time-averaged output power P_{out} rises and this behaviour has been experimentally observed in LDs at low power levels. However, the linewidth usually saturates close to 1-10 MHz in LDs and starts to broaden as the output power increases beyond the linewidth reduction saturation point [174]. Several reasons for the linewidth rebroadening have been studied; mode instability [55], existence of sidemodes [56], spatial hole burning [175], and non-linearity of gain and refractive index [176].

Even though it is not obvious from Equation (4.28), the linewidth depends on the length of the laser cavity, since R_{sp} decreases as the laser cavity becomes longer and the mirror losses decrease. Also the photon density increases at a given output power. For these reasons the linewidth of a Fabry-Perot laser varies according to L_{cav}^{-2} [174]. The dependence of the cavity length is shown to be much stronger $\kappa^{-2}L_{cav}^{-3}$ in QWS-DFB lasers with no end facet reflections due to the highly concentrated intensity distribution [177]. On the other hand the spatial hole burning can degrade the linewidth if the κL -product is too high, and therefore κ is usually kept relatively low.

Because single QW structures have smaller spontaneous emission coupling factor, it was predicted that single QW structures are superior to MQW structures in

terms of linewidth [110]. Nevertheless it has been noticed that MQW structures can exhibit reduced linewidth compared to their single QW counterparts [174, 178]. These observations are explained through the improved differential gain and smaller state filling in the WG and barrier layers [113]. Due to the same reasons strained QW structures have also shown lower values of the linewidth enhancement factor compared to the lattice matched structures [179]. Under modulation the linewidth broadens significantly due to carrier induced refractive index change. In the TDTW model the effective refractive index change is estimated using a first-order approximation

$$n_{eff}(N_c) \approx n_{eff,0} + \Gamma N_c \frac{\partial n_{eff}}{\partial N_c}, \quad (4.29)$$

where $n_{eff,0}$ is a known reference value at negligible carrier injection.

4.6 TDTW modelling of multi-section lasers

The developed TDTW model gives a good picture of complex multi-section lasers with a relatively low computational cost. The model takes into account the longitudinally non-uniform distributions for the carrier and photon densities, for the gain, for the grating coupling coefficient, for the losses, for the effective refractive index, and the longitudinal variations of the transverse sections. Different combinations of active, passive, grating and gratingless sections are also easily modelled. Furthermore, spontaneous noise sources are included into the model, making the algorithm more realistic.

Despite the simplicity of the model it is possible to obtain reasonable estimates for many device characteristics such that the linewidth, threshold current, optical power, and spectrum, which can be compared to experimental results. The simulations performed with the model provide a detailed information about important characteristics within the laser cavity that cannot be measured directly (e.g. longitudinal carrier and photon densities). Many of the longitudinally non-uniform characteristics are essential when the laser structures are designed and optimized to achieve the best possible performance.

The model allows continuous wave as well as transient analysis for a relatively short time-scale, providing important information about the behavior of a laser in time-domain (the rise and fall times, the frequency and damping rate of relaxation oscillations, the overshoot and undershoot of the signal, the jitter). The algorithm is flexible and it is possible to incorporate various sub-problems to the TDTW model in order to improve its correspondence with respect to actual devices.

5. SIMULATION RESULTS AND COMPARISONS

In this chapter a simulation program based on the model described in Chapter 4 is used to estimate some basic continuous wave (CW) and transient operation properties of the well-known QWS-DFB and Fabry-Perot lasers. These results are compared with the analytical and numerical solutions obtained in [180,181] which exploit the power matrix method (PMM).

The chapter also contains sections that introduce CW and large signal modelling results, and analysis of superstructure grating (SSG) DFB lasers. These lasers can be used to generate dual-wavelength emission with electrically tunable frequency separation. CW analysis concentrates on the characteristics of the laser structure without any applied modulation. In the large signal analysis the dynamic behavior of the structure under direct modulation is investigated. The dynamic analysis reveals how the dual-wavelength emission generated with the aid of the SSG-DFB laser structure can carry frequency modulated digital data at a MMW carrier frequency in a RIN limited unamplified RHD link.

In the simulations the receiver is assumed to be perfect and no additional noise is imposed due to the detection. More detailed analysis would require that shot and thermal noises, and PIIN are inserted into the signal. Dispersion and non-linearity of the communication channel are also neglected for simplicity. However, it is possible to include chromatic dispersion in the large signal analysis with a relatively straightforward method by filtering the numerical signal generated by the TDTW model [4]. The characterization of non-linear effects in a RHD link requires more rigorous treatment, and the solution of the pulse propagation equation that can be solved numerically using for example split-step Fourier method [4].

5.1 Conventional laser structures

In the following the large signal dynamics and CW behavior of a QWS-DFB laser are considered briefly by using the same simulation parameters as in [180,181]. These modelling parameters are listed in Appendix B. At first the light-current characteristics of the laser are investigated by running a series of independent simulations with uniformly distributed injection current. After each simulation the bias current is increased, and the final output power of a laser end facet is stored. Because it

has been seen from the output signal that the turn-on transients settle down before 8 ns even for high injection levels, the simulation time of an individual simulation is chosen to be 15 ns in order to guarantee that the CW operation is reached. In [112] it has been found that the threshold current of the laser lies close to 32 mA. According to the TDTW simulations the threshold current is about 29 mA. The bias current is increased to $I_1 = 49$ mA where both PMM and TDTW implementations give about 2.5 mW output power in the CW operation.

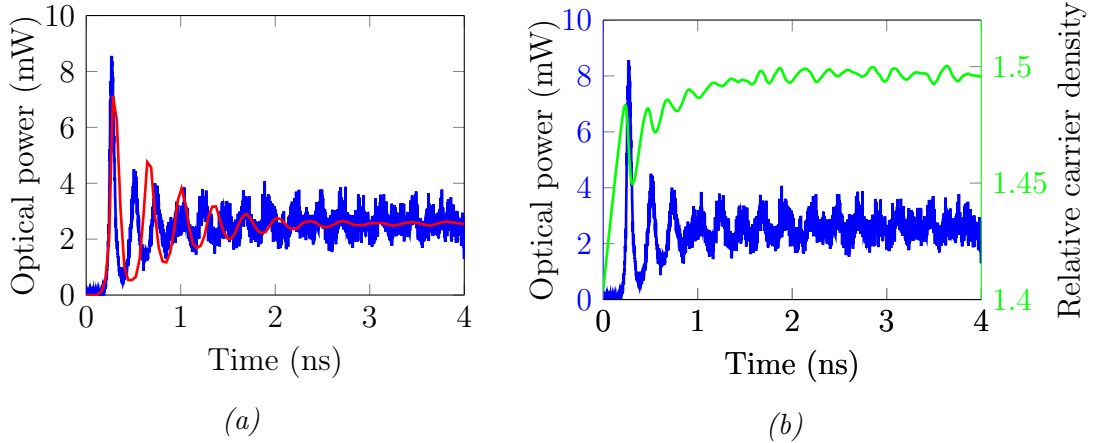


Figure 5.1: (a) depicts the optical power response from one of the facets of the QWS-DFB laser to a step variation of the bias current from just below the threshold current to approx. $1.7 I_{th}$. The red graph is the solution presented in [112], where the problem is solved using PMM. The blue graph is the solution obtained with the implemented TDTW program. (b) illustrates the evolution of the longitudinally averaged relative carrier density (green) and the optical output power (blue) calculated by the TDTW program. The carrier densities are normalized to the transparency carrier density (i.e. $N_c = N_{tr} = 1$).

In the second stage the large signal modulation characteristics of the laser are considered. The laser is biased just below the threshold value and the simulation is run as long as the carrier and photon densities reach the steady-state. Then a step-like current density is injected to the laser such that the bias current is switched rapidly to I_1 . The output power of a laser facet and the longitudinally averaged carrier density are stored during the simulation. Moreover, two spectrums of the signal are calculated by applying a Fourier transform algorithm [182] to the output power. The first spectrum is evaluated from the first 2 ns after the bias current is switched to I_1 and the second spectrum is calculated from a time period between 2 and 4 ns.

Figure 5.1 shows how the carrier density starts to climb up as soon as the current pulse is injected, whereas the photon density waits until the threshold carrier concentration is reached. After that the photon density and optical power rapidly increase and cause carrier density to drop as stimulated emission rate causes more and more

electrons to fall into the valence band. Consequently, the gain also drops, reducing the photon density. Carriers can then accumulate again and initiate an increase in the photon density. This energy exchange is referred to relaxation oscillations (*ROs*), and its consequences were discussed earlier in Section 3.3.2.

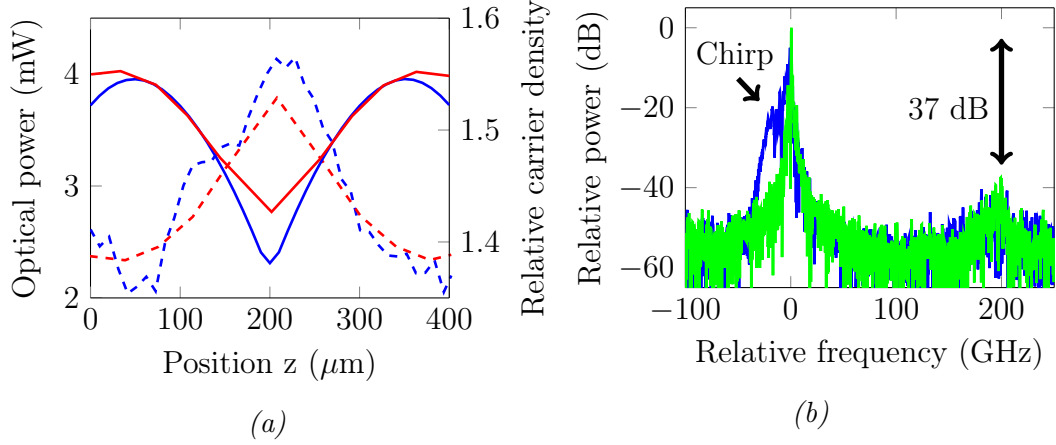


Figure 5.2: (a) indicates the optical power along the longitudinal QWS-DFB laser structure evaluated using the implemented program (dashed blue) and PMM (dashed red) [112]. (a) shows also the corresponding relative carrier densities for the laser structure (solid lines). (b) illustrates the spectra of the simulated QWS-DFB laser during the transients (blue) and under the CW operation (green). This figure shows how the chirp broadens the spectral width of the QWS-DFB laser under direct modulation.

Figure 5.1 points out that there are still significant variations in the output power after the *ROs* have decayed ($t > 2.5$ ns). These fluctuations are induced by the spontaneous emission noise and a poor side-mode suppression ratio (SMSR) [154]. In QWS-DFB lasers the defect in the middle of the longitudinal structure creates a peak in the highly non-uniform longitudinal photon density that drains the population inversion associated with the main mode. However, the main mode does not deplete the population inversion in the nodes of the optical field and other modes can exploit the population inversion of the gain material in the middle of the longitudinal structure because they have a different longitudinal periodicity than the main mode. Hence, this effect, known as longitudinal spatial hole burning (LSHB), may weaken the SMSR and lead to a multimode operation in devices that have a high κL_{cav} -product [154, 180].

In order to verify the correct operation of the gain filtering, the optical spectrum of a typical Fabry-Perot laser structure is simulated in the CW operation. The simulation parameters can be found from Appendix B. The simulated mode spacing is 100.1 GHz with the frequency resolution of 13 MHz. This is in good agreement

with the theoretical mode spacing 101.4 GHz given by equation [183]

$$\Delta f = \frac{v_g}{2L_{cav}}. \quad (5.1)$$

Figure 5.3b also shows clearly that the Lorentzian gain filtering works as intended.

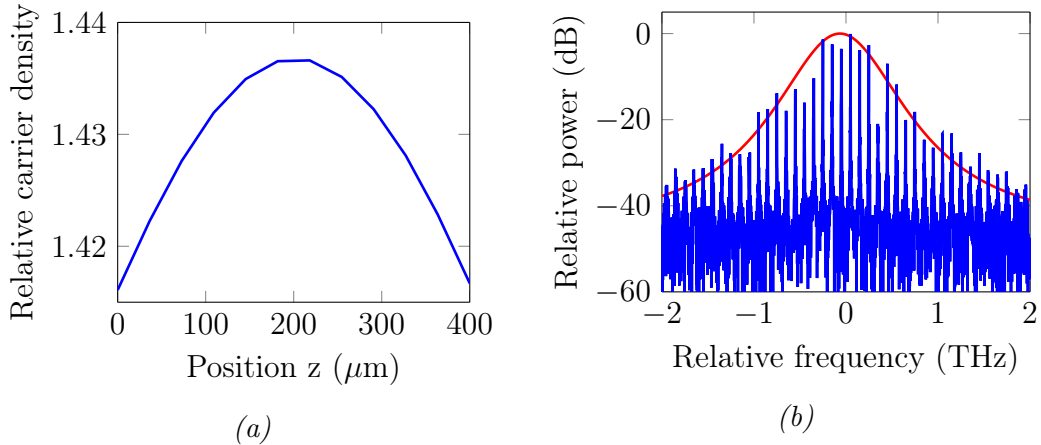


Figure 5.3: (a) is the relative carrier density in the longitudinal direction of the Fabry-Perot LD. (b) shows the calculated optical spectrum of the modelled Fabry-Perot laser with Lorentzian filtering (blue), and a Lorentzian fit (red).

5.2 SSG-DFB laser structures

As discussed in Section 2.1 there are several ways to generate the desired phase-correlated laser lines in RHD links. Dual-wavelength semiconductor lasers have many advantages over the other approaches discussed in Section 2.1. Compact size, low power consumption, high spectral purity, high integrability with optical fibres, low complexity, and low-fabrication cost make dual-wavelength lasers very tempting sources for optical MMW generation. Furthermore, temperature and carrier induced refractive index changes can be exploited to tune the generated MMW frequency. Unfortunately, despite various studies no electrically tunable and stable dual-wavelength QW based semiconductor laser is reported covering the 20–80 GHz frequency separation to the best of author’s knowledge. In this work a monolithic SSG-DFB laser structure with strained MQW active region is analyzed in terms of dual-wavelength emission.

In the analyzed SSG-DFB laser structure two longitudinal modes correspond to the emitted wavelengths. The SSG structure responsible for the selection of these modes consist of multiple internal cavities in which one of the longitudinal mode dominates. This enables the modes to have a substantial spatial overlap in the longitudinal direction while having significantly different longitudinal distributions.

Since both longitudinal modes have almost identical transverse field profile, the longitudinal modes can interact with each other through the gain medium and the grating structure. Hence, the laser structure should provide two highly phase-correlated laser lines that can create a narrow linewidth MMW signal upon detection.

Since the photon densities associated with the main modes are spatially concentrated in different regions of the laser, the power levels of the modes can be balanced by non-uniform current injection into the structure. Also by varying the injection current, it is possible to tune the frequency separation. Several dual-mode SSG-DFB lasers have been fabricated in the ICT FP7 DeLight project using laterally corrugated ridge waveguide gratings, covering the difference frequency band from 20 GHz to 1.3 THz. The lasers have been fabricated employing UV-nanoimprint lithography [129]. In Section 5.3 some measurement and simulation results based on the legacy laser chips are presented.

5.3 CW analysis of SSG-DFB laser structures

This section is devoted to the CW analysis and modelling of the SSG-DFB lasers using the developed TDTW program. In order to provide high quality dual-wavelength emission, a good balance between the power levels of the generated longitudinal modes must be obtained. The currents required to balance the modes are found out by a series of independent simulations.

In each simulation a constant longitudinally non-uniform distributed current density is injected through the contacts into the laser. Once the turn-on transients of the photon and carrier densities have settled down, the simulation is run until a sufficiently long sample is recorded and a discrete Fourier transform is performed for the sample. The simulation series yields a bias map depicting the currents at which the modes are balanced. In addition, several other parameters such as the power levels of the unwanted side modes and the tuning range of the MMW frequency can be also calculated during the simulation series. A simulation series is run for a structure that is targeted to create a frequency difference close to 45 GHz. The used modelling parameters are given in Appendix B.

As shown in Figures 5.4a and 5.4c, the simulated and measured mode spacings have a reasonable good correspondence although several effects are neglected, including temperature induced refractive index change that has an opposite influence on the refractive index than pure carrier density variations. This explains the difference between the shifts of the measured and simulated optical spectra under increasing bias currents because the implemented TDTW model does not take into account thermal effects. Hence, an increasing bias current shifts the spectrum towards higher frequencies in the TDTW model. However, temperature induced refractive index change is much stronger than the carrier induced refractive index change, when

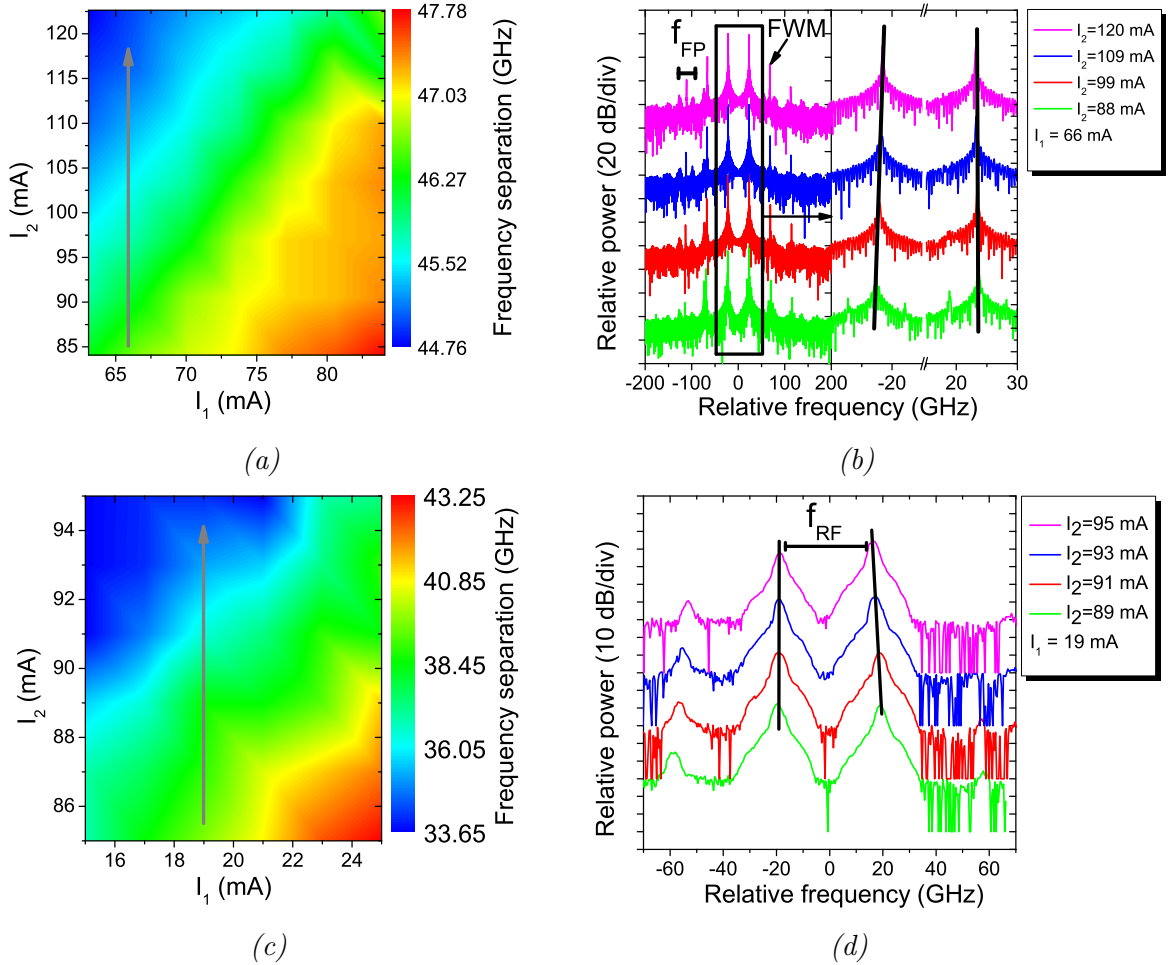


Figure 5.4: (a) shows a map of the simulated frequency difference f_{RF} as a function of two bias currents. The third contact is unbiased. The black arrow indicates the current tuning that has been used to generate the spectra of the laser output in the optical domain shown in (b). (c) and (d) show the corresponding measurement results with slightly different bias currents. f_{FP} denotes the frequency spacing of Fabry-Perot modes.

the bias current changes slowly. Therefore, the measured optical spectrum shifts towards smaller frequencies in Figure 5.4d when the bias current increases.

The Figures 5.4 show that the mode spacing remains almost constant if both currents are increased or decreased simultaneously. If one of the currents is varied and the second one is kept constant, the mode spacing and mode balance change. Moreover, a high tuning efficiency is obtained if one of the currents is increased and the second one is decreased simultaneously. Figures 5.4b and 5.4d also show that almost all the other modes are suppressed with respect to the two dominating ones. Both the simulations and the measurements show two side modes on both sides of the dominating modes. These side modes are displaced from the two main modes by the frequency difference of the main modes. These side modes are present even

when the end facets are perfectly anti-reflection coated and they can be attributed to four-wave mixing (FWM), arising from the non-linear interaction of the main modes. The magnitude of the side modes is related to the overlap of the main modes, the frequency difference of the dominating modes, and the gain compression [184].

To reliably carry information the frequency and amplitude of the MMW signal must be relatively stable. The linewidth of the generated MMW signal is a good indicator of the frequency stability. The linewidths of the measured and simulated signals have been estimated by fitting a Lorentzian lineshape to the spectrums of the MMW signals. The linewidth of the simulated MMW signal and the simulated linewidths of the optical carriers are below 1 MHz. The accurate values are not obtained because this would require impractical simulation times and a very high memory capacity in order to average out the spontaneous emission noise.

The linewidth of the MMW signal is measured by an electronic spectrum analyzer. In the measurement system the laser output is fed into a p-i-n photodiode that generates the MMW beat signal. The photodiode is connected to a broadband electrical amplifier and a bandpass filter that is used to remove the out-of-band noise from the signal before it is fed into the spectrum analyzer. Several successive measurements have been made and the narrowest measured linewidth is 15.6 MHz with the frequency resolution of 24 kHz. Unfortunately, during the measurements it has been noticed that the linewidth experiences considerable fluctuations is broadened up to 159 MHz, when the operation temperature and injection current are kept constant. The linewidth of a SSG-DFB laser is also measured under single-mode operation using self-homodyne measurement technique [7]. The measured results are in the 13–15 MHz range¹. No significant fluctuation in the linewidth has been observed during the measurements.

The amplitude noise level of the MMW signal is traced by capturing the amplitude of the signal using a high-speed oscilloscope with a sampling rate of 80 GS/s. Figure 5.5b reveals that the amplitude noise of the beat signal is relatively low in the measured and simulated MMW signals. Although the output powers of the fabricated lasers are low and therefore the RIN spectrums are not measured, the eye diagram of the output power in Figure 5.5c confirms that under single-mode operation the lasers do not have a particularly large intensity noise level. Furthermore, Figure 5.5a shows that the short-term stability of the measured MMW frequency in the dual-mode operation is poor.

¹In the measurements the bias levels are only slightly perturbed from the currents that balance the modes in dual-mode emission. To avoid poor SMSR, the optical spectrum has been monitored during the measurements.

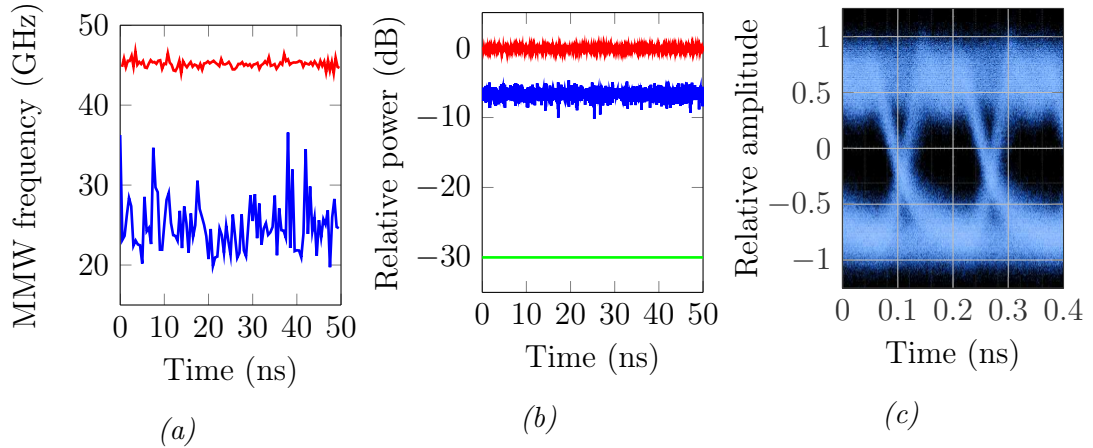


Figure 5.5: (a) shows the instantaneous frequency of the simulated (with red line) and the measured (with blue line) signal. The signals are demodulated using Hilbert transform [185]. (b) presents the amplitude variations of the simulated (with red line) and the measured (with blue line) signals within a 7 GHz frequency span around the central frequency. The green line gives the estimated noise floor that is evaluated from the frequency spectrums. Moreover, the eye diagram in (c) shows the measured output power of the laser under 5 Gbps modulation in single-mode operation.

5.4 Multimode dynamics of LDs

Simulating the non-linear dynamics of LDs is a complex problem and it includes several phenomena such as mode and injection locking [186], and frequency pushing and pulling effects [187]. Moreover, multi-mode LDs are known to have complicated dynamic behavior also due to gain competition under certain operation conditions because of self and cross saturation effects [186, 188]. The dynamic analysis of LDs is particularly important because LDs never actually reach the steady state due to noise caused by the stochastic nature of photogeneration processes, and the steady-state analysis is no longer valid if noise sources are taken into account. Therefore many different approaches have been used to understand the dynamics of LDs [127, 189, 190]. Since each longitudinal mode is driven by spatially and temporally uncorrelated spontaneous emission events, the modes fundamentally experience unavoidable fluctuations in terms of power and frequency although the injected current is held stable.

In RHD links the fluctuations in the power levels or frequencies of the laser lines are directly transferred to the MMW signal affecting its quality. Because cross saturation effects enhance the intensity and frequency noises of multi-mode lasers [191, 192], these effects are detrimental in terms of link performance and should be kept to a minimum.

The cross saturation of the gain is associated with the reduction of the population inversion that corresponds to a certain oscillation mode due to other oscillating

modes. If the instantaneous power of a lasing mode suddenly increases due to a noise source, the population inversion of the electronic states corresponding to the lasing mode is depleted and carriers try to fill this spectral hole by re-distributing themselves via electron-electron and electron-phonon scattering [97]. This reorganization takes place in the intraband relaxation time scale which is in the sub-picoseconds range in QW based materials [97]. The scattering reduces the carrier densities related to other modes leading to the decreasing gain and power of these modes. Hence, an increase in the power of a longitudinal mode causes reduction of the power levels of other modes, and therefore the power spectrum of the laser output can fluctuate significantly compared to the total power.

The fluctuation of the power partition is referred to as mode partition noise and its magnitude depends on many characteristics of the lasers such as the bias levels [188] and the number of longitudinal modes. Large mode partition noise can be found in LDs oscillating just a few longitudinal modes with comparable powers [140]. Also adjacent modes experience much larger power fluctuations than modes that are further apart [193]. In addition the linewidth broadening of the gain material as well as the spatial overlap of the photon populations of different longitudinal modes affect the cross gain saturation and mode partition noise [187]. Very strong mode partition noise occurs when dual-mode emission is generated from two nominally single-mode states that are rapidly switching between each other [140].

Because the gain and refractive index are related through Kramers-Kronig relationship [134], mode partition noise and mode hopping also affect the refractive index of the active region and can cause variation in the mode spacing. Mode partition noise as well as mode hopping take place at the time scale of the cavity round-trip time and therefore these phenomena may be averaged out from the spectrum at high frequencies [140]. However, both of these phenomena are detectable at frequencies below the relaxation oscillation frequency in the spectrum [188, 189]. Because the cavity round-trip time is typically just a couple of ps, the mode partition noise and mode hopping can still affect the MMW signal in time-domain.

Cross saturation effects are partly taken into account in the TDTW model because each spatial node has only a single carrier reservoir that contains all the carriers in the conduction (or holes in the valence band) without any energy dependence. However, the photon densities associated with the lasing modes are not explicitly known during a simulation run in the TDTW model. Cross saturation and spectral burning are suspected to increase the difference between the measured and simulated results.

5.5 Large signal analysis of distributed phase shift structures

In the following the large signal dynamics of SSG-DFB structures is considered. This section gives a theoretical perspective for explaining experimentally observed instabilities discussed in the previous sections. The laser modelling parameters used in this section can be found from Appendix B.

In the beginning several independent simulations have been carried out to find three uniformly distributed currents that keep the suppression ratio between the dominating modes below 3 dB while the suppression ratio between the weakest main mode and the strongest competing side mode is required to exceed 20 dB. This optimization procedure is run for two different structures, where the second one is slightly modified by apodization in order to reduce the effects of LSHB, and increase the uniformity of the longitudinal carrier and photon density distributions.

For both structure variants two different sets of bias currents (\mathcal{I}_0 and \mathcal{I}_1), allowing continuous tuning of the MMW frequency are chosen such that the conditions for the dominating and side modes given above are fulfilled, and the tuning range is maximized by changing two currents out of three and keeping one of the currents constant. Relatively high bias currents are used to achieve a high stimulated emission rate that reduces the carrier lifetime and causes the carrier density rapid decay between successive '0' and '1' states in digital modulation experiments [68]. After the bias currents are determined for both structure variants, the current pulse responses of the structures are simulated by injecting currents \mathcal{I}_0 to the structure until the CW operation is reached and then imposing a 0.4 ns long current pulse with currents \mathcal{I}_1 to the laser.

Figure 5.6 shows that the carrier density has a much longer rise time in SSG-DFB lasers compared to a QWS-DFB laser with the same bias currents and model parameters. The apodized grating structure allows a wider maximum tuning range for the MMW frequency (12 GHz) compared to the unapodized laser structure (7 GHz) with a little bit higher current swing. Large RO s of the SSG-DFB structures can be also alleviated by proper pulse shaping [194,195], reducing the current swing, or increasing the photon density within the laser cavity such that the non-linearity of the gain dampens RO s. However, a smaller current swing reduces the tuning range of the MMW frequency, and a high photon density can increase the magnitude of the unwanted FWM side modes compared to the dominating modes.

In the following a FSK transmission experiment is performed for the apodized SSG-DFB structure by injecting current pulses to the laser, which represent a pseudo random binary sequence. The signal is demodulated using a delay line interferometer described in Section 2.3.1. The optimum delay that maximizes the extinction ratio between '0's and '1's is found to be 56 ps for a 9 GHz frequency tuning that is used

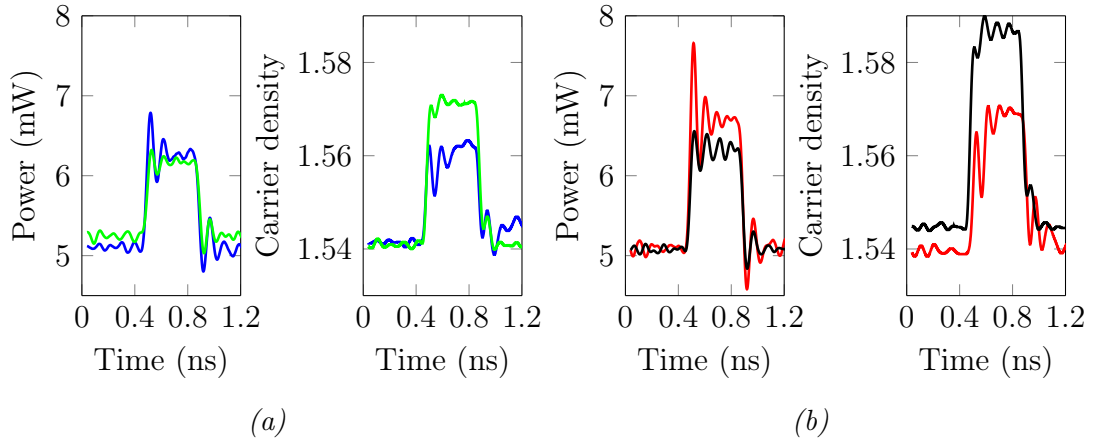


Figure 5.6: (a) presents the optical power (on left panel) and carrier density (on right panel) responses of an SSG-DFB structure (with green line) and the corresponding responses QWS-DFB laser (with blue line) having the same injection currents. (b) shows with red line the power (on left panel) and carrier density (on right panel) responses of an apodized SSG-DFB structure. The black lines are the power and carrier density responses of the reference QWS-DFB laser. The oscillations in the output power and the carrier density at the MMW frequencies are filtered out from the figures.

in the simulation [57]. The demodulated signal is split into two bit long sections that are superimposed to form an eye diagram. In the simulations the bias current is assumed to have 15 ps rise and fall times.

Figure 5.7 shows that the FSK modulated signal has a good vertical eye opening which indicates to a good tolerance with respect to additive noise as expected. On the other hand the intensity modulated signal of the QWS-DFB laser has a smaller timing jitter, and rise and fall times resulting in a better horizontal eye opening. The longer transitions between the logical symbols and the larger jitter are related to the high rise and fall times of the carrier density, and larger fluctuations in the carrier density induced by the beat signal. The longer transitions are also a consequence of the delay which the demodulator requires in order to provide a good extinction ratio between different logical symbols. The delay can be reduced at the expense of the extinction ratio, or by increasing the tuning range. However, during the simulations it has been observed that the improved tuning range increases the relaxation oscillations, leading to larger rise and fall times of the carrier density.

One way to increase the data rate of FSK signals is to increase the number of signalling frequencies. In this way it is possible to increase the number of logical values that correspond to a certain frequency in the signal. This power efficient modulation method is referred to multiple frequency shift keying (MFSK). In MFSK the overlap between the different MMW frequencies that correspond to different logical symbols is higher than in the binary FSK modulation and therefore the symbol rate must

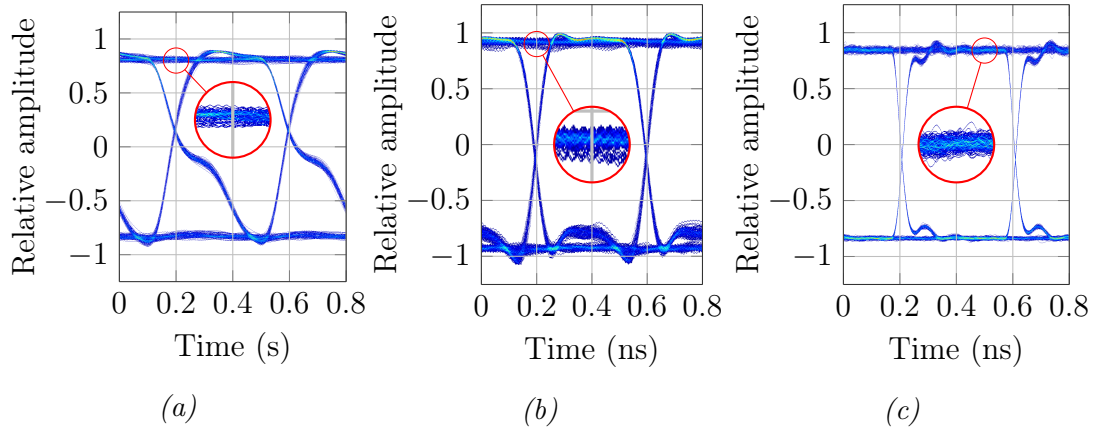


Figure 5.7: (a) is the eye diagram of a demodulated FSK signal that is generated using an apodized SSG-DFB structure with gain compression factor $\epsilon = 1 \times 10^{-17}$. (b) is the eye diagram of the same structure with $\epsilon = 3.5 \times 10^{-17}$. (c) shows the eye diagram of the output power of a QWS-DFB structure with the same laser modelling parameters under single-mode operation when the laser is modulated using the same bias currents with $\epsilon = 3.5 \times 10^{-17}$. The modulation speed is 2.5 Gbps in all of the cases.

be decreased to achieve the same BER value with a given bandwidth. A simulation run is also made for a SSG-DFB structure by increasing the number of signalling frequencies to four by introducing two additional MMW frequencies between the frequencies that were used in the previous simulations. The spectrum of the received signal and the carrier density variations are presented in Figure 5.8.

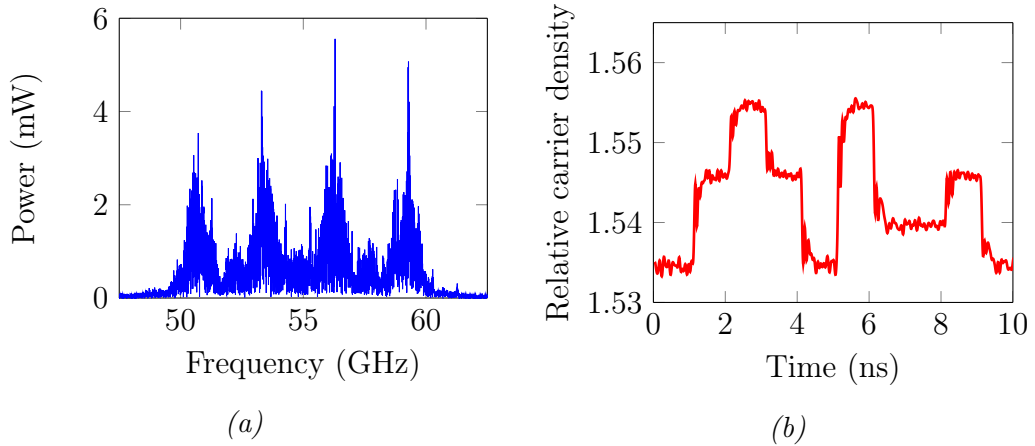


Figure 5.8: (a) depicts the spectrum of the beat signal in the MFSK modulation with four signalling frequencies. The symbol rate is 1 GBd/s. (b) shows a small time sample from the variations of the carrier density within the laser cavity in the MFSK modulation.

5.6 Comparisons

In Section 5.1 the results given by the implemented TDTW program and the solutions of the reference results [112] were presented. It has been observed that the threshold currents slightly differ from each other. In the PMM, that is implemented in [112], the excitation of the numerical model is slightly different from the TDTW implementation and therefore it is expected that this is the main reason for the difference. However, it has been observed that at high injection currents the output powers of the TDTW method and the PMM approach to each other. The transient simulations show that the rise and settling time, and the damping rate of *ROs* are similar, but the *RO* frequencies have a clearly observable difference.

For the SSG laser structure, the measured and the simulated mode spacing have a good correspondence. However, increasing bias current red shifts the longitudinal modes in the measured spectrum contrary to the simulations where the increasing bias current blue shifts the spectrum. This difference is mainly related to the temperature induced refractive index change. A better analysis requires that the thermal problem is coupled to the TDTW model. Despite this difference, the behavior of the MMW frequency is very similar. It is observed in the measurements and simulations that a significant frequency difference tuning occurs when the mode balance changes simultaneously. Only a small change in the frequency difference is observed when the mode balance is kept constant and the tuning currents are increased or decreased simultaneously. Furthermore, a balanced dual-wavelength emission is achieved with different bias currents which can follow from the uncertainties of the model parameters (for example, differences in the injection efficiency, gain or losses with respect to the actual device) or effects that are completely neglected in the model such as temperature induced refractive index change.

Even though the narrowest measured MMW linewidth is 15.6 MHz, it has been observed to experience significant fluctuations. Similar kind of behavior is also noted in time-domain measurements when the MMW signal is directly captured by a fast oscilloscope. The linewidth and time-domain experiments suggest that the MMW signal suffers from stability problems. In the simulation studies the laser structure does not have similar kind of variations in the linewidth or in the MMW frequency. Cross saturation effects and spectral hole burning are considered to be, at least partially, the cause of these fluctuations and both of these phenomena are neglected in the simulations. Moreover, transient analysis shows that it is possible to tune the MMW frequency and use it to transmit FSK or MFSK modulated signals. Simulations also indicate that the MMW frequency can suffer from large *ROs* without paying attention to the damping of these oscillations.

CONCLUSIONS AND FUTURE RESEARCH

The main focus of this work has been on the optical generation of MMWs, exploiting RHD links and the modelling of novel dual-wavelength lasers with a tunable frequency difference. It has been observed that the RHD links have many advantages over conventional approaches in the optical MMW generation and they have a superior performance over IMDD links in applications where MMWs are generated remotely since the periodic fading of the signal is completely avoided. RHD links can also exploit efficiently advanced modulation methods, signal processing tools, and electronic dispersion compensation. In order to generate a high quality MMW signal, RHD links require a laser source that emits two stable and phase-correlated spectral lines. Dual-wavelength lasers could provide low cost laser sources with a small footprint, low power consumption, and tunable MMW frequency for RHD links.

In this work a relatively simple and computationally inexpensive TDTW model is presented to take into account spontaneous emission noise, gain dispersion, and longitudinal variations in the effective refractive index, gain, photon and carrier densities. This model can be applied to multi-section lasers with complex grating structures, and multiple active and passive sections which may be required to obtain various characteristics (including a good mode balance, high tuning range of the frequency difference and a good side mode suppression, and reduced modal overlap) that are essential for tunable dual-wavelength lasers operating in RHD links.

It has been noted that the numerical implementation of the model provides solutions that are in a reasonable agreement with the literature and experimental results. The simulation results have shown that the novel laser structure could provide a good solution for light sources in RHD links with a tunable frequency difference that can be used in various applications.

Several further improvements of the model have been identified during the research. It has been perceived that it is important to incorporate thermal effects, carrier transport in the SCH region, and energetic dependence of carriers using multi-mode carrier rate equations into the TDTW model to further examine the behavior of SSG-DFB lasers. In the analysis thermal effects are important due to non-uniform pumping that affects the longitudinal effective refractive index and modal gain distributions. It is expected that thermal effects have also impact on the frequency separation and the tuning of the spectral lines. Carrier transport in the SCH region in turn influences the rise and fall times of the injected current density, and lateral carrier diffusion may dampen the theoretically predicted large ROs in SSG-DFB lasers [140]. Due to the experimentally observed instabilities in SSG-DFB lasers, it is also essential to include the energy dependence of carriers to

the model in order to investigate spectral hole burning, mode partition noise, and the dual-mode operation of SSG-DFB lasers more accurately. More realistic optical transmission simulations in RHD links also require improved models for optical fibres and receivers, introducing dispersion, non-linear effects, and various phase and intensity noise sources to the signal.

REFERENCES

- [1] Alexander Graham Bell. On the production and reproduction of sound by light. *American Journal of Science*, 118:305–324, 1880.
- [2] KC Kao and George A Hockham. Dielectric-fibre surface waveguides for optical frequencies. *Proceedings of the Institution of Electrical Engineers*, 113(7):1151–1158, 1966.
- [3] Charles A. Brackett. Dense wavelength division multiplexing networks: Principles and applications. *IEEE Journal on Selected Areas in Communications*, 8(6):948–964, 1990.
- [4] P Agrawal Govind. Fiber-optic communication systems. pages 1–20,24–72,114–181, 188–225,345–397,459–510. John Wiley & Sons, 2002.
- [5] Mitsuo Fukuda. Optical semiconductor devices. pages 153–159,381–395. John Wiley & Sons, 1999.
- [6] Brett Wilson, Zabih Ghassemlooy, and Izzat Darwazeh. Analogue optical fibre communications. Number 32. Iet, 1995.
- [7] Rongqing Hui and Maurice O’Sullivan. Fiber optic measurement techniques. pages 25–27,51–85,196–207,484–514. Academic Press, 2009.
- [8] Daniel Colladon. On the reflections of a ray of light inside a parabolic liquid stream. *Comptes Rendus*, 15:800–802, 1842.
- [9] John Tyndall. On some phenomena connected with the motion of liquids. In *Proc R Inst Great Britain*, volume 1, page 446, 1854.
- [10] Ajoy Ghatak and K Thyagarajan. An introduction to fiber optics. pages 38–42. Cambridge university press, 1998.
- [11] Jerry D Gibson. The communications handbook. CRC press, 2002.
- [12] James Clerk Maxwell. A treatise on electricity and magnetism. volume 1. Clarendon press, 1881.
- [13] Tai L Chow. Mathematical methods for physicists: A concise introduction. pages 321–343. Cambridge University Press, 2000.
- [14] Giovanni Ghione. Semiconductor devices for high-speed optoelectronics. pages 51–78,158–254,265–355. Cambridge University Press, 2009.

- [15] Stephen B Alexander. Optical communication receiver design. pages 96–109, 120–167,223–268. SPIE Optical engineering press Bellingham, Washington, USA, 1997.
- [16] Kirk Steven Giboney, Mark JW Rodwell, and John E Bowers. Traveling-wave photodetectors. *IEEE Photonics Technology Letters*, 4(12):1363–1365, 1992.
- [17] LY Lin, MC Wu, T Itoh, TA Vang, RE Muller, DL Sivco, and AY Cho. Velocity-matched distributed photodetectors with high-saturation power and large bandwidth. *IEEE Photonics Technology Letters*, 8(10):1376–1378, 1996.
- [18] Dušan S Golubović, Petar S Matavulj, and Jovan B Radunović. Characterization and optimization of a resonant cavity enhanced pin photodiode response. *International journal of infrared and millimeter waves*, 20(1):109–123, 1999.
- [19] Robert J McIntyre. The distribution of gains in uniformly multiplying avalanche photodiodes: Theory. *IEEE Transactions on Electron Devices*, 19(6):703–713, 1972.
- [20] PW Milonni and JH Eberly. Laser physics ch. 13. pages 569–585. Wiley, 2010.
- [21] John R Barry and Edward A Lee. Performance of coherent optical receivers. *Proceedings of the IEEE*, 78(8):1369–1394, 1990.
- [22] Masataka Nakazawa, Kazurō Kikuchi, Tetsuya Miyazaki, et al. High spectral density optical communication technologies. volume 10, pages 11–51. Springer, 2010.
- [23] U Gliese, S Norskov, and TN Nielsen. Chromatic dispersion in fiber-optic microwave and millimeter-wave links. *IEEE Transactions on Microwave Theory and Techniques*, 44(10):1716–1724, 1996.
- [24] Ulrik Gliese, T Norskov Nielsen, Soren Norskov, and KE Stubkjaer. Multifunctional fiber-optic microwave links based on remote heterodyne detection. *IEEE Transactions on Microwave Theory and Techniques*, 46(5):458–468, 1998.
- [25] H Schmuck. Comparison of optical millimetre-wave system concepts with regard to chromatic dispersion. *Electronics Letters*, 31(21):1848–1849, 1995.
- [26] E Iannone, F Matera, A Galtarossa, G Gianello, and M Schiano. Effect of polarization dispersion on the performance of im-dd communication systems. *IEEE Photonics Technology Letters*, 5(10):1247–1249, 1993.

- [27] MS Islam, SP Majumder, and M Rezwan Khan. Performance limitations of an optical intensity modulated-direct detection transmission system due to polarization mode dispersion in a single mode fiber. In *Military Communications Conference, 2006. MILCOM 2006. IEEE*, pages 1–4. IEEE, 2006.
- [28] Owen E DeLange. Wide-band optical communication systems: Part iifrequency-division multiplexing. *Proceedings of the IEEE*, 58(10):1683–1690, 1970.
- [29] T Okoshi and K Kikuchi. Frequency stabilisation of semiconductor lasers for heterodyne-type optical communication systems. *Electronics Letters*, 16(5):179–181, 1980.
- [30] Francois Favre, Luc Jeunhomme, Irene Joindot, Michel Monerie, and J Simon. Progress towards heterodyne-type single-mode fiber communication systems. *IEEE Journal of Quantum Electronics*, 17(6):897–906, 1981.
- [31] Jürgen Franz and Virander K Jain. Optical communications: Components and systems: Analysis–design–optimization–application. pages 45–78,519–547. CRC press, 2000.
- [32] Philippe B Gallion and Guy Debarge. Quantum phase noise and field correlation in single frequency semiconductor laser systems. *IEEE Journal of Quantum Electronics*, 20(4):343–349, 1984.
- [33] Matthias Seimetz. High-order modulation for optical fiber transmission. volume 143, pages 79–85,143–154. Springer, 2009.
- [34] Seb J Savory. Digital filters for coherent optical receivers. *Optics Express*, 16(2):804–817, 2008.
- [35] Ezra Ip and Joseph M Kahn. Digital equalization of chromatic dispersion and polarization mode dispersion. *Journal of Lightwave Technology*, 25(8):2033–2043, 2007.
- [36] Abdallah Shami, Martin Maier, and Chadi Assi. Broadband access networks. pages 57–60. Springer, 2009.
- [37] P Gallion, FJ Mendieta, and R Leconte. Single-frequency laser phase-noise limitation in single-mode optical-fiber coherent-detection systems with correlated fields. *JOSA*, 72(9):1167–1170, 1982.
- [38] Masahiko Tani, Ping Gu, Masaharu Hyodo, Kiyomi Sakai, and Takehiko Hidaka. Generation of coherent terahertz radiation by photomixing of dual-mode lasers. *Optical and Quantum Electronics*, 32(4-5):503–520, 2000.

- [39] Andreas Klehr, Jorg Fricke, Arne Knauer, Gotz Erbert, Martin Walther, Rafal Wilk, Martin Mikulics, and Martin Koch. High-power monolithic two-mode dfb laser diodes for the generation of thz radiation. *IEEE Journal of Selected Topics in Quantum Electronics*, 14(2):289–294, 2008.
- [40] Graham H Smith, Dalma Novak, and Zaheer Ahmed. Overcoming chromatic-dispersion effects in fiber-wireless systems incorporating external modulators. *IEEE Transactions on Microwave Theory and Techniques*, 45(8):1410–1415, 1997.
- [41] JJ O’reilly, PM Lane, Rolf Heidemann, and Rolf Hofstetter. Optical generation of very narrow linewidth millimetre wave signals. *Electronics Letters*, 28(25):2309–2311, 1992.
- [42] L Goldberg, HF Taylor, JF Weller, and DM Bloom. Microwave signal generation with injection-locked laser diodes. *Electronics Letters*, 19(13):491–493, 1983.
- [43] RP Braun, G Grosskopf, D Rohde, and F Schmidt. Low-phase-noise millimeter-wave generation at 64 ghz and data transmission using optical sideband injection locking. *IEEE Photonics Technology Letters*, 10(5):728–730, 1998.
- [44] LA Johansson and AJ Seeds. Millimeter-wave modulated optical signal generation with high spectral purity and wide-locking bandwidth using a fiber-integrated optical injection phase-lock loop. *IEEE Photonics Technology Letters*, 12(6):690–692, 2000.
- [45] Michael C Gross, Patrick T Callahan, and Michael L Dennis. A fiber laser photonic frequency synthesizer: Concept, performance, and applications. *Johns Hopkins APL Technical Digest*, 30(4):287–298, 2012.
- [46] Ping Gu, Masahiko Tani, Masaharu Hyodo, Kiyomi Sakai, and Takehiro Hidaka. Generation of cw-terahertz radiation using a two-longitudinal-mode laser diode. *Japanese journal of applied physics*, 37(8B):L976, 1998.
- [47] Charles H Henry. Theory of the linewidth of semiconductor lasers. *IEEE Journal of Quantum Electronics*, 18(2):259–264, 1982.
- [48] Milorad Cvijetic. Optical transmission systems engineering. pages 65–85. Artech House, 2004.
- [49] Abhay Joshi, Xinde Wang, Dan Mohr, Don Becker, and Christoph Wree. Balanced photoreceivers for analog and digital fiber optic communications.

- In *Defense and Security*, pages 39–50. International Society for Optics and Photonics, 2005.
- [50] H Schmuck. Carrier-to-noise limitations in optical mm-wave links due to phase-induced-intensity-noise. *Electronics Letters*, 33(14):1236–1237, 1997.
- [51] DA Atlas. Fibre induced distortion and phase noise to intensity noise conversion in external modulated catv systems. *NCTA Technical papers*, page 289, 1996.
- [52] George R Gray, Andrew T Ryan, Govind P Agrawal, and Edward C Gage. Control of optical-feedback-induced laser intensity noise in optical data recording. *Optical Engineering*, 32(4):739–745, 1993.
- [53] Amnon Yariv. Signal-to-noise considerations in fiber links with periodic or distributed optical amplification. *Optics letters*, 15(19):1064–1066, 1990.
- [54] Guohua Qi, Jianping Yao, Joe Seregelyi, Stéphane Paquet, Claude Bélisle, Xiupu Zhang, Ke Wu, and Raman Kashyap. Phase-noise analysis of optically generated millimeter-wave signals with external optical modulation techniques. *Journal of lightwave technology*, 24(12):4861–4875, 2006.
- [55] H Olesen, B Tromborg, HE Lassen, and X Pan. Mode instability and linewidth rebroadening in dfb lasers. *Electronics Letters*, 28(5):444–446, 1992.
- [56] X Pan, B Tromborg, and H Olesen. Linewidth rebroadening in dfb lasers due to weak side modes. *IEEE Photonics Technology Letters*, 3(2):112–114, 1991.
- [57] Richard A Linke and Alan H Gnauck. High-capacity coherent lightwave systems. *Journal of Lightwave Technology*, 6(11):1750–1769, 1988.
- [58] Richard G Smith. Optical power handling capacity of low loss optical fibers as determined by stimulated raman and brillouin scattering. *Applied Optics*, 11(11):2489–2494, 1972.
- [59] Govind P Agrawal. Nonlinear fiber optics. pages 31–58,298–355,389–396. Springer, 2000.
- [60] Yasuhiro Aoki, Kazuhito Tajima, and Ikuo Mito. Input power limits of single-mode optical fibers due to stimulated brillouin scattering in optical communication systems. *Journal of Lightwave Technology*, 6(5):710–719, 1988.
- [61] David Goff. Fiber optic reference guide. pages 36–38. CRC Press, 2002.

- [62] Kyo Inoue. Polarization effect on four-wave mixing efficiency in a single-mode fiber. *IEEE Journal of Quantum Electronics*, 28(4):883–894, 1992.
- [63] Andrew R Chraplyvy et al. Limitations on lightwave communications imposed by optical-fiber nonlinearities. *Journal of Lightwave Technology*, 8(10):1548–1557, 1990.
- [64] AF Elrefaie, DA Atlas, LG Kazovsky, and RE Wagner. Intensity noise in ask coherent lightwave receivers. *Electronics Letters*, 24(3):158–159, 1988.
- [65] Chen Qian. Impact study of multimode fibre taper in modal noise under restricted offset launch conditions. 2007.
- [66] Harrison E Rowe and HE Rowe. Signals and noise in communication systems. van Nostrand New York, 1965.
- [67] Rolf Hofstetter, Harald Schmuck, and Rolf Heidemann. Dispersion effects in optical millimeter-wave systems using self-heterodyne method for transport and generation. *IEEE Transactions on Microwave Theory and Techniques*, 43(9):2263–2269, 1995.
- [68] Michael Bass, Eric W Van Stryland, David R Williams, and William L Wolfe. Handbook of optics. volume 2. McGraw-Hill, 2001.
- [69] John M Senior and M Yousif Jamro. Optical fiber communications: principles and practice. pages 86–163,298–325,444–501, 824–955. Pearson Education, 2009.
- [70] Masaharu Hyodo and Masayoshi Watanabe. Optical generation of millimeter-wave signals up to 330 ghz by means of cascadingly phase locking three semiconductor lasers. *IEEE Photonics Technology Letters*, 15(3):458–460, 2003.
- [71] Ming-Tuo Zhou, Yan Zhang, Shao-Qiu Xiao, and Masayuki Fujise. Signal power degradation due to polarization mismatch in dual-wavelength millimeter-wave fiber-radio systems. In *ITS Telecommunications Proceedings, 2006 6th International Conference on*, pages 478–481. IEEE, 2006.
- [72] A Galtarossa, CG Someda, F Matera, and M Schiano. Polarization mode dispersion in long single-mode-fiber links: a review. *Fiber & Integrated Optics*, 13(2):215–229, 1994.
- [73] L Jeromin and VWS Chan. M-ary fsk performance for coherent optical communication systems using semiconductor lasers. *IEEE Transactions on Communications*, 34(4):375–381, 1986.

- [74] SP Majumder, R Gangopadhyay, and G Prati. Effect of line coding on heterodyne fsk optical systems with nonuniform laser fm response. *IEE Proceedings-Optoelectronics*, 141(3):200–208, 1994.
- [75] AW Davis, MJ Pettitt, JP King, and S Wright. Phase diversity techniques for coherent optical receivers. *Journal of Lightwave Technology*, 5(4):561–572, 1987.
- [76] K Emura, M Shikada, S Fujita, I Mito, H Honmou, and K Minemura. Novel optical fsk heterodyne single filter detection system using a directly modulated dfb-laser diode. *Electronics Letters*, 20(24):1022–1023, 1984.
- [77] Katsumi Emura, Shuntaro Yamazaki, Masayuki Yamaguchi, Minoru Shikada, and Kouichi Minemura. An optical fsk heterodyne dual filter detection system for taking advantage of dfb ld applications. *Journal of Lightwave Technology*, 8(2):243–250, 1990.
- [78] Earl McCune. Practical digital wireless signals. pages 125–160. Cambridge University Press, 2010.
- [79] Keang-Po Ho. Phase-modulated optical communication systems. volume 42, pages 1–20,53–108. Springer, 2005.
- [80] Terumi Chikama, Shigeki Watanabe, Takao Naito, Hiroshi Onaka, Tetsuya Kiyonaga, Yoshihito Onoda, Hideyuki Miyata, Masuo Suyama, Minoru Seino, and H Kuwahara. Modulation and demodulation techniques in optical heterodyne psk transmission systems. *Journal of Lightwave Technology*, 8(3):309–322, 1990.
- [81] Ian Garrett and Gunnar Jacobsen. Theory for optical heterodyne narrow-deviation fsk receivers with delay demodulation. *Journal of Lightwave Technology*, 6(9):1415–1423, 1988.
- [82] Christian Weber, C Bunge, and Klaus Petermann. Fiber nonlinearities in systems using electronic predistortion of dispersion at 10 and 40 gbit/s. *Journal of Lightwave Technology*, 27(16):3654–3661, 2009.
- [83] Robert H Walden. Analog-to-digital converter survey and analysis. *IEEE Journal on Selected Areas in Communications*, 17(4):539–550, 1999.
- [84] Junhao Chu and Arden Sher. Physics and properties of narrow gap semiconductors. pages 151–170. Springer, 2007.
- [85] Leland C Allen. Interpolation scheme for energy bands in solids. *Physical Review*, 98(4):993, 1955.

- [86] Frank Herman. The electronic energy band structure of silicon and germanium. *Proceedings of the IRE*, 43(12):1703–1732, 1955.
- [87] James C Phillips. Energy-band interpolation scheme based on a pseudopotential. *Physical Review*, 112(3):685, 1958.
- [88] Robert Allan Smith. *Semiconductors*. Cambridge Univ. Press, 1978.
- [89] C Kittel. Introduction to solid state physics 7th edition. pages 176–232. John Wiley & Sons, 1996.
- [90] Neil W Ashcroft and ND Mermin. Solid state. *Physics (New York: Holt, Rinehart and Winston)*, pages 131–151,561–584,Appendix M, 1976.
- [91] David Ferry. Semiconductor transport. pages 285–296. CRC Press, 2000.
- [92] Boris I Shklovskii and Alex L Efros. Electronic properties of doped semiconductors. *Moscow Izdatel Nauka*, 1, 1979.
- [93] William Shockley. The theory of p-n junctions in semiconductors and p-n junction transistors. *Bell System Technical Journal*, 28(3):435–489, 1949.
- [94] Leo Esaki and R Tsu. Superlattice and negative differential conductivity in semiconductors. *IBM Journal of Research and Development*, 14(1):61–65, 1970.
- [95] R Dingle, W Wiegmann, and Ch H Henry. Quantum states of confined carriers in very thin $\text{Al}_x\text{Ga}_{1-x}\text{As}$ - Ga_{1-x}As heterostructures. *Physical Review Letters*, 33(14):827, 1974.
- [96] R Dingle, AC Gossard, and W Wiegmann. Direct observation of superlattice formation in a semiconductor heterostructure. *Physical Review Letters*, 34(21):1327, 1975.
- [97] Peter S Zory. Quantum well lasers. pages 18–93. Academic Press, 1993.
- [98] Toshiaki Suhara. Semiconductor laser fundamentals. pages 77–103,255. CRC Press, 2004.
- [99] Shun Lien Chuang. Physics of photonic devices. volume 80, pages 350–407. John Wiley & Sons, 2012.
- [100] Frank Stern. Band-tail model for optical absorption and for the mobility edge in amorphous silicon. *Physical Review B*, 3(8):2636, 1971.

- [101] Minoru Yamada and Yasuharu Suematsu. Analysis of gain suppression in undoped injection lasers. *Journal of applied Physics*, 52(4):2653–2664, 1981.
- [102] Larry A Coldren, Scott W Corzine, and Milan L Mashanovitch. Diode lasers and photonic integrated circuits. volume 218, pages 145–160,218–219,223–226. John Wiley & Sons, 2012.
- [103] David Sands. Diode lasers. pages 156–163. CRC Press, 2010.
- [104] J Nagle, S Hersee, M Krakowski, T Weil, and C Weisbuch. Threshold current of single quantum well lasers: The role of the confining layers. *Applied physics letters*, 49(20):1325–1327, 1986.
- [105] Radhakrishnan Nagarajan, Masayuki Ishikawa, Toru Fukushima, Randall S Geels, and John E Bowers. High speed quantum-well lasers and carrier transport effects. *IEEE Journal of Quantum Electronics*, 28(10):1990–2008, 1992.
- [106] S Morin, B Deveaud, F Clerot, K Fujiwara, and K Mitsunaga. Capture of photoexcited carriers in a single quantum well with different confinement structures. *IEEE Journal of Quantum Electronics*, 27(6):1669–1675, 1991.
- [107] N Tessler, R Nagar, D Abraham, G Eisenstein, U Koren, and G Raybon. Coupling between barrier and quantum well energy states in a multiple quantum well optical amplifier. *Applied physics letters*, 60(6):665–667, 1992.
- [108] H Yamazaki, M Yamaguchi, M Kitamura, and I Mito. Analysis on fm efficiency of ingaas/ingaasp sch-mqw ld’s taking injection carrier transport into account. *IEEE Photonics Technology Letters*, 5(4):396–398, 1993.
- [109] Takahiro Numai. Fundamentals of semiconductor lasers. pages 117–136. Springer, 2004.
- [110] Yasuhiko Arakawa and Amnon Yariv. Theory of gain, modulation response, and spectral linewidth in algaas quantum well lasers. *IEEE Journal of Quantum Electronics*, 21(10):1666–1674, 1985.
- [111] Yasuhiko Arakawa and Amnon Yariv. Quantum well lasers—gain, spectra, dynamics. *IEEE Journal of quantum electronics*, 22(9):1887–1899, 1986.
- [112] B Zhao, TR Chen, and A Yariv. The extra differential gain enhancement in multiple-quantum-well lasers. *IEEE Photonics Technology Letters*, 4(2):124–126, 1992.

- [113] B Zhao, TR Chen, and A Yariv. A comparison of amplitude-phase coupling and linewidth enhancement in semiconductor quantum-well and bulk lasers. *IEEE Journal of Quantum Electronics*, 29(4):1027–1030, 1993.
- [114] T Ishikawa, R Nagarajan, and JE Bowers. Analysis of the effects of doping and barrier design on the small-signal modulation characteristics of long-wavelength multiple quantum well lasers. *Optical and quantum electronics*, 26(7):S805–S816, 1994.
- [115] Brian R Bennett, Richard A Soref, and Jesus A del Alamo. Carrier-induced change in refractive index of in_p, ga_{as} and inga_{asp}. *IEEE Journal of Quantum Electronics*, 26(1):113–122, 1990.
- [116] David K Ferry and Stephen Marshall Goodnick. Transport in nanostructures. Number 6, pages 27–34. Cambridge university press, 1997.
- [117] Alfred R Adams. Strained-layer quantum-well lasers. *IEEE Journal of Selected Topics in Quantum Electronics*, 17(5):1364–1373, 2011.
- [118] D Lancefield, W Batty, CG Crookes, EP O’Reilly, AR Adams, KP Home-wood, G Sundaram, RJ Nicholas, M Emeny, and CR Whitehouse. Pressure dependence of light-hole transport in strained inga_{as}/ga_{as}. *Surface Science*, 229(1):122–125, 1990.
- [119] Joachim Piprek. Semiconductor optoelectronic devices: introduction to physics and simulation. pages 141–158. Academic Press, 2003.
- [120] Hiromitsu Asai and Kunishige Oe. Energy band-gap shift with elastic strain in gax_{1-x}epitaxial layers on (001) ga_{as} substrates. *Journal of Applied Physics*, 54(4):2052–2056, 1983.
- [121] Peter JA Thijs, Luuk F Tiemeijer, PI Kuindersma, JJM Binsma, and Teus Van Dongen. High-performance 1.5 μm wavelength inga_{as}-inga_{asp} strained quantum well lasers and amplifiers. *IEEE Journal of Quantum Electronics*, 27(6):1426–1439, 1991.
- [122] Peter JA Thijs, Teus van Dongen, Luuk F Tiemeijer, and JJM Binsma. High-performance $\lambda = 1.3 \mu\text{m}$ inga_{asp}-in_p strained-layer quantum well lasers. *Journal of Lightwave Technology*, 12(1):28–37, 1994.
- [123] AR Adams. Band-structure engineering for low-threshold high-efficiency semiconductor lasers. *Electronics Letters*, 22(5):249–250, 1986.

- [124] Tsukuru Ohtoshi and Naoki Chinone. Linewidth enhancement factor in strained quantum well lasers. *IEEE Photonics Technology Letters*, 1(6):117–119, 1989.
- [125] SW Corzine and LA Coldren. Theoretical gain in compressive and tensile strained ingaas/ingaasp quantum wells. *Applied physics letters*, 59(5):588–590, 1991.
- [126] Frank Träger. Springer handbook of lasers and optics. pages 767–771. Springer, 2007.
- [127] John E Carroll, James Whiteaway, and Dick Plumb. Distributed feedback semiconductor lasers. volume 10, pages 22–24,58–66,97–162, 211–246,329–351. IET, 1998.
- [128] LM Miller, JT Verdeyen, JJ Coleman, RP Bryan, JJ Alwan, KJ Beernink, JS Hughes, and TM Cockerill. A distributed feedback ridge waveguide quantum well heterostructure laser. *IEEE Photonics Technology Letters*, 3(1):6–8, 1991.
- [129] M Dumitrescu, J Telkkälä, J Karinen, J Viheriälä, A Laakso, S Afzal, J-P Reithmaier, M Kamp, P Melanen, P Uusimaa, et al. Development of high-speed directly modulated dfb and dbr lasers with surface gratings. In *SPIE OPTO*, pages 79530D–79530D. International Society for Optics and Photonics, 2011.
- [130] John D Joannopoulos, Steven G Johnson, Joshua N Winn, and Robert D Meade. Photonic crystals: molding the flow of light. pages 6–65. Princeton university press, 2011.
- [131] Hartmut Hillmer, Anton Grabmaier, HL Zhu, Stefan Hansmann, and Herbert Burkhard. Continuously chirped dfb gratings by specially bent waveguides for tunable lasers. *Journal of Lightwave Technology*, 13(9):1905–1912, 1995.
- [132] Yuechun Shi, Simin Li, Renjia Guo, Rui Liu, Yating Zhou, and Xiangfei Chen. A novel concavely apodized dfb semiconductor laser using common holographic exposure. *Optics express*, 21(13):16022–16028, 2013.
- [133] V Jayaraman, DA Cohen, and LA Coldren. Demonstration of broadband tunability in a semiconductor laser using sampled gratings. *Applied physics letters*, 60(19):2321–2323, 1992.
- [134] Kronig R. de L. On the theory of the dispersion of x-rays. 12:547–557, 1926.
- [135] Basil W Hakki and Thomas L Paoli. Gain spectra in gaas double- heterostructure injection lasers. *Journal of Applied Physics*, 46(3):1299–1306, 1975.

- [136] S Ogita, M Yano, H Ishikawa, and H Imai. Linewidth reduction in dfb laser by detuning effect. *Electronics Letters*, 23(8):393–394, 1987.
- [137] Takayuki Yamanaka, Yuzo Yoshikuni, Kiyoyuki Yokoyama, Wayne Lui, and Shunji Seki. Theoretical study on enhanced differential gain and extremely reduced linewidth enhancement factor in quantum-well lasers. *IEEE Journal of Quantum Electronics*, 29(6):1609–1616, 1993.
- [138] Y Arakawa and Hiroyuki Sakaki. Multidimensional quantum well laser and temperature dependence of its threshold current. *Applied Physics Letters*, 40(11):939–941, 1982.
- [139] LD Zhu, BZ Zheng, and GAB Feak. Temperature dependence of optical gain, quantum efficiency, and threshold current in gaas/gaalas graded-index separate-confinement heterostructure single-quantum-well lasers. *IEEE Journal of Quantum Electronics*, 25(9):2007–2012, 1989.
- [140] Klaus Petermann. Laser diode modulation and noise. volume 3, pages 91–93,163–176. Springer, 1991.
- [141] Philip B Allen and Volker Heine. Theory of the temperature dependence of electronic band structures. *Journal of Physics C: Solid State Physics*, 9(12):2305, 1976.
- [142] Tien-Chang Lu, Bo-Siao Cheng, and Mei-Chun Liu. Temperature dependent gain characteristics in gan-based vertical-cavity surface-emitting lasers. *Optics express*, 17(22):20149–20154, 2009.
- [143] N Bewtra, GL Tan, R Neumann, F Chatenoud, and JM Xu. Modelling of electro-opto-thermal interactions in quantum well lasers. In *Lasers and Electro-Optics Society Annual Meeting, 1993. LEOS'93 Conference Proceedings. IEEE*, pages 631–632. IEEE, 1993.
- [144] Bernd Witzigmann, Andreas Witzig, and Wolfgang Fichtner. A multidimensional laser simulator for edge-emitters including quantum carrier capture. *IEEE Transactions on Electron Devices*, 47(10):1926–1934, 2000.
- [145] Lutz Schneider, Andreas Witzig, Michael J Pfeiffer, Matthias Streiff, and Wolfgang Fichtner. Coupled electro-thermo-optical simulation of a multisection dbr laser. In *Integrated Optoelectronics Devices*, pages 100–110. International Society for Optics and Photonics, 2003.

- [146] CF Tsang, DD Marcenac, JE Carroll, and LM Zhang. Comparison between 'power matrix model' and 'time domain model' in modelling large signal responses of dfb lasers. *IEE Proceedings-Optoelectronics*, 141(2):89–96, 1994.
- [147] Linh VT Nguyen, Arthur James Lowery, Phillip CR Gurney, and Dalma Novak. A time-domain model for high-speed quantum-well lasers including carrier transport effects. *IEEE Journal of Selected Topics in Quantum Electronics*, 1(2):494–504, 1995.
- [148] John E Carroll. *Rate equations in semiconductor electronics*. Cambridge University Press, 1990.
- [149] AJ Lowery. Comparison between two recent large-signal dynamic dfb laser models. *IEE Proceedings J (Optoelectronics)*, 139(6):402–406, 1992.
- [150] Wei Li, Wei-Ping Huang, and Xun Li. Digital filter approach for simulation of a complex integrated laser diode based on the traveling-wave model. *IEEE Journal of Quantum Electronics*, 40(5):473–480, 2004.
- [151] Thomas G Moore, Jeffery G Blaschak, Allen Taflove, and Gregory A Kriegsmann. Theory and application of radiation boundary operators. *IEEE Transactions on Antennas and Propagation*, 36(12):1797–1812, 1988.
- [152] Matthew NO Sadiku. *Numerical techniques in electromagnetics*. CRC press, 2000.
- [153] Jianming Jin. *The finite element method in electromagnetics*. John Wiley & Sons, 2014.
- [154] LM Zhang, SF Yu, MC Nowell, DD Marcenac, JE Carroll, and RGS Plumb. Dynamic analysis of radiation and side-mode suppression in a second-order dfb laser using time-domain large-signal traveling wave model. *IEEE Journal of Quantum Electronics*, 30(6):1389–1395, 1994.
- [155] John C Strikwerda. Finite difference schemes and partial differential equations. pages 95–102. Siam, 2004.
- [156] Dale R Durran. Numerical methods for fluid dynamics: With applications to geophysics. volume 32. Springer, 2010.
- [157] L Lapidus and GF Pinder. Numerical solution of partial differential equations in science and engineering. 1982.
- [158] Wolfgang Rodi. Large-eddy simulation in hydraulics. pages 50–52. Crc Press, 2013.

- [159] H Haus and Weiping Huang. Coupled-mode theory. *Proceedings of the IEEE*, 79(10):1505–1518, 1991.
- [160] Amnon Yariv. Coupled-mode theory for guided-wave optics. *IEEE Journal of Quantum Electronics*, 9(9):919–933, 1973.
- [161] Kim A Winick. Effective-index method and coupled-mode theory for almost-periodic waveguide gratings: A comparison. *Applied optics*, 31(6):757–764, 1992.
- [162] William Streifer, Donald R Scifres, and Robert Burnham. Coupled wave analysis of dfb and dbr lasers. *IEEE Journal of Quantum Electronics*, 13(4):134–141, 1977.
- [163] H Ghafouri-Shiraz. Distributed feedback laser diodes and optical tunable filters. pages 31–78. John Wiley & Sons, 2004.
- [164] CB Su, R Olshansky, J Manning, and W Powazinik. Carrier dependence of the radiative coefficient in iii-v semiconductor light sources. *Applied Physics Letters*, 44(8):732–734, 1984.
- [165] A Mozer, Stefan Hausser, and M Pilkuhn. Quantitative evaluation of gain and losses in quaternary lasers. *IEEE Journal of Quantum Electronics*, 21(6):719–725, 1985.
- [166] Robert Olshansky, CB Su, J Manning, and William Powazinik. Measurement of radiative and nonradiative recombination rates in ingaasp and algaas light sources. *IEEE Journal of Quantum Electronics*, 20(8):838–854, 1984.
- [167] W Van Roosbroeck and W Shockley. Photon-radiative recombination of electrons and holes in germanium. *Physical Review*, 94(6):1558, 1954.
- [168] We Shockley and WT Read Jr. Statistics of the recombinations of holes and electrons. *Physical Review*, 87(5):835, 1952.
- [169] Sheng S Li. Semiconductor physical electronics. pages 135–149. Springer, 2007.
- [170] Xun Li and Wei-Ping Huang. Simulation of dfb semiconductor lasers incorporating thermal effects. *IEEE Journal of Quantum Electronics*, 31(10):1848–1855, 1995.
- [171] Miroslav Kolesik and Jerome V Moloney. A spatial digital filter method for broad-band simulation of semiconductor lasers. *IEEE Journal of Quantum Electronics*, 37(7):936–944, 2001.

- [172] William H Press. Numerical recipes 3rd edition: The art of scientific computing. pages 667–673. Cambridge university press, 2007.
- [173] Charles H Henry. Phase noise in semiconductor lasers. *Journal of Lightwave Technology*, 4(3):298–311, 1986.
- [174] M Aoki, K Uomi, T Tsuchiya, Shinji Sasaki, M Okai, and N Chinone. Quantum size effect on longitudinal spatial hole burning in mqw $\lambda/4$ -shifted dfb lasers. *IEEE Journal of Quantum Electronics*, 27(6):1782–1789, 1991.
- [175] H Wenzel, HJ Wünsche, and U Bandelow. Linewidth rebroadening in semiconductor lasers due to lateral spatial holeburning. *Electronics Letters*, 27(25):2301–2302, 1991.
- [176] F Girardin, Guang-Hua Duan, and P Gallion. Linewidth rebroadening due to nonlinear gain and index induced by carrier heating in strained quantum-well lasers. *IEEE Photonics Technology Letters*, 8(3):334–336, 1996.
- [177] Keisuke Kojima, Kazuo Kyuma, and Takashi Nakayama. Analysis of the spectral linewidth of distributed feedback laser diodes. *Journal of Lightwave Technology*, 3(5):1048–1055, 1985.
- [178] Fumiyo Kano, Takayuki Yamanaka, Norio Yamamoto, Hiroyasu Mawatari, Yuichi Tohmori, and Yuzo Yoshikuni. Linewidth enhancement factor in in-gaasp/lnp modulation-doped strained multiple-quantum-well lasers. *IEEE Journal of Quantum Electronics*, 30(2):533–537, 1994.
- [179] Colin E Webb and Julian DC Jones. Handbook of laser technology and applications: Laser design and laser systems. volume 2, pages 270–275, 590–591, 713–714. CRC Press, 2004.
- [180] James EA Whiteaway, GHB Thompson, Andrew J Collar, and CHRISTOPHER J Armistead. The design assessment of $\lambda/4$ phase-shifted dfb laser structures. *Quantum Electronics, IEEE Journal of*, 25(6):1261–1279, 1989.
- [181] LM Zhang, John Carroll, et al. Large-signal dynamic model of the dfb laser. *Quantum Electronics, IEEE Journal of*, 28(3):604–611, 1992.
- [182] Fftw. <http://www.fft.org>. Accessed: 2014-01-31.
- [183] Osamu Wada. Optoelectronic integration: Physics, technology and applications: Physics, technology, and applications. volume 269, pages 148–152. Springer Science & Business Media, 1994.

- [184] M Radziunas and H-J Wünsche. Multisection lasers: longitudinal modes and their dynamics. In *Optoelectronic Devices*, pages 121–150. Springer, 2005.
- [185] Michael Feldman. Hilbert transform, envelope, instantaneous phase, and frequency. *Encyclopedia of Structural Health Monitoring*, 2009.
- [186] Govind P Agrawal and Niloy K Dutta. Semiconductor lasers. pages 44–56,289–297. Van Nostrand Reinhold, New York, 1993.
- [187] Anthony E Siegman. Lasers university science books. *Mill Valley, CA*, 37:462–466, 1986.
- [188] Moustafa Ahmed and Minoru Yamada. Influence of instantaneous mode competition on the dynamics of semiconductor lasers. *IEEE Journal of Quantum Electronics*, 38(6):682–693, 2002.
- [189] Govind P Agrawal. Gain nonlinearities in semiconductor lasers: Theory and application to distributed feedback lasers. *IEEE Journal of Quantum Electronics*, 23(6):860–868, 1987.
- [190] Andrew T Ryan, Govind P Agrawal, George R Gray, and Edward C Gage. Optical-feedback-induced chaos and its control in multimode semiconductor lasers. *IEEE Journal of Quantum Electronics*, 30(3):668–679, 1994.
- [191] Govind P Agrawal. Mode-partition noise and intensity correlation in a two-mode semiconductor laser. *Physical Review A*, 37(7):2488, 1988.
- [192] George R Gray and Govind P Agrawal. Effect of cross saturation on frequency fluctuations in a nearly single-mode semiconductor laser. *IEEE Photonics Technology Letters*, 3(3):204–206, 1991.
- [193] W Throssell. Partition noise statistics for multimode lasers. *Journal of Lightwave Technology*, 4(7):948–950, 1986.
- [194] F Koyama and K Iga. Frequency chirping of external modulation and its reduction. *Electronics Letters*, 21(23):1065–1066, 1985.
- [195] L Bickers and LD Westbrook. Reduction of transient laser chirp in 1.5 μm dfb lasers by shaping the modulation pulse. *IEE Proceedings J (Optoelectronics)*, 133(2):155–162, 1986.

A. APPENDIX

Description	Symbol	Value (Fig. 2.2 a)	Value (Fig. 2.2 b)	Unit
Second-order dispersion coef.	D	0	17	ps/nm·km
Operation wavelength	λ	1310	1550	nm
MMW frequency	f_{RF}	60	60	Ghz
Relative intensity noise	RIN	-149	-149	dB/Hz
Amplifier gain (EDFA)	G	0	22	dB
Gain figure (EDFA)	G_n	0	3	dB
Transmitted optical power	P_{in}	10	10	mW
Optical bandwidth	B_{op}	1	1	nm
Linewidth	$\Delta\nu$	12	12	Mhz
Resistance	R	50	50	Ω
Operation temperature	T	300	300	K
Attenuation constant	α	0.35	0.2	dB/km
Responsivity	\mathcal{R}	0.45	0.5	W/A

Table A.1: The parameter values used for different intensity noise sources in the calculations of Figure 2.2 are listed in this table.

B. APPENDIX

Description	Symbol	Value (Fig. 2.2 a)	Value (Fig. 2.2 b)	Unit
Second-order dispersion coef.	D	0	17	ps/nm·km
Operation wavelength	λ	1310	1550	nm
MMW frequency	f_{RF}	60	60	Ghz
Relative intensity noise	RIN	-149	-149	dB/Hz
Amplifier gain (EDFA)	G	0	22	dB
Gain figure (EDFA)	G_n	0	3	dB
Transmitted optical power	P_{in}	10	10	mW
Optical bandwidth	B_{op}	1	1	nm
Linewidth	$\Delta\nu$	12	12	Mhz
Resistance	R	50	50	Ω
Operation temperature	T	300	300	K
Attenuation constant	α	0.35	0.2	dB/km
Responsivity	\mathcal{R}	0.45	0.5	W/A

Table B.1: The parameter values used for different intensity noise sources in the calculations of Figure 2.2 are listed in this table.

C. APPENDIX

Description	Symbol	Value	Unit
Responsivity	\mathcal{R}	0.45	A/W
Shockley-Read-Hall recomb. coefficient	A_{SRH}	0	s^{-1}
Bimolecular recom. coefficient	B_{spont}	1×10^{-10}	cm^3s^{-1}
Auger recom. coefficient	C_{Aug}	3×10^{-29}	cm^6s^{-1}
Gain coefficient	g_0	3×10^{16}	cm^2
Transparency carrier density	N_{tr}	1.5×10^{18}	cm^{-3}
Linewidth enhancement factor	$\alpha_{\mathcal{H}}$	4.86	
Internal loss factor	α_i	40	cm^{-1}
Grating coupling coefficient	κ	50	cm^{-1}
Effective phase refractive index	$n_{eff,0}$	3.27	
Effective group refractive index	v_g	3.7	
Length of the laser cavity	L_{cav}	400	μm
Thickness of the guiding region	d	0.47	μm
Width of the guiding region	W	3.5	μm
Confinement factor	Γ	0.35	
Refraction coefficients	r_1, r_2	0	
Spontaneous emission coupling coefficient	β_{spont}	1×10^{-4}	
Gain compression factor	ϵ	1×10^{-17}	
Number of subsections	M_s	41	
Injection efficiency	η	0	

Table C.1: This table includes the laser modelling parameters that have been used in the CW and dynamic TDTW simulations of Section 5.1. The coupling coefficient is 0 cm^{-1} , and the end facet reflection coefficients are 0.53 for the Fabry-Perot laser.

Description	Symbol	Value	Unit
Responsivity	\mathcal{R}	0.45	A/W
Shockley-Read-Hall recomb. coefficient	A_{SRH}	0	s^{-1}
Bimolecular recom. coefficient	B_{spon}	1×10^{-10}	cm^3s^{-1}
Auger recom. coefficient	C_{Aug}	5×10^{-29}	cm^6s^{-1}
Gain coefficient	g_0	5.2×10^{16}	cm^2
Transparency carrier density	N_{tr}	1.5×10^{18}	cm^{-3}
Linewidth enhancement factor	$\alpha_{\mathcal{H}}$	3.0	
Internal loss factor	α_i	40	cm^{-1}
Grating coupling coefficient	κ	14	cm^{-1}
Effective phase refractive index	$n_{eff,0}$	3.25	
Effective group refractive index	v_g	3.68	
Length of the laser cavity	L_{cav}	1800	μm
Thickness of the guiding region	d	0.25	μm
Width of the guiding region	W	2.2	μm
Confinement factor	Γ	0.055	
Refraction coefficients	r_1, r_2	0	
Spontaneous emission coupling coefficient	β_{spon}	3×10^{-4}	
Gain compression factor	ϵ	1.0×10^{-17}	
Number of subsections	M_s	32	
Injection efficiency	η	0.7	

Table C.2: The modelling parameters of a SSG-DFB laser that have been used in Sections 5.3 and 5.5. The table also gives the simulation parameters for the reference QWS-DFB laser with an exception that the coupling coefficient of this structure is $11 cm^{-1}$. In Section 5.3 the reflection coefficients of the end facets are $r_1 = r_2 = 0.53$. Moreover, the length of the cavity in Section 5.5 is $1400 \mu m$.